이학박사 학위논문

Variational models for multiplicative noise removal

(곱셈잡음 제거를 위한 변분법 모델)

2017년 8월

서울대학교 대학원

수리과학부

나한울

Variational models for multiplicative noise removal

(곱셈잡음 제거를 위한 변분법 모델)

지도교수 강 명 주

이 논문을 이학박사 학위논문으로 제출함

2017년 4월

서울대학교 대학원

수리과학부

나한울

나한울의 이학박사 학위논문을 인준함

2017년 6월

위 원 장	______________________	(인)
부위원장	______________________	(인)
위 원	______________________	(인)
위 원	______________________	(인)
위 원	______________________	(인)

Variational models for multiplicative noise removal

A dissertation
submitted in partial fulfillment
of the requirements for the degree of
Doctor of Philosophy
to the faculty of the Graduate School of
Seoul National University

by

Hanwool Na

Dissertation Director : Professor Myungjoo Kang

Department of Mathematical Sciences
Seoul National University

August 2017

Abstract

This dissertation discusses a variational partial differential equation (PDE) models for restoration of images corrupted by multiplicative Gamma noise. The two proposed models are suitable for heavy multiplicative noise which is often seen in applications. First, we propose a total variation (TV) based model with local constraints. The local constraint involves multiple local windows which is related a spatially adaptive regularization parameter (SARP). In addition, convergence analysis such as the existence and uniqueness of a solution is also provided. Second model is an extension of the first one using nonconvex version of the total generalized variation (TGV). The nonconvex TGV regularization enables to efficiently denoise smooth regions, without staircasing artifacts that appear on total variation regularization based models, and to conserve edges and details.

Key words: image denoising, multiplicative Gamma noise, spatially adaptive regularization parameter, proximal linearized alternating direction algorithm, nonconvex total generalized variation, iteratively reweighted ℓ_1 algorithm
Student Number: 2011-20269

Contents

Chapter 1

Introduction

Image denoising is a challenging task and is widely studied in the field of image processing. Image denoising aims at eliminating noise from a corrupted image, while also preserving essential features such as edges and textures. It typically covers additive noise removal and multiplicative noise removal. Many work have focused on the removal of additive Gaussian noise. However, the Gaussian noise model is not suitable to describe noises in real images such as synthetic aperture radar (SAR), ultrasound images and laser images. In fact, these images are distorted by multiplicative noise, and the multiplicative noise depends on intensity values of the original image. So, the removal of multiplicative noise is more challenging than that of additive Gaussian noise. We focus on multiplicative noise removal.

Let $\Omega \subset \mathbb{R}^2$ be an open and bounded domain with a compact Lipschitz boundary and $u : \Omega \to \mathbb{R}$ be a clean image. The degradation model for observed data f corrupted by multiplicative noise is given by

$$f = u \cdot \eta, \tag{1.0.1}$$

where η represents noise that follows a certain distribution such as Gamma distribution or Rayleigh distribution. In this dissertation, we concentrate on the Gamma-distributed noise present in SAR images, i.e., η is assumed to be Gamma noise with the following density function [43],

$$P(\eta) = \frac{M^M \eta^{M-1}}{\Gamma(M)} e^{-M \cdot \eta}, \quad \text{for } \eta \geqslant 0, \tag{1.0.2}$$

where $M > 0$ is an integer related to the noise level, and Γ is the Gamma function. Thus, the mean of η is 1, and its standard deviation is $1/\sqrt{M}$.

Generally, there are two ways to recover noisy image to a clean image. One is filter based model [42, 26, 72, 38, 39] and the other is the variational model [62, 5, 46, 65, 28, 41, 60]. For filter based model, one of the earliest adaptive filter model [42] used minimum mean square error estimator to obtain the noise filtering algorithm. Later, Kuan, et al. proposed Kuan filter based on maximum a posteriori [39]. Wavelet filter method [12, 11] were studied quickly, but it did not produce a visually satisfactory result by repeatability of the same pattern near edge. In recent years, there are many filters [24, 20] with good results for Gaussian additive noise have been extended to multiplicative noise [33, 59]. However, because of similarity measurement, there is a limitation that can not restore thin or small detail properly.

In a variational framework, several total variation (TV) regularization based models have been proposed for removing multiplicative noise. TV regularization [62] is one of the most well-known regularization approaches for image denoising, owing to its capability in preserving edges and discontinuities. The first variational approach with TV regularization dedicated to multiplicative noise removal was proposed by Rudin et al. [61]. However, their model could only address noise that followed Gaussian distribution. Based on a maximum a posteriori (MAP) estimation, Aubert and Aujol (AA) [5] introduced a new TV based model to remove multiplicative Gamma noise. However, the data-fidelity term in their model is not convex; therefore, resulting computed solutions may not be global optimal solutions. Moreover, their model is strongly dependent on the initialization. To cope with these drawbacks, Shi and Osher (SO) [65] utilized a log transformation and converted the AA model into a convex model. Their model is independent of the initialization, and has demonstrated better denoising results than the AA model. On the other hand, Dong and Zeng (DZ) [23] suggested another convex model, by inserting a quadratic penalty term into the AA model. However, this model is designed to be more suitable for low noise levels, owing to the penalty term. Therefore, Lu et al. [48] modified the DZ model and proposed a new convex model (exp) that can handle high levels of noise. In this dissertation, we extend the exp model [48] to a TV model with local constraints, where the local constraints are derived from local statistical characteristics of some random variables with respect to Gamma noise. All these aforementioned models involve the TV regularization, so they tend to produce some artifacts with stair form in smooth transition regions, which is often called staircasing artifacts. To alleviate these artifacts, several hybrid TV regularization models have been suggested in [13, 15, 50, 9], which combines first and second-order TV functionals. In particular, Feng et al. [25] extended the model in [65], by adopting the total generalized variation (TGV) regularization [9] instead of TV. Moreover, Shama et al. [64] proposed a TGV based model associated with the convex fidelity term in [23].

Nonconvex regularization [40, 58] has drawn interests since nonconvex regularizers have more advantages than convex ones, in terms of keeping edges and discontinuous features. In [37], the authors replaced the TV regularization term by the ℓ_q norm of gradient of image with $0.5 < q < 0.8$ and demonstrated that the nonconvex one finds a better denoised image than TV. Additionally, numerical results in [52] showed that nonconvex regularizations are superior to convex ones. Recently, Oh et al. [55] proposed a nonconvex hybrid TV regularizer, which is a convex combination of TV and second order TV. The authors also showed that the nonconvex hybrid TV produces better denoising results than its convex one as well as TV. The TGV was also extended in [54] to its nonconvex version, and it was validated that the nonconvex TGV has preferable performance compared to the TGV. Hence, we also utilize a nonconvex version of the TGV, to take advantages of both nonconvex regularization and TGV regularization.

A variational model for image restoration is usually composed of a data-fitting term and a regularization term. Typically, the regularization parameter multiplied in the fidelity term handles the tradeoff of a fidelity term and a regularization term. That is, a small value of it leads to over-smoothing of fine features such as edges and details, while a large value of it results in leftover noise in homogeneous regions. Therefore, spatially varying values for the regularization parameter, i.e., small values in homogeneous parts and large values in textural parts, are more appropriate for denoising. In fact, the spatially adaptive regularization parameter (SARP) approach has been proposed in many works [31, 29, 44, 7, 1, 22] for various denoising models. Gilboa et al. [29] proposed a parameter update scheme based on local variance measures; however, it was only suitable for Gaussian noise removal. The idea was later extended to deal with multiplicative noise [44], where the proposed algorithm focused on evolving the negative gradient flow based on the AA model. However, the model converges slowly and requires many iterations for satisfactory results. In particular, Dong et al. [22] proposed a new SARP approach for the additive Gaussian noise removal with a theoretical analysis. This approach was extended for the denoising problems with other types of noise [34, 16, 47]. We in this dissertation also extend this SARP approach for the removal of heavy multiplicative Gamma noise.

CHAPTER 1. **INTRODUCTION**

In the last decade, many efficient optimization algorithms for convex minimization problems have been proposed [30, 14, 8, 70]. The alternating direction method of multipliers (ADMM) [8, 70] is the most commonly used algorithms for convex problems in image processing due to its convergence and wide applicability. It is known that ADMM is equivalent to the split Bregman method [63] under linear equality constrained optimization problems. Despite its effectiveness, this algorithm usually requires inner iterations or inverse operations involving the Laplacian operator at each iteration. The computational cost of inner iterations or inversions are considerably high. Therefore, many linearized techniques have been developed [56, 57] for accelerating alternating algorithms that do not involve any inner iteration or inversion. Recently, in [69], a fast proximal linearized alternating direction (PLAD) algorithm was proposed for solving the multiplicative noise removal models in [65, 67]. This algorithm linearized both data-fitting and quadratic terms in the augmented Lagrangian function, and also demonstrated that the linearized algorithm outperforms the original augmented Lagrangian algorithm. On the other hand, nonconvex optimization algorithms have not been studied as much as convex ones because of its intrinsic difficulties arisen from nonconvexity. Nevertheless, several numerical algorithms for nonconvex problems have been proposed in [2, 4, 66] with or without convergence analysis. Recently, Candes, et al. [10] introduced a new algorithm, called the iteratively reweighted ℓ_1 algorithm (IRLA), to solve the compressive sensing problems involving a nonconvex regularization. Furthermore, Ochs et al. [53] extended it to solve linearly constrained optimization problems in computer vision problems, which was also generalized as various kinds of iteratively reweighted algorithms [54] with convergence analysis. In this work, we adopt the IRLA in [53] to handle our nonconvex model, and the ADMM to solve a convex subproblem.

In this dissertation, we propose a variational model with local constraints for restoring images corrupted by heavy multiplicative Gamma noise. The local constraint involves multiple local windows rather than one local window as in [17], which helps in effectively removing the noise both in homogeneous and edge regions. The proposed models are related to the exp model [48] associated with the SARP. Thus, the proposed models enable us to handle heavy multiplicative Gamma noise as well as to benefit from the advantages of the SARP scheme. For the first proposed model, the convergence analysis such as the existence and uniqueness of a solution is provided. Furthermore, we derive our SARP algorithm from the first optimality characterization of our model. Lastly, we utilize the PLAD algorithm for solving our subproblem; this results in a fast optimization algorithm for solving the proposed model. The second proposed model is based on the nonconvex TGV (NTGV) regularization. Despite, we can not guarantee theoretical analysis because of nonconvexity, NTGV has a good property such as keeping edges sharply and discontinuous feature.

The remainder of this paper is organized as follows: Section 2 recalls convex and nonconvex regularizers, several variational models for multiplicative Gamma noise removal and a proximal linearized alternating minimization algorithm. In Section 3, we introduce our variational models as well as an optimization algorithm for solving our model. We also present numerical results for our models and compare them with some state-of-the art models. Lastly, we conclude this paper in Section 4.

Chapter 2

Previous works

2.1 Variational models for image denoising

Generally, variational models for image denoising consists are composed of data-fidelity term and regularization term. In this section, we explore several existing regularizers for image denoising and introduce various variational models for multiplicative noise removal.

2.1.1 Convex and nonconvex regularizers

This subsection recalls several existing regularizers. First, the total variation (TV) regularizer [62] was introduced in a variational model for the Gaussian noise removal:

$$\min_u \frac{\lambda}{2} \int_\Omega (u-f)^2 dx + |u|_{\mathrm{BV}(\Omega)}, \tag{2.1.1}$$

where $\lambda > 0$ is a tuning parameter that balances data-fitting and regularization terms. Here, $\mathrm{BV}(\Omega)$ is the subspace of functions $u \in L^1(\Omega)$ such that the following quantity, namely, the BV semi-norm $|u|_{\mathrm{BV}(\Omega)}$, is finite:

$$|u|_{\mathrm{BV}}(\Omega) := \int_\Omega |Du| = \sup\left\{ \int_\Omega u \mathrm{div}(\phi) dx \,\middle|\, \phi \in C_c^1(\Omega), \|\phi\|_\infty \leqslant 1 \right\}, \tag{2.1.2}$$

where the vector measure Du represents the distributional or weak gradient of u, and $\|\cdot\|_\infty$ is the essential supremum norm. If $u \in W^{1,1}(\Omega)$, then $\int_\Omega |Du| = \int_\Omega |\nabla u|\, dx$, where $|\nabla u| = \sqrt{u_{x_1}^2 + u_{x_2}^2}$ with $x = (x_1, x_2)$. This regularization is also called the TV of u; it has been widely used owing to its discontinuity or edges preserving. Note that, the space $\mathrm{BV}(\Omega)$ is a Banach space equipped with the norm $\|u\|_{\mathrm{BV}(\Omega)} = \|u\|_{L^1(\Omega)} + |u|_{\mathrm{BV}(\Omega)}$.

To enhance the edge-preserving ability of TV, several nonconvex TV regularizers were proposed in [37, 52], which has the form $\Phi(|\nabla u|) = \int_\Omega \phi(|\nabla u|)dx$, where ϕ is the nonconvex function defined as

$$\phi(s) = s^q \ (0 < q < 1)\,, \quad \frac{\rho s^2}{1+\rho s^2}\,, \quad \frac{1}{\rho}\log(1+\rho s) \ (\rho > 0). \tag{2.1.3}$$

Numerical results in [52] exhibited that the nonconvex TV regularizers better preserved edges or textures than TV. However, the nonconvex TV regularizers smooth homogeneous regions like TV, which indicates that they can yield some staircasing artifacts near smooth transition regions in restored images.

To overcome these staircasing effects, higher-order regularization based models were suggested in [13, 15, 50]. As an early work, a inf-convolution TV (ICTV) model was proposed in [13], which takes the infimal convolution of TV and second-order TV:

$$\min_{u_1,u_2} \frac{\lambda}{2}\int_\Omega (u_1+u_2-f)^2 dx + \int_\Omega |\nabla u_1| + \alpha|\nabla^2 u_2|\, dx, \ \text{with } u_1+u_2 = u, \tag{2.1.4}$$

where $| \nabla^2 u_2 | = \sqrt{(u_2)^2_{x_1x_1} + (u_2)^2_{x_1x_2} + (u_2)^2_{x_2x_1} + (u_2)^2_{x_2x_2}}$ and $\alpha > 0$ is a weight parameter.

Moreover, Li et al. [45] proposed the following denoising model, involving a convex combination of TV and the second order TV as a regularizer:

$$\min_u \frac{\lambda}{2}\int_\Omega (u-f)^2 dx + \int_\Omega (1-g)|\nabla u| dx + \int_\Omega g|\nabla^2 u| dx, \tag{2.1.5}$$

where $g = \frac{1}{1+\|\nabla(G_\sigma * f)\|_2^2}$ is an edge detector, where G_σ is a Gaussian kernel with standard deviation σ.

Oh et al. [55] further extended the model (2.1.5) by making use of a nonconvex hybrid TV regularizer:

$$\min_u \frac{\lambda}{2}\int_\Omega (u-f)^2 dx + \int_\Omega (1-g)|\nabla u|^{\alpha_1}\, dx + \int_\Omega g|\nabla^2 u|^{\alpha_2}\, dx, \tag{2.1.6}$$

where $\alpha_i \in (0,1)$ are tuning parameters that control the nonconvexity of regularization terms. The authors showed that the nonconvex hybrid TV regularizer is more suitable for the image denoising problem than the convex hybrid TV (2.1.5) or a nonconvex TV.

On the other hand, as a generalization of the ICTV, the total generalized variation (TGV) regularizer was proposed in [9]. Particularly, the second-order TGV based model is as follows:

$$\min_{u} \frac{\lambda}{2}\int_{\Omega}(u-f)^2 \; dx + \mathrm{TGV}^2(u), \tag{2.1.7}$$

$$\text{with} \qquad \mathrm{TGV}^2(u) = \min_{\mathbf{p}} \int_{\Omega} \alpha_1 |\nabla u - \mathbf{p}| + \alpha_0 |\mathcal{E}(\mathbf{p})| \; dx,$$

where $\mathcal{E}(\mathbf{p}) = \frac{1}{2}\left(\nabla \mathbf{p} + (\nabla \mathbf{p})^T\right)$ represents the distributional symmetrized derivative, and α_1, $\alpha_0 > 0$ are the weighted parameters that control the balance between the first and second-order terms. From the formulation (2.1.7) of TGV, it can be interpreted that $\mathrm{TGV}^2(u)$ can automatically find an appropriate balancing between the first and the second-order derivative of u with respect to α_i.

Recently, Ochs et al. [54] proposed a nonconvex extension of the TGV regularizer as follows:

$$\min_{u,\mathbf{p}} \frac{\lambda}{2}\int_{\Omega}(u-f)^2 dx + \int_{\Omega} \alpha_1 \phi(|\nabla u - \mathbf{p}|) + \alpha_0 \phi(|\mathcal{E}(\mathbf{p})|) dx, \tag{2.1.8}$$

where $\phi(x) = \frac{1}{\rho}\log(1+\rho x)$ with the parameter $\rho > 0$ controlling the nonconvexity of regularization term. This regularization takes advantages of both noconvex regularization and TGV regularization.

2.1.2 Variational models for multiplicative noise removal

In this subsection, we review existing variational models for multiplicative Gamma noise removal. First, based on a MAP estimator, Aubert and Aujol (AA) [5] proposed a new TV-based model for removing multiplicative Gamma noise:

$$\min_{u>0} \lambda \int_{\Omega} \left(\log u + \frac{f}{u}\right) dx + \int_{\Omega} |\nabla u| dx, \tag{2.1.9}$$

where $\lambda > 0$ is a tuning parameter that balances data-fitting and regularization terms. The main defect of model (2.1.9) is that the data-fidelity term is not convex. Thus, classical optimization algorithms provide only a local minimum, which may not be the global optimal solution; moreover, the algorithms strongly rely on the initialization. To overcome this difficulty, Shi and Osher (SO) [65] adopted the log transformation, $z = \log u$, and proposed the following convex model:

$$\min_{z} \ \lambda \int_{\Omega} \Big(z + f e^{-z} \Big) \ dx + \int_{\Omega} |\nabla z| dx, \tag{2.1.10}$$

It was shown in the [65] that this model outperforms the AA model (2.1.9) and their results do not depend on initial guesses. Furthermore, to better preserve textures and details, this model was extended by Chen and Cheng [17], incorporating it with a spatially dependent regularization parameter $\lambda \in L^{\infty}(\Omega)$:

$$\min_{z} \ \int_{\Omega} \lambda(x) \Big(z + f e^{-z} \Big) \ dx + \int_{\Omega} |\nabla z| dx, \tag{2.1.11}$$

where $\lambda : \Omega \to \mathbb{R}$ is a spatially varying parameter. In [25], this convex data-fitting term was integrated with the TGV regularizer, leading to the following model:

$$\min_{u} \ \lambda \int_{\Omega} \big(u + f e^{-u} \big) \ dx + \mathrm{TGV}^2(u). \tag{2.1.12}$$

Different from the idea of the SO model, Dong and Zeng (DZ) [23] inserted a quadratic penalty term into the AA model (2.1.9) and proposed the following convex model:

$$\min_{u>0} \ \lambda \int_{\Omega} \Big[\log u + \frac{f}{u} + \alpha \left(\sqrt{\frac{u}{f}} - 1 \right)^2 \Big] \ dx + \int_{\Omega} |\nabla u| dx, \tag{2.1.13}$$

where $\alpha > 0$ is a parameter. It was shown in [23] that the objective function of (2.1.14) is strictly convex if $\alpha \geqslant \frac{2\sqrt{6}}{9}$. The penalty term was derived from the following statistical properties of multiplicative Gamma noise η with distribution (1.0.2): (I) $\lim_{M\to\infty} \mathbb{E}\Big\{(\frac{1}{\sqrt{\eta}} - 1)^2\Big\}$=0, (II) $\frac{1}{\sqrt{\eta}} = \sqrt{\frac{u}{f}}$. However, $\mathbb{E}\{(\sqrt{u/f})\}$ is always larger than 1 and is close to 1 only when M is large sufficiently. This indicates that this model is more appropriate for a relatively large value of M, which corresponds to a low noise level. Recently, Shamma et al. [64] proposed a variational model by combining the convex data-fidelity term in [23] with the TGV:

$$\min_{u} \lambda \int_{\Omega} \left[\log u + \frac{f}{u} + \alpha \left(\sqrt{\frac{u}{f}} - 1 \right)^2 \right] dx + \mathrm{TGV}^2(u), \tag{2.1.14}$$

To address considerable multiplicative Gamma noise, Lu et al. [48] substituted the value 1 in the quadratic penalty term in model (2.1.13) with the varying value $\beta \geqslant 1$. Furthermore, owing to the constraint $u > 0$ and the observation that exponent-like models usually provide better quality denoised images than their logarithm-like counterparts, the authors used the log transformation, $z = \log u$, and proposed the following model, called the exp model:

$$\min_{z} \ \lambda \int_{\Omega} \left[z + f e^{-z} + \alpha \left(\sqrt{\frac{e^{z}}{f}} - \beta \right)^{2} \right] dx + \int_{\Omega} |\nabla z| dx, \tag{2.1.15}$$

where β is no less than 1 and varies depending on the level of noise. The objective function of this model is strictly convex if

$$\alpha \beta^{4} \leqslant \frac{4096}{27}. \tag{2.1.16}$$

In this dissertation, we extend this model (2.1.15) to a TV model with local constraints and nonconvex extension of TGV with local constraints.

2.2 Proximal linearized alternating direction method of multipliers

This subsection recalls the proximal linearized alternating direction method of multipliers (PLAD) proposed in [69], which is adopted for solving our proposed model.

Let us consider the following TV-based convex minimization problem:

$$\min_{u} \ \{\lambda F(u) + \|\nabla u\|_{1}\}, \tag{2.2.1}$$

where F is a real-valued, convex, and differentiable function. Moreover, the gradient of F is assumed to be Lipschitz continuous with a Lipschitz constant $L_F > 0$: $\|\nabla F(u) - \nabla F(v)\|_2 \leqslant L_F \|u - v\|_2$, $\forall u, v \in \mathrm{dom}\ F$.

Using the variable splitting technique [21, 30], the unconstrained problem (2.2.1) can be converted into its equivalent constrained version as

$$\min_{u,d} \ \{\lambda F(u) + \|d\|_{1} \mid d = \nabla u\}. \tag{2.2.2}$$

The augmented Lagrangian function for problem (2.2.2) is given by

$$L_{\rho}(u, d, b) = \lambda F(u) + \|d\|_{1} \ + \langle b, d - \nabla u \rangle + \frac{\rho}{2} \|d - \nabla u\|_{2}^{2}, \tag{2.2.3}$$

where b is a Lagrange multiplier that can alternatively be regarded as the variables of the dual problem of (2.2.2), and $\rho > 0$ is a penalty parameter. The alternating direction method of multipliers (ADMM) [70, 71, 21, 30] for solving problem (2.2.2) is as follows:

$$\left\{ \begin{array}{lcl} u^{k+1} & = & \arg\min\limits_{u} \mathcal{L}_\rho(u, d^k, b^k), \\ d^{k+1} & = & \arg\min\limits_{z} \mathcal{L}_\rho(u^{k+1}, d, b^k), \\ b^{k+1} & = & b^k + \rho\left(d^{k+1} - \nabla u^{k+1}\right). \end{array} \right. \tag{2.2.4}$$

The ADMM is a well-known algorithm for solving linearly constrained convex minimization problems. However, in many cases, the subproblem for u does not have a closed form solution.

To address this issue, the authors in [69] replaced $G(u) = F(u) + \frac{\rho}{2}\|d - \nabla u\|_2^2$ in the first subproblem in (2.2.4) by its second-order Taylor series at $\hat{u}$ as follows:

$$G(\hat{u}) + \langle \nabla_u G(\hat{u}), u - \hat{u} \rangle + \frac{1}{2}(u - \hat{u})^T \nabla_u^2 G(\hat{u})(u - \hat{u}). \tag{2.2.5}$$

In addition, they substituted the Hessian matrix, $\nabla_u^2 G(\hat{u})$, with a positive definite diagonal matrix, $\frac{1}{\delta}\mathbf{I}$, for a small constant $\delta > 0$. Then, they updated u using the following linearized augmented Lagrangian function, $\mathcal{LL}_\alpha$, with the generalized proximal term as:

$$\mathcal{LL}_\alpha(u, d, b\,;\, \hat{u}) = G(\hat{u}) + \langle \nabla_u G(\hat{u}), u - \hat{u} \rangle + \frac{1}{2\delta}\|u - \hat{u}\|_2^2 + \|d\|_1 + \langle b, d - \nabla u \rangle, \tag{2.2.6}$$

where $\nabla_u G(\hat{u}) = \lambda \nabla F(\hat{u}) + \rho \operatorname{div}(d - \nabla \hat{u})$. To sum up, the PLAD algorithm proposed in [69] updates u using $\mathcal{LL}_\alpha$, instead of $\mathcal{L}_\alpha$, in ADMM framework (2.2.4), with the other steps remain the same as in (2.2.4):

$$\left\{ \begin{array}{lcl} u^{k+1} & = & \arg\min\limits_{u} \mathcal{LL}_\rho(u, d^k, b^k; u^k), \\ d^{k+1} & = & \arg\min\limits_{d} \mathcal{L}_\rho(u^{k+1}, d, b^k), \\ b^{k+1} & = & b^k + \rho\left(d^{k+1} - \nabla u^{k+1}\right). \end{array} \right. \tag{2.2.7}$$

The convergence of the PLAD algorithm was provided in [18] as follows:

Theorem 2.2.1. *Let (u^k, d^k, b^k) be the sequence generated by the PLAD algorithm with $\delta < \frac{1}{\lambda L_F + \rho\|\triangle\|_2}$, where $\triangle$ is the Laplacian operator. Then, the tuple (u^k, d^k, b^k) converges to $(\bar{u}, \bar{d}, \bar{b})$ that satisfies the Karush-Kuhn-Tucker optimality conditions of (2.2.2).*

In [18], the authors proved this theorem with the energy functional, $F(u) = u + fe^{-u}$, which is the data-fidelity of the SO model. However, we note that the only conditions required for the proof of this theorem are that F is convex and differentiable and ∇F is Lipschitz continuous.

Chapter 3

Proposed models

3.1 Proposed model 1 : exp TV model with SARP

In this section, we introduce our model and an optimization algorithm for solving our model. In particular, in subsection 3.1.1, we describe the local statistical characteristics of a random variable with respect to Gamma noise. In subsection 3.1.2, we propose a TV model with local constraints. We also present the first optimality characterizations of our model and show that our model is related to the exp model with a SARP. From this relationship, we derive our SARP algorithm in subsection 3.3, along with an efficient algorithm for solving our subproblem.

3.1.1 Derivation of our model

To derive our model, we first present some statistical properties of a Gamma random variable (RV) following distribution (2.1.15).

Lemma 3.1.1. *Let η be a Gamma RV with mean 1 and standard deviation $\frac{1}{\sqrt{M}}$. Consider the following function of η:*

$$I(\eta) = \eta - \log \eta + \alpha \left(\sqrt{\frac{1}{\eta}} - \beta \right)^2, \tag{3.1.1}$$

for any real numbers α and β. Then, the following estimate of the expected *value of $I(\eta)$ holds true for a large value of M:*

$$\begin{aligned}\mathbb{E}\{I(\eta)\} &= 1+\frac{1}{2M}+\frac{1}{12M^2}-\frac{5}{2M^3} \\ &\quad +\alpha\left(\frac{M}{M-1}-\frac{2\beta\sqrt{M}\Gamma(M-\frac{1}{2})}{\Gamma(M)}+\beta^2\right)+O(\frac{1}{M^3}),\end{aligned} \tag{3.1.2}$$

where $\frac{O(s)}{s}<\infty$.

Proof. Let $T(\eta)=\eta-\log\eta$. Then, as in [17], we can obtain

$$\mathbb{E}\{T(\eta)\}=1+\frac{1}{2M}+\frac{1}{12M^2}-\frac{5}{2M^3}+O(\frac{1}{M^3}). \tag{3.1.3}$$

Moreover, it was shown in [23] that

$$\mathbb{E}\left\{\frac{1}{\eta}\right\}=\frac{M}{M-1} \quad \text{and} \quad \mathbb{E}\left\{\frac{1}{\sqrt{\eta}}\right\}=\frac{\sqrt{M}\Gamma(M-\frac{1}{2})}{\Gamma(M)}. \tag{3.1.4}$$

Thus, we can easily attain the conclusion by the linearity of the expectation. □

Here, we assume that β satisfies the following condition:

$$\beta>\frac{\sqrt{M}\Gamma(M-1)}{\Gamma(M-\frac{1}{2})}>1, \tag{3.1.5}$$

where the value of $\frac{\sqrt{M}\Gamma(M-1)}{\Gamma(M-\frac{1}{2})}$ is decreasing as M increases, and it approaches 1 as $M\to\infty$.

Lemma 3.1.2. *Let η be a Gamma RV with mean 1 and standard deviation $\frac{1}{\sqrt{M}}$, and assume that β satisfies (3.1.5). Then, we have*
(a) If $d(x)=x-\log(1+x)$ for $x>0$, then $d(x)>0$ for $x>0$.
(b) $\mathbb{E}\left\{\left(\frac{a}{\sqrt{\eta}}-\beta\right)^2\right\}>\mathbb{E}\left\{\left(\frac{1}{\sqrt{\eta}}-\beta\right)^2\right\}$, *where* $0<a<1$.

Proof. (a) $\lim_{x\to0+}d(x)=0$ and $d'(x)=1-\frac{1}{1+x}>0$ for $x>0$. Therefore, d is a strictly increasing function, thus $d(x)>0$ for $x>0$.

(b) By the linearity of the expectation, it can be easily shown that the inequality in (b) is identical to the following inequality, $\mathbb{E}\left\{\frac{1}{\eta}\right\}/\mathbb{E}\left\{\frac{1}{\sqrt{\eta}}\right\}<$

$\frac{2\beta}{1+a}$. On the other hand, the equalities in (3.1.4) and the condition (3.1.5) for β yield

$$\mathbb{E}\left\{\frac{1}{\eta}\right\}/\mathbb{E}\left\{\frac{1}{\sqrt{\eta}}\right\} = \frac{\sqrt{M}\Gamma(M-1)}{\Gamma(M-\frac{1}{2})} < \beta < \frac{2\beta}{1+a}. \tag{3.1.6}$$

Therefore, the inequality in (b) can be obtained. □

From now on, we investigate the characteristic of the formula obtained by letting $\eta \approx \frac{f}{\tilde{u}}$ in the function (3.1.1):

$$g(\tilde{u}) = \frac{f}{\tilde{u}} - \log\frac{f}{\tilde{u}} + \alpha\Big(\sqrt{\frac{\tilde{u}}{f}} - \beta\Big)^2. \tag{3.1.7}$$

Let u_* be a clean and natural image defined on Ω. Assume that the image u_* can be decomposed into $u_* = u_c + u_t$, where u_c and u_t represent cartoon and texture regions, respectively. Then, the noisy image $f = u_* \cdot \eta$ corrupted by the Gamma noise η can be rewritten as $f = (u_c + u_t)\eta$. Generally, TV-based variational models pursue piecewise constant restored images. Hence, we can assume that the denoised image $\tilde{u}$ in a TV-based model is approximated by the cartoon component u_c, i.e., $\tilde{u} = u_c$. Under this assumption, we can obtain

$$g(\tilde{u}) = \eta - \log\eta + \left\{\frac{u_t}{u_c}\eta - \log\left(1 + \frac{u_t}{u_c}\right)\right\} + \alpha\left(\sqrt{\frac{u_c}{(u_c+u_t)\eta}} - \beta\right)^2. \tag{3.1.8}$$

Let Ω_c and Ω_t be cartoon and textural regions in Ω, respectively, and be assumed to be sufficiently large. In the region Ω_c, we have $u_t \approx 0$, which leads to

$$\begin{aligned} \frac{1}{|\Omega_c|}\int_{\Omega_c} g(\tilde{u}) &\approx \frac{1}{|\Omega_c|}\int_{\Omega_c}\left(\eta - \log\eta + \alpha\left(\sqrt{\frac{1}{\eta}} - \beta\right)^2\right)dx \\ &\approx \mathbb{E}\{I(\eta)\} \approx C, \end{aligned} \tag{3.1.9}$$

where $C = 1 + \frac{1}{2M} + \frac{1}{12M^2} - \frac{5}{2M^3} + \alpha\left(\frac{M}{M-1} - \frac{2\beta\sqrt{M}\Gamma(M-\frac{1}{2})}{\Gamma(M)} + \beta^2\right)$.

On the other hand, in the region Ω_t, we can have the following relations:

$$
\begin{aligned}
\frac{1}{|\Omega_t|}\int_{\Omega_t} g(\tilde{u}) &= \frac{1}{|\Omega_t|}\int_{\Omega_t}\left(\eta - \log\eta + \left\{\frac{u_t}{u_c}\eta - \log\left(1+\frac{u_t}{u_c}\right)\right\}\right.\\
&\qquad \left. +\alpha\left(\sqrt{\frac{u_c}{(u_c+u_t)\eta}} - \beta\right)^2\right) dx\\
&= \frac{1}{|\Omega_t|}\int_{\Omega_t}\left(\eta - \log\eta + \{s\eta - \log(1+s)\}\right.\\
&\qquad \left. +\alpha\left(\sqrt{\frac{1}{(1+s)\eta}} - \beta\right)^2\right) dx \qquad (3.1.10)\\
&> \frac{1}{|\Omega_t|}\int_{\Omega_t}\left(\eta - \log\eta + \alpha\left(\sqrt{\frac{1}{(1+s)\eta}} - \beta\right)^2\right) dx\\
&> \frac{1}{|\Omega_t|}\int_{\Omega_t}\left(\eta - \log\eta + \alpha\left(\sqrt{\frac{1}{\eta}} - \beta\right)^2\right) dx \approx \mathbb{E}\{I(\eta)\} \approx C,
\end{aligned}
$$

where $s = u_t/u_c$. The first inequality is derived from the Lemma 3.1.2-(a) and the property $\mathbb{E}\{\eta\} = 1$, and the second inequality is obtained from the Lemma 3.1.2-(b).

3.1.2 Proposed TV model with local constraints

Based on the arguments in Subsection 3.1, we make use of the local expected value estimator of $g(\tilde{u})$ in (3.1.7) as a constrained term for the denoised image $\tilde{u}$. As in [17], we define a local window centered at pixel x as $\Omega_x^r = \left\{y \mid \|x-y\|_\infty \leqslant \frac{r}{2}\right\}$, and a mean filter $w_r(x,y)$ as

$$
w_r(x,y) = \begin{cases} \frac{1}{|\Omega_x^r|}, & \text{if } \|y-x\|_\infty \leqslant \frac{r}{2},\\ 0, & \text{else.}\end{cases} \tag{3.1.11}
$$

Then, the local expected value estimator of $g(\tilde{u})$ at x can be defined as

$$
\int_\Omega w_r(x,y)\Big[\frac{f}{\tilde{u}} - \log\frac{f}{\tilde{u}} + \alpha\Big(\sqrt{\frac{\tilde{u}}{f}} - \beta\Big)^2\Big](y)\,dy. \tag{3.1.12}
$$

Next we take the log transformation, $u = \log(\tilde{u})$, in (3.1.12), leading to

$$S_r(u)(x) = \int_\Omega w_r(x,y)\bar{q}(u)(y)dy, \tag{3.1.13}$$

which is the local expected value estimator of the function $\bar{q}(u)$

$$\bar{q}(u) = u + fe^{-u} - \log f + \alpha\left(\sqrt{\frac{e^u}{f}} - \beta\mathbf{1}\right)^2. \tag{3.1.14}$$

Using the formula (3.1.13), we can obtain the following TV minimization problem with local constraints:

$$\min_u \quad J(u) = \int_\Omega |Du|, \qquad \text{s.t.} \qquad S_r(u) \leqslant C \quad \text{a.e. in } \Omega, \tag{3.1.15}$$

where C is a constant value defined after equation (3.1.9). Note that the exponential of the solution u of this model, i.e. e^u, exhibits the denoised image from the data f.

Now we assume $\alpha > 0$ and relax the condition (3.1.5) for β to be $\beta \geqslant 1$. If we further assume that α and β satisfy the condition (2.1.16), then the model (3.1.15) is an extension of the exp model in (2.1.15) to a constrained model with local constraints. We here further extend the model (3.1.15) by adopting multiple local windows, instead of using one local window as in [17]. Therefore, we propose the following model with the local constraints involving multiple local windows:

$$\min_u \quad J(u) = \int_\Omega |Du|, \qquad \text{s.t.} \qquad S(u) \leqslant C \quad \text{a.e. in } \Omega, \tag{3.1.16}$$

where $S(u)$ is the local expected value estimator of $\bar{q}(u)$ with multiple local windows as

$$S(u) = \frac{1}{N}\sum_{i=1}^{N} S_{r_i}(u) = \frac{1}{N}\sum_{i=1}^{N}\int_\Omega w_{r_i}(x,y)\bar{q}(u)(y)dy. \tag{3.1.17}$$

This idea comes from the observation that a small local window leads to denoised images with remaining noise in homogeneous regions, while a large local window derives denoised images with over-smoothed details and small features, which was shown in [17]. Fig 3.1 shows the efficiency of using multiple local windows rather than using one local window. From (a) to (c), we use one local window with r = 9, 17, 31, respectively. It can be seen that the denoised image in (a) has well-preserved edges but still contains noise in homogeneous background regions. In contrast, the denoised images in (b) and (c) have well-denoised background areas, but they keep much noises near edges, especially in the tripod part. On the other hand, we can observe that the image in (d) denoised by using multiple local windows take advantages of multiple sizes of local windows, resulting in well-denoised in both homogeneous and edge regions.

Existence and uniqueness of solutions of model (3.1.16)

In this subsection, we prove the existence and uniqueness of a solution of our model (3.1.16). Let us define a mean filter $w(x,y)$ involving multiple local windows as

$$w(x,y) = \frac{1}{N}\sum_{i=1}^{N} w_{r_i}(x,y). \tag{3.1.18}$$

Then, $S(u)$ in (3.1.17) becomes

$$S(u) = \int_\Omega w(x,y)\bar{q}(u)\ dy. \tag{3.1.19}$$

The following lemma provides the lower bound for the local expected value estimator $S(u)$, which is independent of u.

Lemma 3.1.3. *Assume that $\alpha > 0$ and $\beta \geqslant 1$ satisfy the conditions in (2.1.16). Then, there exists a constant $K' \in \mathbb{R}$ such that*

$$S(u)(x) \geqslant K' \ \ \textit{for any} \ \ x \in \Omega. \tag{3.1.20}$$

Proof. We define $p(s) := s - \log s + \alpha\left(\frac{1}{\sqrt{s}} - \beta\right)^2$, for $s > 0$. By [48, Theorem 2.4.], there exists unique $k' > 0$ such that $p(k') \leqslant p(s)$ for all $s > 0$. Let $K' = p(k')$. By substituting s by f/e^u, we can obtain

$$S(u)(x) = \int_\Omega w(x,y)p(\frac{f}{e^u})dy \geqslant K' \geqslant s - \log s \geqslant 1. \tag{3.1.21}$$

□

By Lemma 3.1.3, it is easy to check that the following feasible set is closed and convex:

$$\mathcal{C} = \{u \in \mathrm{BV}(\Omega) \mid S(u) \leqslant C \ \ \text{a.e. in} \ \ \Omega\}. \tag{3.1.22}$$

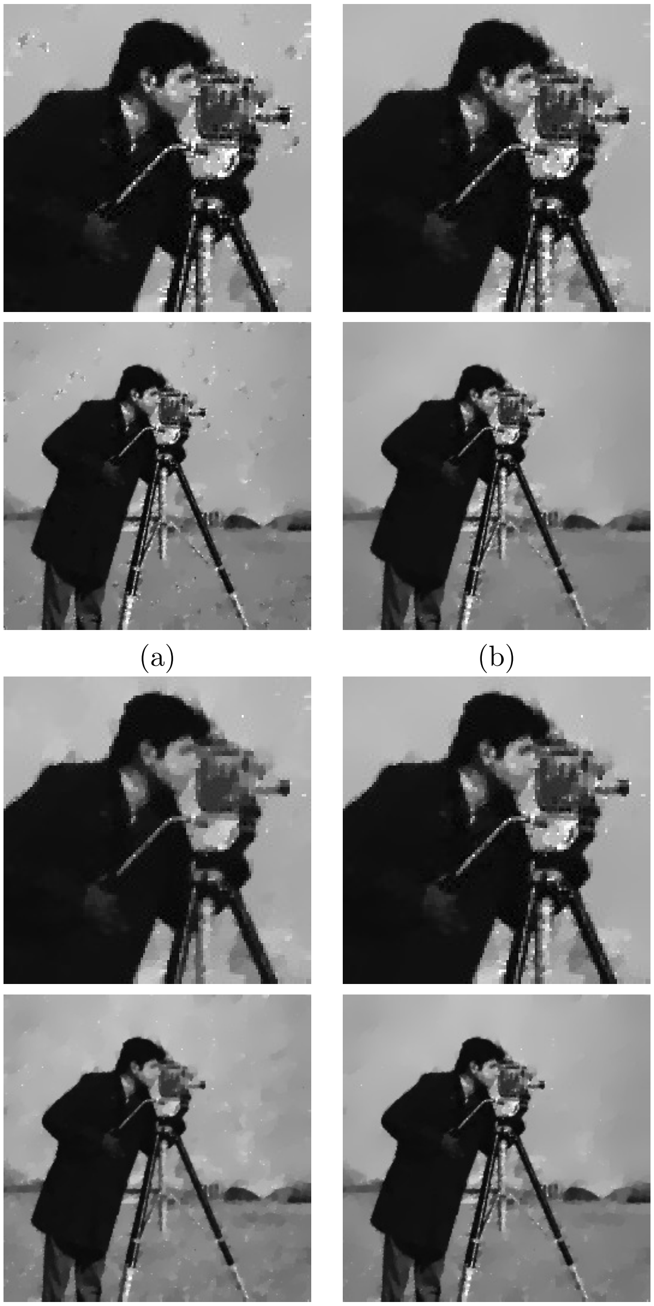

(a) (b)

(c) (d)

Figure 3.1: Denoised images with different size of local windows w_r. (a) $r = 7$ (b) $r = 17$ (c) $r = 256$ (d) $r = 7, 21, 256$.

In the following, we prove the existence and uniqueness of a solution of our model (3.1.16). First of all, we define the following functional

$$E(u) = J(u) + \int_\Omega S(u)(x)\,dx. \tag{3.1.23}$$

Theorem 3.1.1. *(Existence) Assume that* $\alpha > 0$ *and* $\beta \geqslant 1$ *satisfy the condition (2.1.16). Let* $f_{\min}$ *and* f_{max} *be two positive constants such that* $f \in [f_{\min}, f_{\max}]$. *Then,* $\|u\|_{BV(\Omega)} \to \infty$ *implies* $E(u) \to \infty$. *Moreover, the model (3.1.16) admits a solution.*

Proof. Let $L(u) = J(u) + \frac{1}{N}\sum_{r_i=1}^{N}\int_\Omega\int_\Omega w_{r_i}(x,y)(fe^{-u} + u - \log f)\,dydx$. Then, the functional $E(u)$ is rewritten as $E(u) = L(u) + \frac{\alpha}{N}\sum_{r_i=1}^{N}\int_\Omega\int_\Omega w_{r_i}(x,y) \times \left(\sqrt{\frac{e^u}{f}} - \beta\mathbf{1}\right)^2 dydx$. In [17, Theorem 1], it was shown that $L(u)$ with one local window goes to ∞ as $\|u\|_{\mathrm{BV}(\Omega)} \to \infty$. Thus, we can easily extend this result for $L(u)$ with multiple local windows. Furthermore, since $E(u) \geqslant L(u)$ for all $u \in \mathrm{BV}(\Omega)$, $E(u) \to \infty$ as $\|u\|_{\mathrm{BV}(\Omega)} \to \infty$, which indicates the BV-coercivity of $E(u)$.

To show the existence of solutions of model (3.1.16), let $\{u_n\}$ be a minimizing sequence in $\mathcal{C}$, where $\mathcal{C}$ is defined in (3.1.22). Since $S(u)$ is bounded, then $E(u)$ is bounded. In addition, due to the coercivity of E, we can conclude that the sequence $\{u_n\}$ is bounded in $\mathrm{BV}(\Omega)$. Then, by the compactness of $\mathrm{BV}(\Omega)$ [6], there exists a subsequence $\{u_{n_k}\}$ of $\{u_n\}$ and $\bar{u} \in \mathrm{BV}(\Omega)$ such that u_{n_k} weakly* converges in $\mathrm{BV}(\Omega)$ to $\bar{u}$. Moreover, since $J(u)$ is weakly lower semi-continuous with respect to the topology in $\mathrm{BV}(\Omega)$, we have

$$J(\bar{u}) \leqslant \liminf_{k\to\infty} J(u_{n_k}) = \inf_{u\in\mathcal{C}} J(u). \tag{3.1.24}$$

Because $\mathcal{C}$ is closed and convex, we have $\bar{u} \in \mathcal{C}$. Therefore, $\bar{u}$ is a solution of model (3.1.16). $\square$

For the uniqueness of the solution of model (3.1.16), we assume the following modified mean filter $\tilde{w}_{r_i}(x,y)$ instead of a mean filter $w_{r_i}(x,y)$ in (3.2.5) :

$$\tilde{w}_{r_i}(x,y) = \begin{cases} \frac{1}{w_{r_i}}, & \text{if } \|x-y\|_\infty \leqslant \frac{r_i}{2}, \\ \epsilon_i, & \text{else.} \end{cases}$$

where, $0 < \epsilon_i \ll \min(1, \frac{1}{w_{r_i}})$, and w_{r_i} satisfying $\int_\Omega \tilde{w}_{r_i}(x,y)dy = 1$.

Theorem 3.1.2. *(Uniqueness) Assume that the assumptions in Theorem 3.1.1 hold true. Furthermore, we assume that* $c\chi_\Omega \notin \mathcal{C}$ *for any constant c,* *where* $\chi_\Omega = 1$ *for* $x \in \Omega$*. Then, the solution of the model (3.1.16) is unique.*

Proof. $q(s) = s + fe^{-s} - \log f + \alpha \left\| \sqrt{\frac{e^s}{f}} - \beta \mathbf{1} \right\|_2^2$ is strictly convex by the assumption of α, β. Let z_1 and z_2 be two solutions of (3.1.16) in $\mathrm{BV}(\Omega)$. Define $\tilde{z} = \frac{1}{2}(z_1 + z_2)$. By the convexity of $q(s)$, we have $q(\tilde{z}) \leqslant \frac{1}{2}(q(z_1) + q(z_2))$.
Case 1) If $q(\tilde{z}) = \frac{1}{2}(q(z_1) + q(z_2))$ a.e. in Ω , then $z_1 = z_2$ by the strictly convexity of $q(z)$.
Case 2) If there exist $\tau > 0$ and $\Omega_\tau \subset \Omega$ with $|\Omega_\tau| > 0$, such that

$$q(\tilde{z}) \leqslant \frac{1}{2}(q(z_1) + q(z_2)) - \tau \quad \text{a.e. in } \Omega_\tau \tag{3.1.25}$$

Define $\epsilon_\tau = \epsilon_0 \tau |\Omega_\tau|$. Take multiplication a modified mean filter $w(x, y)$ and integral over Ω to (3.1.25), we get

$$S(\tilde{z})(x) \leqslant \frac{1}{2}(S(z_1)(x) + S(z_2)(x)) - \epsilon_\tau \leqslant C - \epsilon_\tau \quad \text{a.e in } \Omega$$

Let define $z_\theta = \theta\tilde{z}$ for $\theta \in [0, 1]$. Since $S(\cdot)$ is continuous, then $z_\theta \in \mathcal{C}$ for some θ close to 1. If $\int_\Omega |\nabla \tilde{z}| dx \neq 0$, then $\int_\Omega |\nabla z_\theta| dx = \theta \int_\Omega |\nabla \tilde{z}| dx < \int_\Omega |\nabla \tilde{z}| dx$ for any $\theta \in [0, 1)$. Since $\tilde{z}$ is a minimizer, $\int_\Omega |\nabla \tilde{z}| dx = 0$. This implies that $\tilde{z} \equiv c\chi_\Omega$ for some constant c. It is a contradiction to assumption $c\chi_\Omega \notin \mathcal{C}$ for any constant c. Thus there is no subset Ω_τ with $|\Omega_\tau| > 0$ such that $q(\tilde{z}) \leqslant \frac{1}{2}(q(z_1) + q(z_2)) - \tau$ a.e. in Ω for all positive τ. It implies that $z_1 = z_2$ a.e. in Ω. □

First-order optimality characterization of a solution of model (3.1.16)

This subsection exhibits the first order optimality condition of a solution of model (3.1.16). This shows that the constrained minimization problem in (3.1.16) is relevant to the following TV model with a spartially adaptive regularization parameter $\lambda \in L^2(\Omega)$:

$$\min_{u \in \mathrm{BV}(\Omega)} \int_\Omega \lambda(x) q(u)\, dx + J(u), \tag{3.1.26}$$

where $q(u) = u + fe^{-u} + \alpha \left(\sqrt{\frac{e^u}{f}} - \beta \mathbf{1} \right)^2$. From this relation, we derive an optimization algorithm for our model (3.1.16), which will be illustrated in the next subsection.

First, we consider the following penalty problems as

$$\min_{u \in \mathrm{BV}(\Omega)} L_\mu(u) = J(u) + \mu \int_\Omega (\max(S(u) - C, 0))^2 \, dx, \tag{3.1.27}$$

where μ is a positive penalty parameter. Then, we obtain

Theorem 3.1.3. *Let the assumptions of Theorem 3.1.1 still hold. Then, the penalty problem (3.1.27) admits a solution* $u_\mu \in BV(\Omega)$ *for any positive constant* μ*. Moreover, as* $\mu \to \infty$*,* $\{u_\mu\}$ *converges along a subsequence weakly in* L^2 *to a solution of (3.1.16), and the following equation holds:* $\|\max(S(u_\mu) - C, 0)\|_2 = o\left(1/\sqrt{\mu}\right)$*, where* $\lim_{s \to 0} o(s)/s = 0$*.*

Proof. Note that $S(\cdot)$ and $\max(\cdot, 0)$ are continuous and convex function, and $\int_\Omega |\nabla \cdot| dx$ is weakly lower semicontinuous in $\mathrm{BV}(\Omega)$. Let $z_n \in \mathrm{BV}(\Omega)$ be a minimizing sequence of $L_\mu(z)$. Let $\tilde{z}$ be a solution of (3.1.16). Since $dom(L_\mu) \supset \mathcal{C}$, we have

$$L_\mu(z_n) \leqslant L_\mu(\tilde{z}) + 1 = \int_\Omega |\nabla \tilde{z}| dx + 1 \quad \text{for large enough } n \in \mathbb{N}$$

Define $\Omega_+^n = \{x \in \Omega \mid S(z_n)(x) \geqslant C\}$ and $\Omega_-^n = \{x \in \Omega \mid S(z_n)(x) < C\}$. Then, we have

$$\begin{aligned} \int_{\Omega_+^n} (S(z_n) - C)^2 dx &= \int_\Omega \{\max(S(z_n) - C, 0)\}^2 dx \\ &\leqslant \int_\Omega \{\max(S(z_n) - C, 0)\}^2 dx + \int_\Omega |\nabla z_n| dx \\ &= L_\mu(z_n) \leqslant \int_\Omega |\nabla \tilde{z}| dx + 1 \quad \text{for large } n \end{aligned} \tag{3.1.28}$$

By triangular inequality,

$$\sqrt{\int_{\Omega_+^n} S(z_n)^2 dx} - \sqrt{\int_{\Omega_+^n} C^2 dx} \leqslant \sqrt{\int_\Omega |\nabla \tilde{z}| dx + 1} \quad \text{for large } n \in \mathbb{N} \tag{3.1.29}$$

Thus, we obtain

$$\|S(z_n)\|_{L^2(\Omega_+^n)} \leqslant \sqrt{\int_\Omega |\nabla \tilde{z}| dx + 1} + C\sqrt{|\Omega_+^n|} \leqslant \sqrt{\int_\Omega |\nabla \tilde{z}| dx + 1} + C\sqrt{|\Omega|} = C_1 \tag{3.1.30}$$

For Ω_-^n region, we have $1 \leqslant K' \leqslant S(z_n) < C$, here K' is a constant in Lemma 3.1.3. So $\|S(z_n)\|_{L^2(\Omega_-^n)} \leqslant C\sqrt{|\Omega_-^n|} \leqslant C\sqrt{|\Omega|} = C_2$.
Note that C_1, C_2 do not depend on n and μ. Thus, $\|S(z_n)\|_{L^2(\Omega)}$ is bounded for large n.
Since Ω is bounded domain, $\|S(z_n)\|_1$ is bounded by Holder's inequality. i.e. $\|S(z_n)\|_1 \leqslant \|S(z_n)\|_2|\Omega|$ for large n
If z_n is not bounded, then $\int_\Omega |\nabla z_n| dx \to \infty$ or $\int_\Omega S(z_n) dx \to \infty$ by Theorem 3.1.1 and it implies that L_μ is not bounded. So we conclude that z_n is bounded in BV(Ω). Now similar arguments as in proof of Theorem 3.1.1 claim the existence of a solution $z_\mu \in$ BV(Ω) for fixed μ.
Since $L_\mu(z_\mu) \leqslant J(\tilde{z})$, similar arguments in first part of the proof, we have the boundedness of z_μ in BV(Ω). Let $\tilde{z}_\mu$ be a weak limit of a subsequence of $z_\mu \in$ BV(Ω). Then by lower semicontinuity, we have

$$J(\tilde{z}_\mu) \leqslant \liminf_{k\to\infty} L_{\mu_k}(z_{\mu_k}) \leqslant J(\tilde{z}) = \inf_{z\in\mathcal{C}} J(z).$$

Next, it is necessary to show that $\tilde{z}_\mu \in \mathcal{C}$. Above inequality holds for all $\mu > 0$

$$\mu \int_\Omega \{\max(S(z_\mu) - C, 0)\}^2 dx \leqslant J(\tilde{z}) - J(z_\mu)$$

which is represented as

$$\int_\Omega \{\max(S(z_\mu) - C, 0)\}^2 dx \leqslant \frac{J(\tilde{z}) - J(z_\mu)}{\mu} \to 0 \quad \text{as } \mu \to \infty$$

So we have

$$\|\max(S(z_\mu) - C, 0)\|_2 = \mathcal{O}\left(\frac{1}{\sqrt{\mu}}\right)$$

By weak lower semicontinuity and Fatou's Lemma, we obtain $\tilde{z}_\mu \in \mathcal{C}$ such that

$$\int_\Omega \{\max(S(\tilde{z}_\mu) - C, 0)\}^2 dx \leqslant \liminf_{k\to\infty} \int_\Omega \{\max(S(z_{\mu_k}) - C, 0)\}^2 dx = 0$$

Therefore,we have $\max(S(\tilde{z}_\mu) - C, 0) = 0$ a.e. in Ω, which means $S(\tilde{z}_\mu) \leqslant C$ a.e. in Ω. □

In the succeeding results, we present the first order optimality characterization of a solution $\bar{u}$ of problem (3.1.16), and we show that $\bar{u}$ is also a solution of the TV model (3.1.26) with some λ. Let us first define λ_μ° and

λ_μ as

$$\lambda_\mu^\circ = \mu \max(S(u_\mu) - C, 0), \qquad \lambda_\mu = \int_\Omega w(x,y)\lambda_\mu^\circ \, dx. \tag{3.1.31}$$

Then, we have

$$\begin{aligned} \mu \| \max(S(u_\mu) - C, 0)\|_2^2 &= \int_\Omega \lambda_\mu^\circ (S(u_\mu) - C)\, dx \\ &= \int_\Omega \lambda_\mu q(u_\mu)\, dx - C_\mu, \end{aligned} \tag{3.1.32}$$

where $C_\mu = C \int_\Omega \lambda_\mu^\circ \, dx$.

From (3.1.27) and (3.1.32) and the results in Theorem 3.1.3, we obtain the following subsequences for the relationship of the problems (3.1.16) and (3.1.26):

Theorem 3.1.4. *Let the assumptions of Theorem 3.1.1 hold and $\bar{u}$ denote a weak limit point of $\{u_{\mu_n}\}$ in L_2 as $\mu_n \to \infty$. Moreover, we assume that $\|u_{\mu_n}\|_{L^2} \to \|\bar{u}\|_{L^2}$ as $\mu_n \to \infty$ and that there exists a constant $h > 0$ such that $\|\lambda_{\mu_n}^o\|_{L^1} \leqslant h$ for any $n \in \mathbb{N}$. Then, there exist $\bar{\lambda} \in L^\infty(\Omega)$, a bounded Borel measure $\bar{\lambda}^\circ$, and a subsequence $\{\mu_{n_k}\}$ such that*

(a) $\lambda_{\mu_{n_k}}$ weakly converges to $\bar{\lambda}$ in $L^\infty(\Omega)$ and $\bar{\lambda} \geqslant 0$ a.e. in Ω.*

(b) There exists $j(\bar{u}) \in \partial J(\bar{u})$ such that

$$\langle j(\bar{u}), v\rangle + \int_\Omega \bar{\lambda} q'(\bar{u}) v \; dx = 0, \quad \text{for all } \; v \in \; BV(\Omega). \tag{3.1.33}$$

(c) $\int_\Omega \psi d\lambda_{\mu_{n_k}}^o \to \int_\Omega \psi d\bar{\lambda}^o$ for all $\psi \in C(\bar{\Omega})$, $\bar{\lambda}^o \geqslant 0$, and

$\int_\Omega \lambda_{\mu_n}^o (S(u_{\mu_n}) - C) \; dx \to 0.$

Proof. (a) Since $w_i \in L^\infty(\Omega)$, we have $\lambda_{\mu_n} \in L^\infty(\Omega)$ from the similar arguments in the proof of Theorem 3.1.1. Thus, $\int_\Omega \lambda_{\mu_n} f \, dx$ is well-defined for all $f \in L^1(\Omega)$. Then, from the assumption, there exists $C' > 0$, which is independent of μ_n, such that

$$\begin{aligned} \|\mu_n\|_{L^\infty(\Omega)} &\leqslant \mu_n \, \|w(x,y)\|_{L^\infty(\Omega\times\Omega)} \left\| \max\left(\frac{1}{N} \sum_{i=1}^{N} S_{w_i}(u_{\mu_n}) - C, 0 \right) \right\|_{L^1(\Omega)} \\ &\leqslant C', \end{aligned} \tag{3.1.34}$$

where the boundedness of the second term comes from the proof of Theorem 3.1.1. By Banach-Alaoglu theorem [19], we obtain

$$\int_\Omega \lambda_{\mu_{n_k}} f dx \to \int_\Omega \bar{\lambda} f dx \quad \text{for all } f \in L^1(\Omega), \tag{3.1.35}$$

which proves the first statement. The non-negativity of $\bar{\lambda}$ is obtained from the non-negativity of λ_μ and λ_{μ_n}.

(b) The boundedness of $\{u_{\mu_n}\}$ in $\mathrm{BV}(\Omega)$ can be obtained from the proof of Theorem 3.1.1. Moreover, due to the continuity of $J(\cdot)$, we attain the uniform boundedness of $\partial J(\cdot)$ with respect to μ_n. On the other hand, the first-order optimality condition for problem (3.1.27) is given by

$$0 \in \partial J(u_{\mu_n}) + \mu_n \left(\frac{1}{N} \sum_{i=1}^N S'_{w_i}(u_{\mu_n}) \right)^* \max\left(S_w(u_{\mu_n}) - C, 0\right), \tag{3.1.36}$$

where $S'(\cdot)^*$ denote the adjoint operator of $S'(\cdot)$ and $S_w(\cdot) = \frac{1}{N}\sum_{i=1}^N S_{w_i}(\cdot)$. Then, the boundedness of $\{u_{\mu_n}\}$ and $\{\partial J(u_{\mu_n})\}$ in $\mathrm{BV}(\Omega)$ and $\mathrm{BV}^*(\Omega)$, respectively, yields that

$$\mu_n \left\| \left(\frac{1}{N} \sum_{i=1}^N S'_{w_i}(u_{\mu_n}) \right)^* \max\left(S_w(u_{\mu_n}) - C, 0\right) \right\|_{\mathrm{BV}^*(\Omega)} \leqslant C'', \tag{3.1.37}$$

for some constant C'' independent of μ_n. Moreover, for $v \in \mathrm{BV}(\Omega)$, we have

$$\begin{aligned}
&\mu_n \left\langle \left(\frac{1}{N} \sum_{i=1}^N S'_{w_i}(u_{\mu_n}) \right)^* \max\left(S_w(u_{\mu_n}) - C, 0\right), v \right\rangle_{\mathrm{BV}^*(\Omega),\mathrm{BV}(\Omega)} \qquad (3.1.38)\\
= &\int_\Omega \mu_{n_k} \max\Big(S_w(u_{\mu_{n_k}}) - C, 0\Big) \left[\frac{1}{N} \sum_{i=1}^N S'_{w_i}(u_{\mu_n}) \right] v dx \\
= &\int_\Omega \lambda^o_{\mu_{n_k}} \frac{1}{N} \left\{ \int_\Omega w_1(x,y)[\bar{q}'(u_{\mu_{n_k}})v](y) dy + \cdots \right. \\
&\qquad\qquad\qquad \left. + \int_\Omega w_N(x,y)[\bar{q}'(u_{\mu_{n_k}})v](y) dy \right\} dx \\
= &\int_\Omega \int_\Omega \lambda^o_{\mu_{n_k}} \left(\frac{w_1(x,y) + \cdots + w_N(x,y)}{N} \right) [\bar{q}'(u_{\mu_{n_k}})v](y) dy dx
\end{aligned}$$

$$
\begin{aligned}
&= \int_\Omega [\bar{q}'(u_{\mu_{n_k}})v](y) \int_\Omega \lambda^o_{\mu_{n_k}} w(x,y)dxdy \\
&= \int_\Omega \lambda_{\mu_{n_k}} [\bar{q}'(u_{\mu_{n_k}})v](y)dy \\
&= \int_\Omega [(\bar{q}'(u_{\mu_{n_k}}) - \bar{q}'(\tilde{u}))v](y)\lambda_{\mu_{n_k}} dy + \int_\Omega [\bar{q}'(\bar{u})v](y)(\lambda_{\mu_{n_k}} - \tilde{\lambda})dy \\
&\qquad + \int_\Omega [\bar{q}'(\bar{u})v](y)\tilde{\lambda}dy.
\end{aligned}
$$

Since $\bar{u}$ is a weak limit of $\{u_{\mu_n}\}$ in L^2 and $\|u_{\mu_n}\|_{L^2} \to \|\bar{u}\|_{L^2}$, we have that

$$\int_\Omega [(\bar{q}'(u_{\mu_{n_k}}) - \bar{q}'(\bar{u}))v](y)\lambda_{\mu_{n_k}} dy \to 0 \quad \text{as} \quad k \to \infty. \tag{3.1.39}$$

Therefore, as $k \to \infty$, we have that

$$\mu_n \left\langle \left(\frac{1}{N} \sum_{i=1}^N S'_{w_i}(u_{\mu_n}) \right)^* \max\left(S_w(u_{\mu_n}) - C, 0\right), v \right\rangle_{\mathrm{BV}^*(\Omega),\mathrm{BV}(\Omega)} \to \int_\Omega [\bar{q}'(\bar{u})v](y)\tilde{\lambda}dy. \tag{3.1.40}$$

(c) Based on the boundedness of $\lambda^o_{\mu_n}$ and [3], we have $\psi d\lambda^o_{\mu_{n_k}} \to \int_\Omega \psi d\bar{\lambda}^o$, The non-negativity of $\bar{\lambda}^o$ comes from the definition of λ^o_μ. Finally, by Theorem 3.1.3,

$$\left| \int_\Omega \lambda^o_{\mu_n} (S(u_{\mu_n}) - C)\, dx \right| = \mu_n \|\max(S(u_{\mu_n}) - C, 0)\|^2_{L^2(\Omega)} \to 0 \quad \text{as} \quad n \to \infty. \tag{3.1.41}$$

□

As a result, it can be observed from Theorem 3.1.3 and Theorem 3.1.4-(b) that a solution of the constrained problem (3.1.16) satisfies the first order optimality condition of the TV model (3.1.26) with $\lambda = \bar{\lambda}$. Besides, assuming that the last result in Theorem 3.1.3 still holds with $o(1/\mu)$ in place of $o(1/\sqrt{\mu})$, we can conclude from (3.1.31) that $\{\lambda^\circ_{\mu_n}\}$ is uniformly bounded in $L^2(\Omega)$, thus $\bar{\lambda}^\circ$ is the weak limit of the subsequence $\lambda^\circ_{\mu_n}$. And, if the last statement in Theorem 3.1.4-(c) holds, then we can obtain

$$\bar{\lambda}^\circ(S(\bar{u}) - C) = 0 \quad \text{a.e. in} \quad \Omega, \tag{3.1.42}$$

because of that $\bar{\lambda}^\circ \geqslant 0$ and $S(\bar{u}) - C \leqslant 0$. The equation (3.1.42) indicates that $\bar{\lambda}^\circ$ is just the Lagrangian multiplier of the Lagrangian function of the constrained problem (3.1.16). Therefore, we can utilize a updating rule for $\bar{\lambda}^\circ$ like the Lagrangian multiplier update rule, which will be used in the next subsection.

3.1.3 A SARP algorithm for solving model (3.1.16)

Now we present an optimization algorithm for solving our model (3.1.16), following the SARP strategy discussed in Subsection 3.1.2. Similar to [17], we utilize an adjustment approach similar to the Lagrangian multipliers update based approach for λ in (3.1.26). Initially, a small constant value of $\lambda > 0$ is chosen, which results in an over-smoothed restored image without details retained. However, since we have that $S_u(x) > C$ in the textured regions, we observe that the value of λ would need to be increased. Therefore, from (3.1.31) and assuming that $\bar{\lambda}^k$ denotes the current estimate of $\bar{\lambda}^\circ$ in (3.1.42), the update rules for λ can be derived as follows:

$$\begin{aligned} \bar{\lambda}^{k+1} &= \bar{\lambda}^k + \tau \max(S_{u^k}(x) - C, 0), & (3.1.43) \\ \lambda^{k+1} &= \int_\Omega w(x,y)\bar{\lambda}^{k+1}(x)\, dx, & (3.1.44) \end{aligned}$$

where $\tau > 0$ is a step size, and u^k is the current estimate of the original logarithmic image u. That is, u^k is a solution of problem (3.1.26) with fixed λ^k, i.e.,

$$u^k := \arg \min_{u \in \mathrm{BV}(\Omega)} \int_\Omega \lambda^k(x)\, q(u)\, dx + J(u). \qquad (3.1.45)$$

Consequently, the SARP algorithm for our model, (3.1.16), is summarized in Algorithm 1.

Solving for the u-subproblem (3.1.46)

Now, we focus on solving the u-subproblem in (3.1.46). In this work, we adopt the PLAD algorithm described in Subsection 2.2 for solving problem (3.1.46). First, however, let us prove the following theorem:

Lemma 3.1.4. *Let $f \in L^\infty(\Omega)$ with $\inf_\Omega f > 0$. Assume that $\alpha > 0$ and $\beta \geqslant 1$ hold for condition (2.1.16). A solution u of problem (3.1.46) for fixed $\lambda^k : \Omega \to \mathbb{R}$ satisfies*

$$\inf_\Omega \log(t_{\alpha,\beta}^2 f) \leqslant u \leqslant \sup_\Omega \log(t_{\alpha,\beta}^2 f),$$

Algorithm 1 Proposed SARP algorithm for model (3.1.16)

```
**Parameter** : $\alpha$, $\beta$, $\tau$; the size $r_i$ of local windows ($i = 1, 2, ..., n$).
**Initialization** : $k = 0$, $\bar{\lambda}^k = \lambda^k = \lambda^0 = c$ with a small constant value $c > 0$.
**while** a stopping condition is satisfied **do**
    Solve the discrete version of the problem
        $u^k := \arg \min_{u \in \mathrm{BV}(\Omega)} \left\{ \int_\Omega \lambda^k \left\{ u + f e^{-u} + \alpha \left( \sqrt{\frac{e^u}{f}} - \beta \right)^2 \right\} dx + J(u) \right\}. \quad (3.1.46)$
    Based on $u^k$, update $\lambda^k$ as follows:
        Calculate $S^{r_i}_{u^k}(x)$ for all $i \in \{1, 2, \cdots, n\}$,
        $\bar{\lambda}^{k+1} = \bar{\lambda}^k + \tau \max \left( \frac{1}{n} \sum_{i=1}^{n} S^{r_i}_{u^k}(x) - C, 0 \right)$,
        $(\lambda^{k+1})_{i,j} = \frac{1}{n} \sum_{i=1}^{n} \left( \frac{1}{r_i^2} \sum_{(s,t) \in \Omega^{r_i}_{i,j}} (\bar{\lambda}^{k+1})_{s,t} \right).$
**end while**
**Final output** : $\tilde{u} = e^u$
```

where $t_{\alpha,\beta}$ *is the unique real solution of* $1 - \frac{1}{t^2} + \alpha(t^2 - \beta t) = 0$ *for* $t > 0$.

Proof. Let us consider a minimizing sequence $\{u_n\}$ of the problem (3.1.46). Define $\tilde{\gamma} = \inf(\log(t^2_{\alpha,\beta} f))$, $\tilde{\xi} = \sup(\log(t^2_{\alpha,\beta} f))$, and

$$V(u) = V_0(u) + J(u) \quad \text{and} \quad V_0(u) = \int_\Omega \lambda(x) q(u)\, dx. \tag{3.1.47}$$

For fixed $x \in \Omega$, let $v_0(s) = \lambda(x)\left\{s + f(x)e^{-s} + \alpha\left(\sqrt{\frac{e^s}{f(x)}} - \beta\right)^2\right\}$. Then, the function $v_0(s)$ has the unique minimum value at $s = \log(t^2_{\alpha,\beta} f(x))$. And, $v(s)$ is decreasing on $(-\infty, \log(t^2_{\alpha,\beta} f(x)]$ and increasing on $[\log(t^2_{\alpha,\beta} f(x)), \infty)$. This implies that if $M_1 \geqslant \log(t^2_{\alpha,\beta} f(x))$ and $M_2 \leqslant \log(t^2_{\alpha,\beta} f(x))$, then $v_0(\min(s, M_1)) \leqslant v_0(s)$ and $v_0(\max(s, M_2)) \leqslant v_0(s)$. This yields that

$$V_0(\inf(u, \tilde{\xi})) \leqslant V_0(u) \quad \text{and} \quad V_0(\sup(u, \tilde{\gamma})) \leqslant V_0(u).$$

Moreover, by Lemma 1 in [36], we have that $J(\inf(u, \tilde{\beta})) \leqslant J(u)$ and $J(\sup(u, \tilde{\alpha})) \leqslant J(u)$, which yields that

$$V(\inf(u, \tilde{\xi})) \leqslant V(u) \quad \text{and} \quad V(\sup(u, \tilde{\gamma})) \leqslant V(u). \tag{3.1.48}$$

On the other hand, assuming that $\tilde{\gamma} \leqslant u_n \leqslant \tilde{\xi}$, we have $\{u_n\} \in L^1(\Omega)$. Since $\{u_n\}$ is a minimizing sequence of V, $V(u_n)$ is bounded. And from the proof in Lemma 3.1.3, $V_0(u_n) \geqslant K$ for some constant K. Then, $J(u_n)$ is bounded, and thus u_n is bounded in BV(Ω). By the compactness of BV(Ω), there exists a subsequence $\{u_{n_k}\}$ of $\{u_n\}$ such that $u_{n_k} \to u$ in BV(Ω)-weak* and $u_{n_k} \to u$ in $L^1(\Omega)$-strong. Then, we can obtain that $\tilde{\gamma} \leqslant u \leqslant \tilde{\xi}$. Finally, due to the lower semi-continuity of $J(\cdot)$ and Fatou's lemma, u is a solution of (3.1.46). ☐

Based on the above lemma, in practice, we solve the following problem for u:

$$\min_{u \in \mathcal{U}} \int_\Omega \lambda^k \left\{u + fe^{-u} + \alpha\left(\sqrt{\frac{e^u}{f}} - \beta\right)^2\right\} dx + \int_\Omega |\nabla u|\, dx, \tag{3.1.49}$$

where $\mathcal{U} = \{u : \inf_\Omega \log(t^2_{\alpha,\beta} f) \leqslant u \leqslant \sup_\Omega \log(t^2_{\alpha,\beta} f)\}$. Using the variable splitting technique [30], we can reformulate problem (3.1.49) as the following constrained problem:

$$\min_{z,u} \{F(u) + \|z\|_1 \mid z = \nabla u,\ u \in \mathcal{U}\}, \tag{3.1.50}$$

where $F(u) = \int_\Omega \lambda \left\{ u + fe^{-u} + \alpha \left(\sqrt{\frac{e^u}{f}} - \beta \right)^2 \right\} dx$ with $\lambda = \lambda^k$.

Before applying the PLAD algorithm to problem (3.1.50), we prove the subsequent lemma, which is a necessary condition for the PLAD algorithm.

Lemma 3.1.5. *The function F in (3.1.50) with $\lambda \in L^\infty(\Omega)$ is differentiable and has a Lipschitz continuous gradient on $\mathcal{U}$.*

Proof. Let $h(u) := \nabla F(u) = \lambda \left(1 - \frac{f}{e^u} + \alpha \left(\frac{e^u}{f} - \beta \sqrt{\frac{e^u}{f}} \right) \right)$. By the mean value theorem, we have that for all $u, v \in \mathcal{U}$,

$$\|\nabla F(u) - \nabla F(v)\|_2 = \|h(u) - h(v)\|_2 = |h'(\tilde{u})| \|u - v\|_2 \leqslant \|\lambda\|_\infty L_q \|u - v\|_2, \tag{3.1.51}$$

where $\tilde{u} = tu + (1-t)v$ for some $t \in [0, 1]$, and $L_q = \sup_{\tilde{w} \in \mathcal{U}} |q'(\tilde{w})|$. By basic calculation, we can find an upper bound for L_q as follows:

$$\begin{aligned} L_q &= \sup \left| fe^{-u} + \alpha \left(\frac{e^u}{f} - \frac{\beta}{2} \sqrt{\frac{e^u}{f}} \right) \right| \leqslant \sup |fe^{-u}| + \alpha \sup \left| \frac{e^u}{f} - \frac{\beta}{2} \sqrt{\frac{e^u}{f}} \right| \\ &\leqslant \frac{f_{\max}}{t^2_{\alpha,\beta} f_{\min}} + \alpha \max \left(\frac{\alpha\beta^2}{16}, \frac{t^2_{\alpha,\beta} f_{\max}}{f_{\min}} - \frac{\beta}{2} \sqrt{\frac{t^2_{\alpha,\beta} f_{\max}}{f_{\min}}} \right). \end{aligned} \tag{3.1.52}$$

Define $\tilde{L} := \frac{f_{\max}}{t^2_{\alpha,\beta} f_{\min}} + \alpha \max \left(\frac{\alpha\beta^2}{16}, \frac{t^2_{\alpha,\beta} f_{\max}}{f_{\min}} - \frac{\beta}{2} \sqrt{\frac{t^2_{\alpha,\beta} f_{\max}}{f_{\min}}} \right)$. Then we have

$$\|\nabla_u F(u) - \nabla_u F(v)\|_2 \leqslant \|\lambda\|_\infty \tilde{L} \|u - v\|_2, \tag{3.1.53}$$

which proves the Lipschitz continuity of ∇F. □

As a consequence, we can apply the PLAD algorithm to the constrained problem, (3.1.50), which leads to the following iterative algorithm:

$$\left\{ \begin{aligned} u^{k,\ell+1} &= \arg\min_{u \in \mathcal{U}} \langle \lambda^k \nabla q(u^{k,\ell}) + \rho \operatorname{div}(z - \nabla u^{k,\ell}), u \rangle - \langle b^{k,\ell}, \nabla u \rangle \\ &\qquad + \tfrac{1}{2\delta} \|u - u^{k,\ell}\|_2^2, \\ z^{k,\ell+1} &= \arg\min_z \|z\|_1 + \langle b^{k,\ell}, z \rangle + \frac{\rho}{2} \|z - \nabla u^{k,\ell+1}\|_2^2, \\ b^{k,\ell+1} &= b^{k,\ell} + \rho \left(z^{k,\ell+1} - \nabla u^{k,\ell+1} \right), \end{aligned} \right. \tag{3.1.54}$$

where $\nabla q(u) = 1 - \frac{f}{e^u} + \alpha\left(\frac{e^u}{f} - \beta\sqrt{\frac{e^u}{f}}\right)$. The solution $u^{k,\ell+1}$ in (3.1.54) can be explicitly obtained as

$$u^{k,\ell+1} = P_{\mathcal{U}}\left(u^{k,\ell} - \delta\left[\lambda^k \nabla q(u^{k,\ell}) + \rho \mathrm{div}(z^{k,\ell} - \nabla u^{k,\ell}) + \mathrm{div} b^{k,\ell}\right]\right), \tag{3.1.55}$$

where $P_{\mathcal{U}}$ denotes the projection onto the set $\mathcal{U}$. In addition, the solution, $z^{k,\ell+1}$, in (3.1.54) is also attained using the following explicit formula:

$$z^{k,\ell+1} = shrink\left(\nabla u^{k,\ell+1} - \frac{b^{k,\ell}}{\rho}, \frac{1}{\rho}\right), \tag{3.1.56}$$

where *shrink* is a soft-thresholding operator defined as $shrink(a, b) = \frac{a}{\|a\|_2}\max(\|a\|_2 - b, 0)$. The iterative algorithm for solving the u-subproblem, (3.1.46), is summarized in Algorithm 4.

Algorithm 2 Solving the u-subproblem (3.1.46)

```
Parameter : $\rho > 0$, $\delta > 0$.
Initialization : $\ell = 0, u^{k,0} = u^{k-1}, z^{k,0} = \mathbf{0}, b^{k,0} = \mathbf{0}$.
while a stopping condition is satisfied do
    $u^{k,\ell+1} = \mathbf{P}_{\mathcal{U}}\left(u^{k,\ell} - \delta\left[\lambda^k \nabla q(u^{k,\ell}) + \rho \mathrm{div}(z^{k,\ell} - \nabla u^{k,\ell}) + \mathrm{div} b^{k,\ell}\right]\right)$,
    $z^{k,\ell+1} = shrink\left(\nabla u^{k,\ell+1} - \frac{b^{k,\ell}}{\rho}, \frac{1}{\rho}\right)$,
    $b^{k,\ell+1} = b^{k,\ell} + \rho\left(z^{k,\ell+1} - \nabla u^{k,\ell+1}\right)$.
end while
```

Lastly, we discuss the selection of the parameter δ in (3.1.55). To guarantee the convergence of $u^{k,\ell}$, the value of δ needs to satisfy the condition in Theorem 2.2.1. In our work, the parameter λ is not a constant, but it is assumed to be fixed for the u-subproblem. Hence, our iterative algorithm converges to a solution if the following condition is satisfied:

$$\delta < \frac{1}{\sup_\Omega(\lambda(x)) L_q + \rho\|\triangle\|_2}. \tag{3.1.57}$$

In practice, the parameter δ significantly affects the speed of the algorithm. In our case, L_q may play a crucial role with regard to the speed of the algorithm. The minimum value of a noisy image f corrupted by multiplicative Gamma noise is very small. This leads to a large value of L_q and a small value of δ, resulting in slow convergence. Thus, we want to replace L_q by its approximated value that is the expectation of the second derivative of $q(u)$, as suggested in [69]. It is the averaged estimation of L_q to avoid the worst estimation of L_q. For this, let us assume that e^u is closed to the original clean image. Then, we can compute

$$\begin{aligned}\mathbb{E}\{\nabla^2 q(u)\} &= \mathbb{E}\left\{\frac{f}{e^u}+\alpha\left(\frac{e^u}{f}-\frac{\beta}{2}\sqrt{\frac{e^u}{f}}\right)\right\}\approx\mathbb{E}\left\{\eta+\alpha\left(\frac{1}{\eta}-\frac{\beta}{2}\sqrt{\frac{1}{\eta}}\right)\right\}\\ &= 1+\alpha\left(\frac{M}{M-1}\right)-\alpha\beta\sqrt{M}\frac{\Gamma(M-\frac{1}{2})}{\Gamma(M)}=\tilde{C}.\end{aligned}$$

From this calculation, in practice, we set the value of δ as follows:

$$\delta=\frac{1}{2}\cdot\frac{1}{\sup_\Omega(\lambda(x))\tilde{C}+\rho\|\triangle\|_2}. \tag{3.1.58}$$

3.1.4 Numerical results

In this section, we test our model (3.1.16) on various natural images and SAR images that are presented in Figure 3.15 and we also display noisy images in Figure 3.3 that we will deal with. We compare the performance of our model with those of the SAR-BM3D model [59] and several TV-based state-of-the-art models; SO model [65], exp model [48], TV-SARP model [17] and TwL-mV model [35].

In the experiments, all the test images are contaminated by multiplicative Gamma noise for $M = 3$, 5, or 10. To quantify the effect of the models, we measure the Peak-Signal-to-Noise (PSNR) vaule and the Structural SIMilarity (SSIM) index [68]. The PSNR in dB is defined as PSNR $= 10\log_{10}\left(\frac{255^2 N_p}{\|u-u_*\|_2^2}\right)$, where u and u_* represent the recovered image and noise free image, respectively, and N_p is the total number of pixels.

For all the models, we tune the parameters to achieve the best denoised images with respect to the visual aspect as well as the PSNR and SSIM values. The stopping criterion is as follows, with respect to the relative error:

$$\frac{\|\tilde{u}^{\ell+1}-\tilde{u}^{\ell}\|_2}{\|\tilde{u}^{\ell+1}\|_2}<tol, \tag{3.1.59}$$

where $\tilde{u}^\ell$ displays the denoised image at iteration ℓ; $\tilde{u}=e^u$ for our model, the SO model, and the exp model, $\tilde{u}=u$ for the TV-SARP model and $\tilde{u}=u^m$ for the TwL-mV model. For our model and TV-SARP model, condition (3.1.59) is used for solving the u-subproblem, since the outer iteration number for both models is fixed as 3 which is the smallest iteration to provide enough result. The tolerance value tol is fixed as 10^{-4} for our model, the SO model,

Figure 3.2: Original images: (1st row) Cameraman (256×256), Parrot (256×256), Bird (256×256), Castle (321×481), (2nd row) Clock tower (321×481), Rectangle (215×215), Zebra (481×321), Butterfly (271×270), (3rd row) House (256×256), Remote1 (662×541), Remote2 (750×563), Remote3 (717×686), (4th row) Remote4 (640×452), Remote5 (200×200), Remote6 (256×256), Remote7 (400×400).

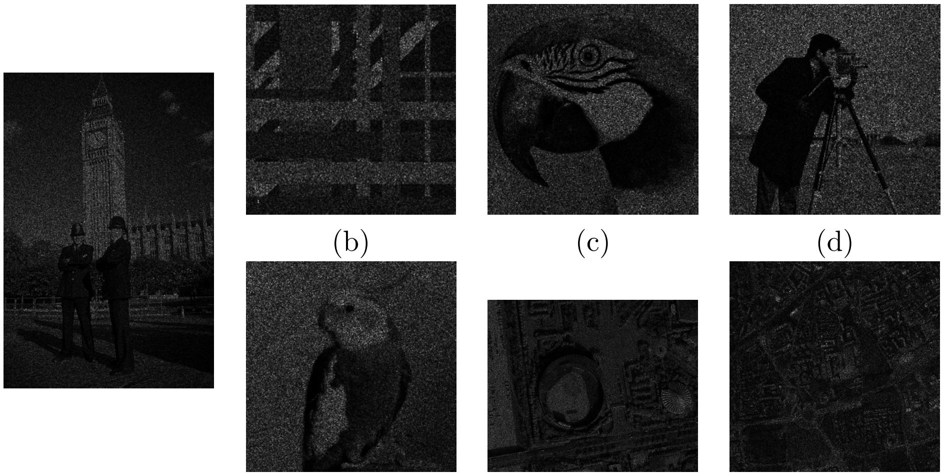

(a) (b) (c) (d) (e) (f) (g)

Figure 3.3: Noisy images: (a) Clock tower ($M = 5$) (b) Rectangle ($M = 3$) (c) Parrot ($M = 3$) (d) Cameraman ($M = 3$) (e) Bird ($M = 3$) (f) Remote1 ($M = 5$) (g) Remote2 ($M = 3$)

and the exp model, and $tol = 10^{-3}$ for the TV-SARP model and the TwL-mV model. Additionally, the maximum iteration number for ℓ is set to be 2000 for the SO and exp models and 500 for the TwL-mV, TV-SARP and our model.

For solving the SO model (2.1.10), we use the PLAD algorithm, as in [69]. For exp model (2.1.15), we follow the algorithm in [48], which is a fixed-point proximity algorithm. LPAMA is used to solve the TwL-mV model provided in [35].

The codes for the exp model, SO model, TV-SARP model and our model are written in Matlab, and we compute SAR-BM3D and TwL-mV models in C language with interface to Matlab through the mex function which are provided by the authors of [59, 35]. The experiments are implemented under Windows 7 with 64 bit and MATLAB R2014b running on an Intel i7-3770 CPU @ 3.40 GHz and 16GB Memory.

Parameter selection

In the exp model and our model, the value of β depends on the noise level. In both models, we fix $\beta = (1.9014, 1.3468, 1.0893)$ for $M = (3, 5, 10)$, respectively, based on the condition $\beta = \frac{1}{0.1113+0.1109M^2} + 1$ provided in [48]. In the

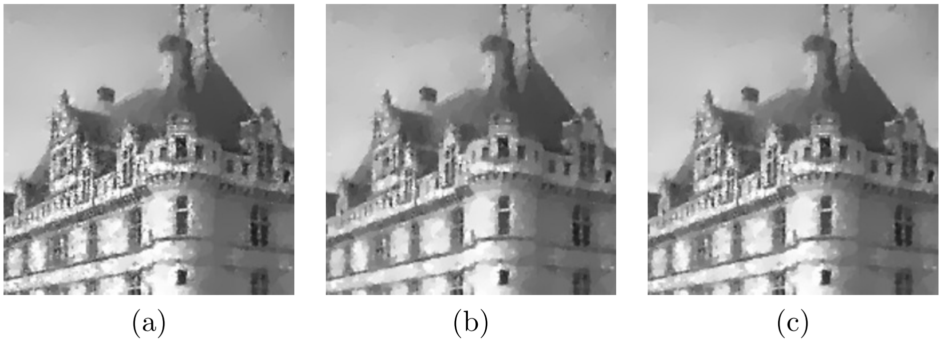

Figure 3.4: Denoised images with different number of windows and sizes. (a) $r = 7, 21$ (b) $r = 7, 321$ (c) $r = 7, 21, 321$

exp model, the value of α is heuristically selected satisfying the condition (2.1.16) and the condition in [48, Proposition 5.3], while in our model we choose it only within condition (2.1.16). The parameter λ is a tuning parameter that determines the smoothness of u; therefore, we select the value of it manually to attain satisfactory denoising results.

For the TV-SARP model, we basically implement the same parameter selection in [17], but we choose different values for some parameters because we treat heavier multiplicative noise than that handled in the TV-SARP model. Specifically, we choose the local window size $r = 17$, $\nu = 0.15$, and we increase the iteration number for the Chambolle projection method to be 12; see [17] for more details. Moreover, the initial regularization parameter λ^0 is set to be $(0.6\,, 0.8\,, 1)$ for $M = (3, 5, 10)$, respectively.

For the TwL-mV model, we select $m = 4$ owing to satisfactory denoised images with reasonable compatational cost as in [35]. We choose all parameters used in [35].

In our model, we use three local windows with $r_1 = 7$, $r_2 = 21$, $r_3 = \text{size}(f)$. In Figure 3.4, we compare the denoised images obtained by using two or three local windows. Figure (a) shows the denoised image when using two small windows, which still retains noise near edges. On the other hand, Figure (b) presents the denoised image when using one small and one large windows, where the textural regions are oversmoothed. However, as in (c), the denoised image when using three local windows, which is the combination of small, medium, large windows, preserves the texture parts while sufficiently removing noise near edges. We also note that the use of more than four windows is not necessary since it produces similar denoising results with when using three windows. Therefore, this example justifies the use of three different local windows rather than two local windows.

The initial constant value for λ is set to be the same as the TV-SARP model. In Algorithm 2, the value of ρ is fixed as 0.75 and the value of δ is computed as in (3.1.58).

Denoising results

First, in Figure 3.5, we present the denoising results of all mentioned models, tested on a natural image. The data f is contaminated by the multiplicative Gamma noise with $M = 5$. Since our model is an extension of the exp model with the SARP, it is expected that our model more adaptively removes the noise than the exp model. In fact, our model sufficiently denoises in homogeneous regions like the sky area while preserving details in textured regions such as the grass area. This is obtained from a suitable selection of the spatially adaptive regularization parameter in our model. On the other hand, the exp model inadequately eliminates the noise in homogeneous regions while also oversmoothing textures or details. These phenomena also happen in the SO and TwL-4V models that use fixed regularization parameters. Hence, this example validates the benefit of the SARP approach and the efficiency of our model for removing multiplicative Gamma noise. Moreover, comparing our model with the TV-SARP model, we can observe that the TV-SARP model tends to produce smoother denoised image than ours, so more details are preserved in our model, as seen in the grass area and window parts of the building. This can be more clearly seen in the zoomed images in Figure 3.8 (a). Lastly, we can observe the SAR-BM3D model better preserves textures than the other models, such as the repeated patterns in the building, leading to the highest PSNR value among all models. However, it produces undesirable artifacts in homogeneous regions, such as the sky area, and near the edges, which can be also shown in Figure 3.8 (a). On the contrary, our model yields clean homogeneous regions and sharp edges, that can be the advantages of our model over the SAR-BM3D model. Therefore, despite the better denoising performance of the SAR-BM3D model, our model is still meaningful in the sense that it outperforms the existing TV-based models, such as the exp, SO, TwL-4V, TV-SARP models, and moreover provides clean homogeneous regions and sharp edges, unlike the SAR-BM3D model that supplies unwanted artifacts in homogeneous regions and near edges.

In Figures 3.6 and 3.7, we compare our denoising results with those of other models, tested on a synthetic image and a natural image. The noisy images are contaminated with noise level $M = 3$, and the restored images


(a) (b) (c)

(d) (e) (f)

Figure 3.5: Denoising results of our model when $M = 5$ and comparisons with the exp [48], SO [65], TV-SARP [17], TwL-4V [35], SAR-BM3D [59] models. Denoised images with PSNR values: (a) exp (23.82) (b) SO (23.63) (c) TV-SARP (24.01) (d) TwL-4V (23.78) (e) SAR-BM3D (25.14) (f) our model (24.21)

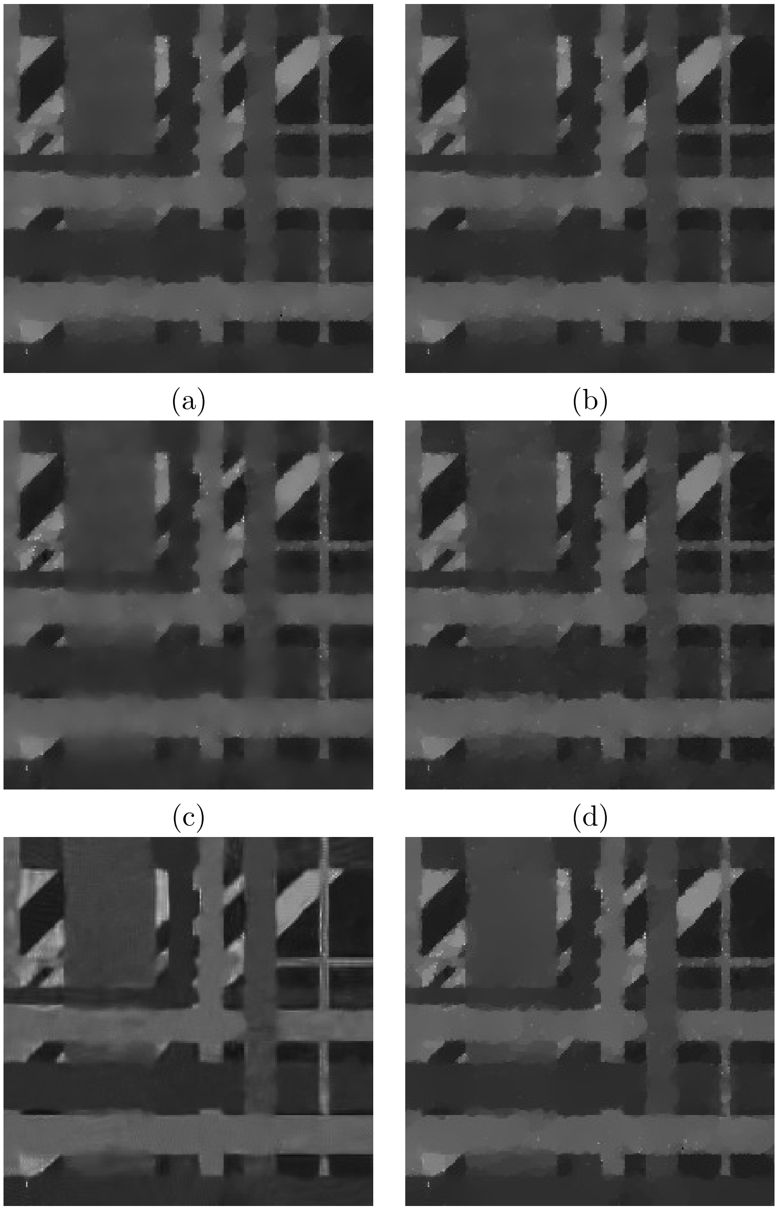

(a) (b)

(c) (d)

(e) (f)

Figure 3.6: Denoising results of our model when $M = 3$ and comparisons with the exp [48], SO [65], TV-SARP [17], TwL-4V [35], SAR-BM3D [59] models. Denoised images with PSNR values: (a) exp (28.09) (b) SO (27.71) (c) TV-SARP (27.42) (d) TwL-4V (27.77) (e) SAR-BM3D (28.94) (f) our model (28.32)

of all models are shown. Since the exp model includes a data-fidelity term that is suitable for heavy multiplicative noise, it brings the highest PSNR values among the variational models with fixed regularization parameters. Comparing our model, which is an extension of the exp model, with the TV-SARP model, it can be seen that the denoised images are visually distinguishable. This is a result of different local constraints used in these two models. In particular, the TV-SARP model tends to oversmooth the regions compared with ours; in Figure 3.6, our model produces sharp edges whereas the TV-SARP model provides some over-smoothed edges whcih can be seen in Figure 3.8 (b). In addition, in Figure 3.7, our model preserves more details than TV-SARP, especially in the areas of the beak and the head of the bird. We can also observe from the zoomed images in Figure 3.8 (c) that the TV-SARP model retains more noise in the textural parts than our model, while the head part is over-smoothed. Consequently, these examples show that our model performs better than the TV-SARP model for multiplicative noise removal. On the other hand, the SAR-BM3D model produces the better denoised images with the higher PSNR values than ours, however, it also results in some artifacts in homogeneous regions as well as near edges, while our model contributes to neat homogeneous regions and sharp edges. These also show the benefits and effectiveness of our model, compared to other state-of-the-art models.

In Figure 3.9, we display two final SARPs, $\lambda : \Omega \to \mathbb{R}$, obtained from Figures 3.5 and 3.7, respectively. It can be seen that the SARP, λ, has high values in the textural regions and edges and low values in the background and homogeneous regions. This indicates that the updating process for λ functions appropriately, and 3 outer iterations are enough to achieve the proper SARPs as well as the satisfactory denoising results.

Figures 3.10 and 3.11 present the denoising results of our model, with comparisons with SO, exp, TV-SARP, TwL-4V, and SAR-BM3D models. We consider the data f degraded by the heavy multiplicative noise with the noise level $M = 3$. In both figures, we can observe that the SARP based models (our model and TV-SARP) generate adequately denoised homogeneous regions with better conserved details than SO, exp, and TwL-4V models. In particular, in Figure 3.10, SO, exp, TwL-4V models smooth out the camera and tripod parts, while the SARP models maintain the details in those parts. Moreover, in Figure 3.11, all variational models seem to engender similar denoised images; however, the noise remains in the homogeneous regions in the denoised images of the SO, exp, and TwL-4V models. Indeed, we can adjust the regularization parameter in these models in order to remove the remaining noise in the homogeneous regions, but this may result

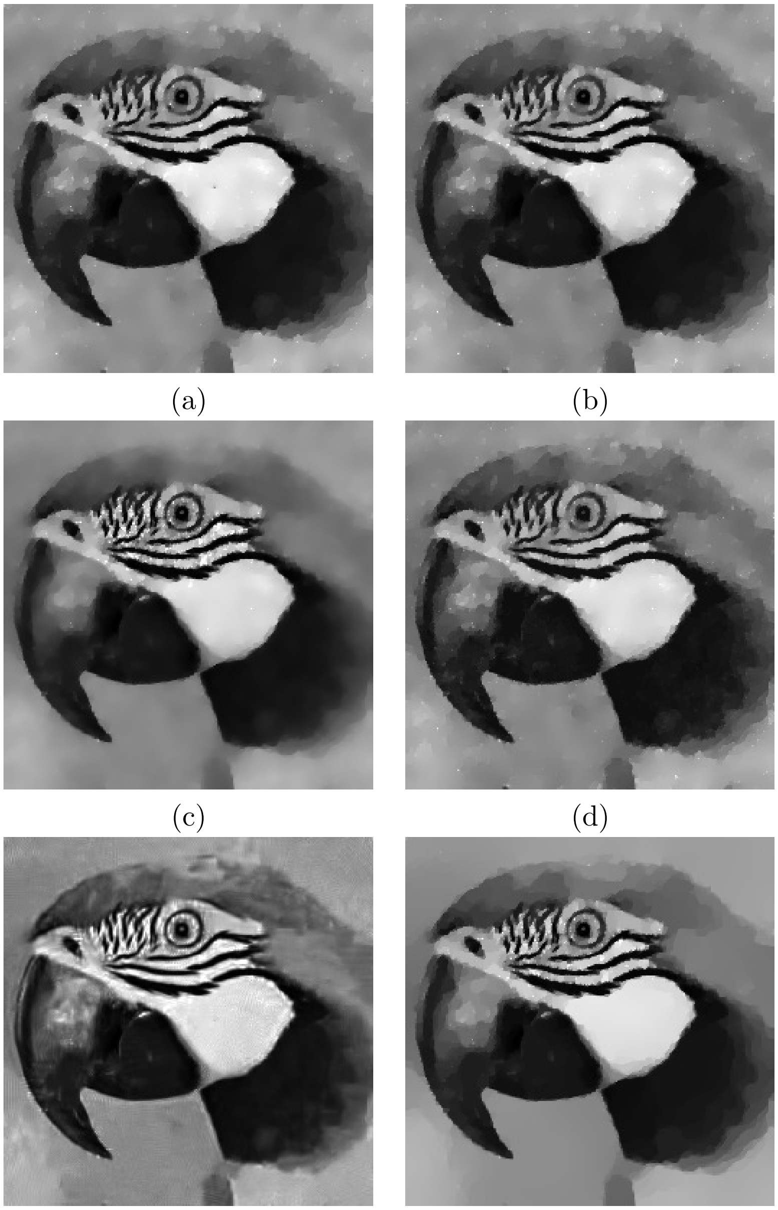

(a) (b)

(c) (d)

(e) (f)

Figure 3.7: Denoising results of our model when $M = 3$ and comparisons with the exp [48], SO [65], TV-SARP [17], TwL-4V [35], SAR-BM3D [59] models. Denoised images with PSNR values: (a) exp (23.01) (b) SO (22.52) (c) TV-SARP (22.70) (d) TwL-4V (22.60) (e) SAR-BM3D (24.39) (f) our model (23.23)

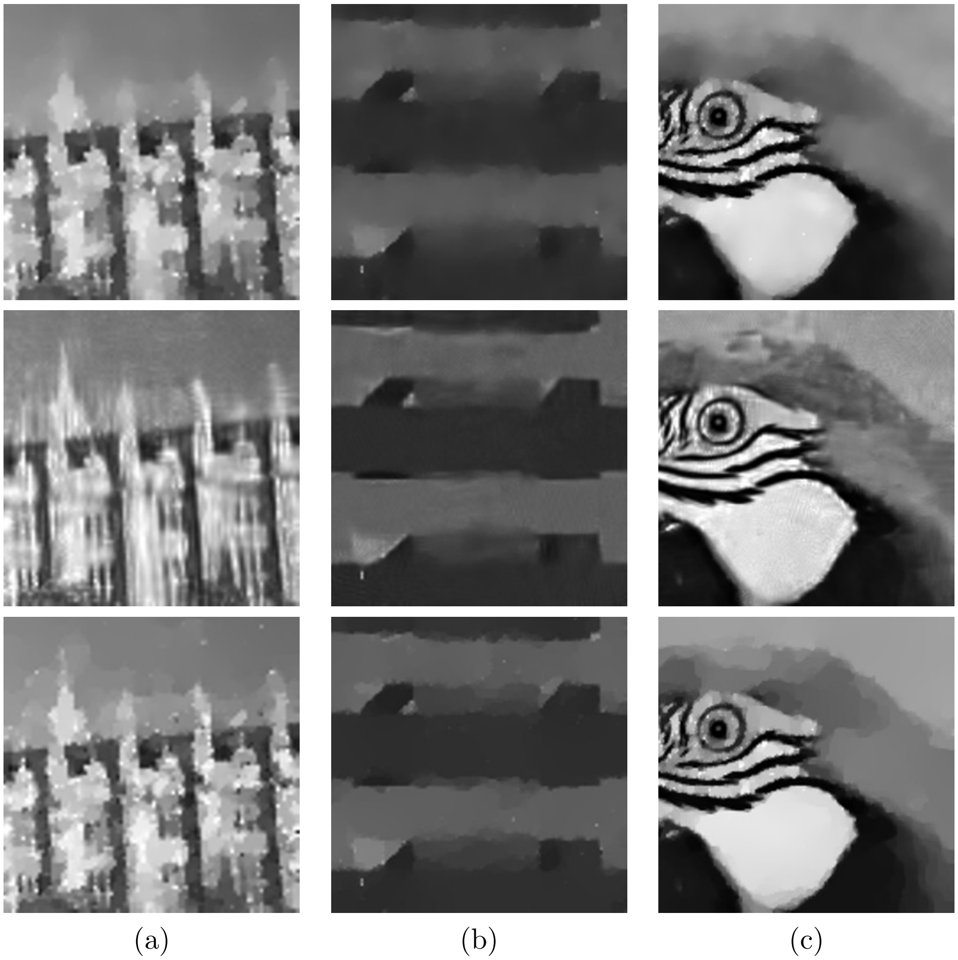

Figure 3.8: Zoomed denoised images in Figures 3.5, 3.6, 3.7. Top row: denoised images of TV-SARP [17]. Middle row: denoised images of SAR-BM3D [59]. Bottom row: denoised images of our model. (a) Figure 3.5, (b) Figure 3.6, (c) Figure 3.7.

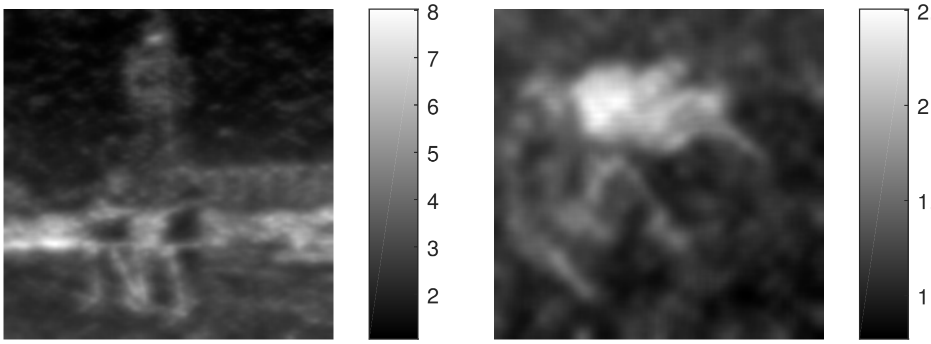

(a) (b)

Figure 3.9: Final SARP λ obtained from Figures 3.5 and 3.7: (a) Figure 3.5 ($M = 5$) (b) Figure 3.7 ($M = 3$)

in over-smoothed details. Thus, these examples also show the effectiveness of the SARP models in denoising. Comparing our model with the TV-SARP model, both models produce comparable denoised images. However, we observe that our model yields sharper and cleaner edges than the TV-SARP model, which can be observed in the zoomed images given in Figure 3.14 (a) and (b). Moreover, our model brings the highest PSNR and SSIM values among the TV-based models, as shown in Table 3.3. Nevertheless, the SAR-BM3D model preserves more details than ours, such as the camera and face areas in the Cameraman image and the bird's body in the Bird image, and furnishes the highest PSNR values among all models. However, we can also see that undesirable artifacts appear in the background and near edges in both examples, which can be also shown in the zoomed images in Figure 3.14.

In Figures 3.12 and 3.13, we test all the aforementioned models on SAR images. We consider noisy images with noise levels set at $M = 5, 3$ in Figures 3.12 and 3.13, respectively. Again, it can be observed that the SARP models (our model and TV-SARP) provide more effective denoising results than the others (SO, exp and TwL-4V), with satisfactorily smoothed homogeneous regions and well-retained details. Moreover, our model preserves more details than the TV-SARP model since the TV-SARP model oversmooths some small scales such as edges. This can be also seen in the zoomed images in Figure 3.14 (c) and (d). Therefore, these example also justify the predominance of our model over the other variational models such as the exp, SO, TwL-4V and TV-SARP models. However, the SAR-BM3D model exhibits the better reconstructed images with higher PSNR values than our model. Since the SAR images are dark and include very fine details, the artifacts that appeared in natural images are rather unnoticeable in the SAR images. Although the artifacts can be detected in the zoomed images in Figure 3.14, we admit the good denoising performance of the SAR-BM3D model on the SAR images. In spite of that, our model is also worthwhile since it has a merit of providing sharp edges and clean homogeneous regions.

In Tables 3.1, 3.2, 3.3, and 3.4 we quantify the denoising performance of different models and algorithms for natural images and SAR images in Figure 3.15. The tables list the PSNR, SSIM values, and the computational time for all models (exp, SO, TV-SARP, TwL-4V, SAR-BM3D, our model) with respect to the noise levels $M = 10$, 5, 3. We observe that our model provides the highest PSNR and SSIM values in nearly all examples, except the SAR-BM3D model. When it comes to the computational time, it is inevitable that the SARP models (our model and TV-SARP model) require more computing time than the others (exp, SO, TwL-4V) due to the additional updating step of the SARP λ in outer iterations. By comparing our model with the TV-SARP model, our model takes less computing time than the TV-SARP model, especially in the case of the heavy multiplicative noise such as $M = 3$. This is owing to the PLAD algorithm used for solving the u-subproblem since the outer iteration number is fixed as 3 for both models. The TwL-4V and SAR-BM3D models are written in C language, which is much faster than MATLAB. Although the SAR-BM3D model is written in C language, our model provides much faster computing time. In fact, the computational cost of the SAR-BM3D model is too expensive, compared to the other variational models. Therefore, our model also has a benefit of computational time over the SAR-BM3D model. Nonetheless, the SAR-BM3D model brings the highest image quality measurements in almost all examples. However, as discussed above, the SAR-BM3D model produces some undesirable artifacts in homogeneous regions and near edges, unlike our model. Lastly, we note that the SAR-BM3D model does not have any mathematical analysis, such as the existence or uniqueness of a solution, while our model involves the theoretical analysis. As a result, all these discussions validate the effectiveness our proposed model and the efficiency of our algorithm, compared to other state-of-the-art models.

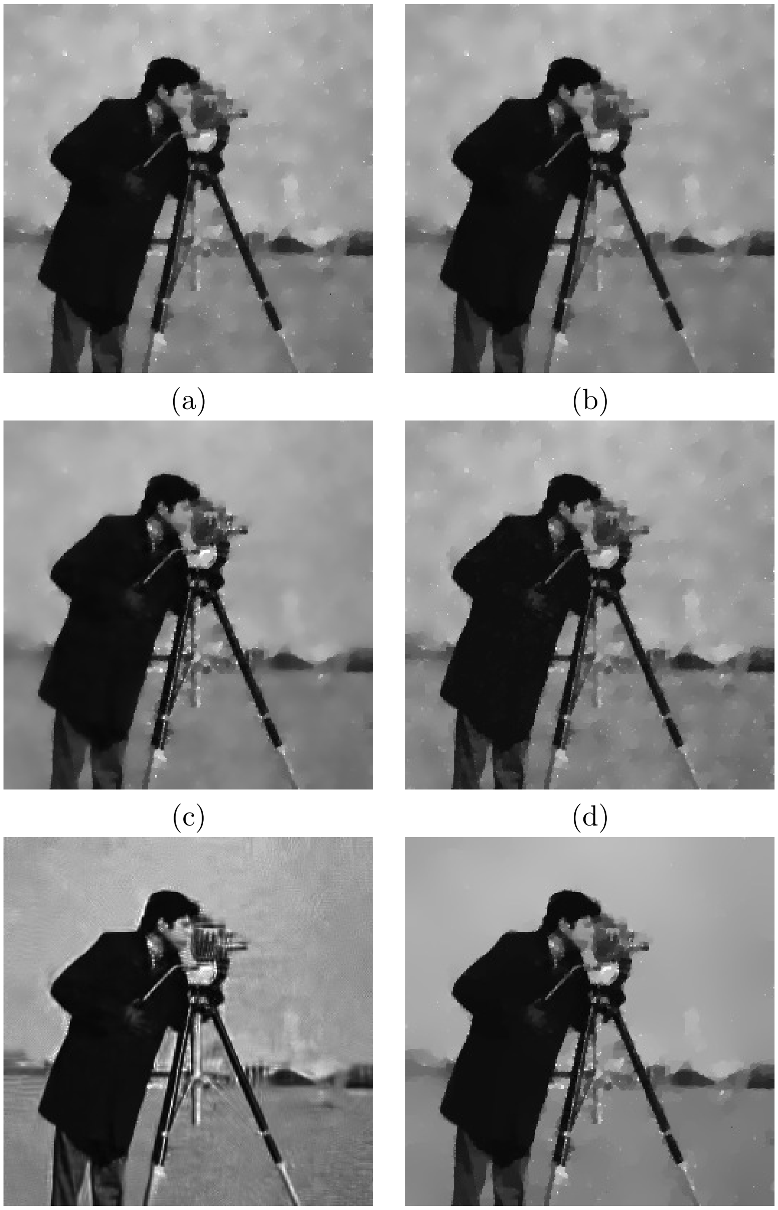

(a) (b)

(c) (d)

Figure 3.10: Denoising results of our model when $M = 3$ and comparisons with the exp [48], SO [65], TV-SARP [17], TwL-4V [35], SAR-BM3D [59] models. Denoised images with PSNR values: (a) exp (23.17) (b) SO (22.93) (c) TV-SARP (23.51) (d) TwL-4V (23.28) (e) SAR-BM3D (24.93) (f) our model (23.57)

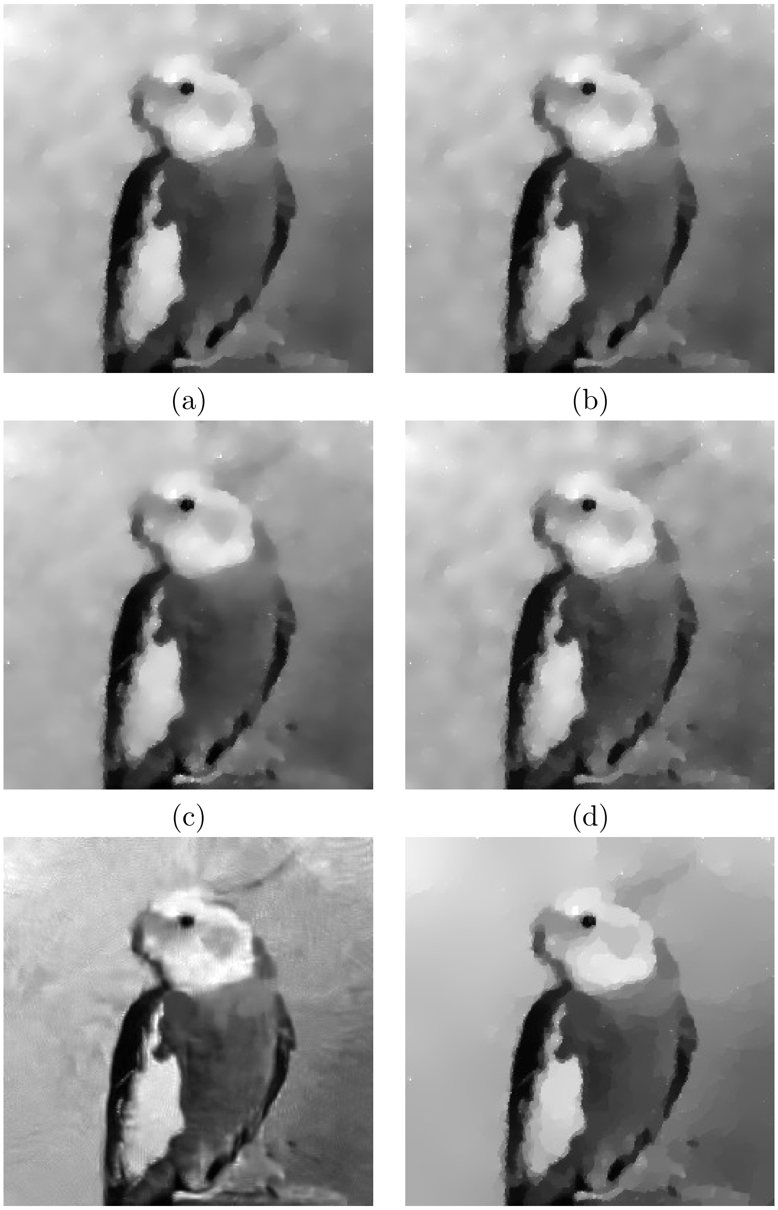

(a) (b)

(c) (d)

Figure 3.11: Denoising results of our model when $M = 3$ and comparisons with the exp [48], SO [65], TV-SARP [17], TwL-4V [35], SAR-BM3D [59] models. Denoised images with PSNR values: (a) exp (25.86) (b) SO (25.73) (c) TV-SARP (25.92) (d) TwL-4V (25.95) (e) SAR-BM3D (26.93) (f) our model (26.14)

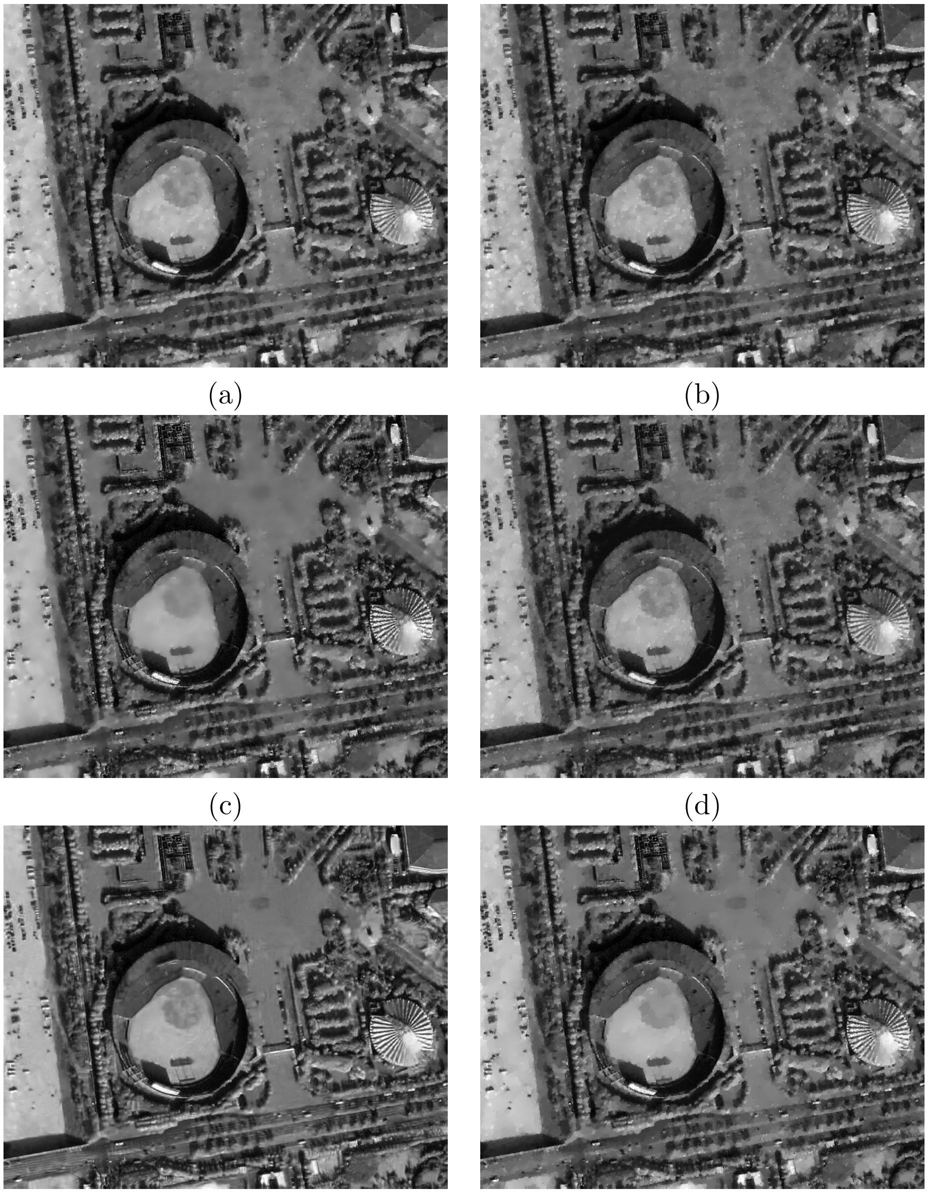

Figure 3.12: Denoising results of our model when $M = 5$ and comparisons with the exp [48], SO [65], TV-SARP [17], TwL-4V [35], SAR-BM3D [59] models. Denoised images with PSNR values: (a) exp (22.17) (b) SO (21.92) (c) TV-SARP (22.04) (d) TwL-4V (22.09) (e) SAR-BM3D (22.94) (f) our model (22.39)

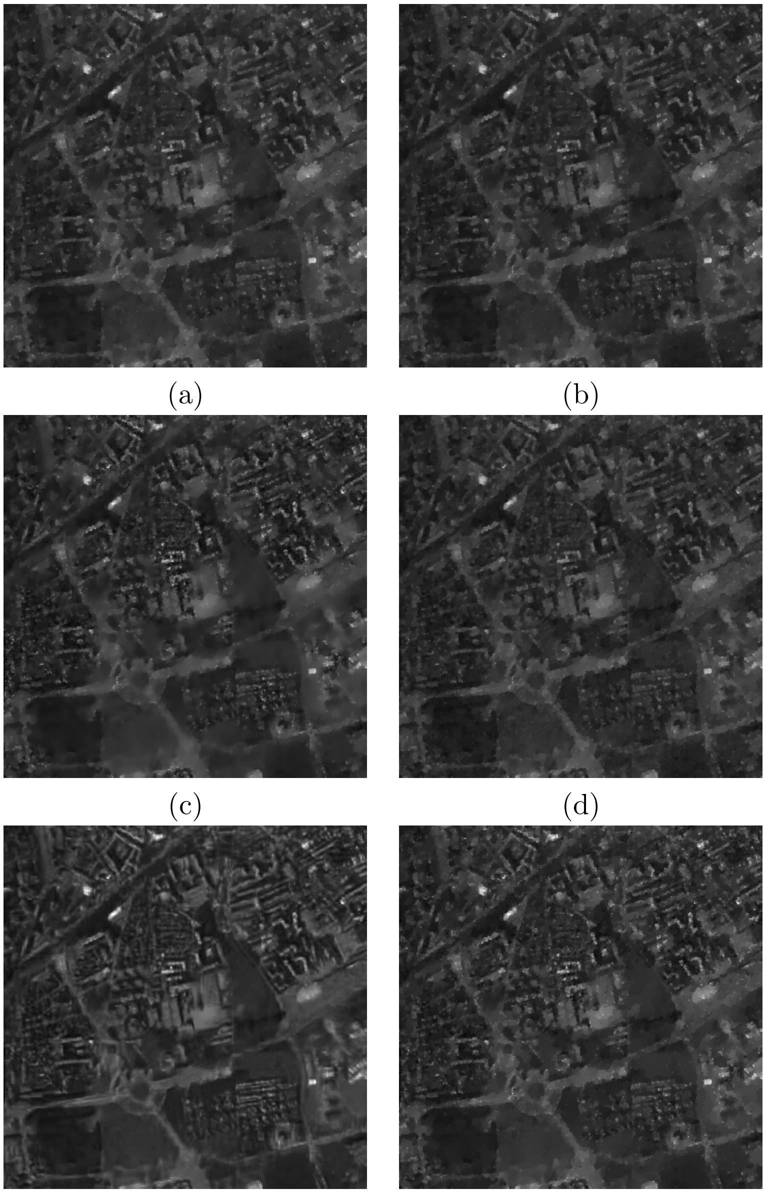
(a) (b)
(c) (d)

Figure 3.13: Denoising results of our model when $M = 3$ and comparisons with the exp [48], SO [65], TV-SARP [17], TwL-4V [35], SAR-BM3D [59] models. Denoised images with PSNR values: (a) exp (25.08) (b) SO (24.83) (c) TV-SARP (24.78) (d) TwL-4V (24.91) (e) SAR-BM3D (25.73) (f) our model (25.04)

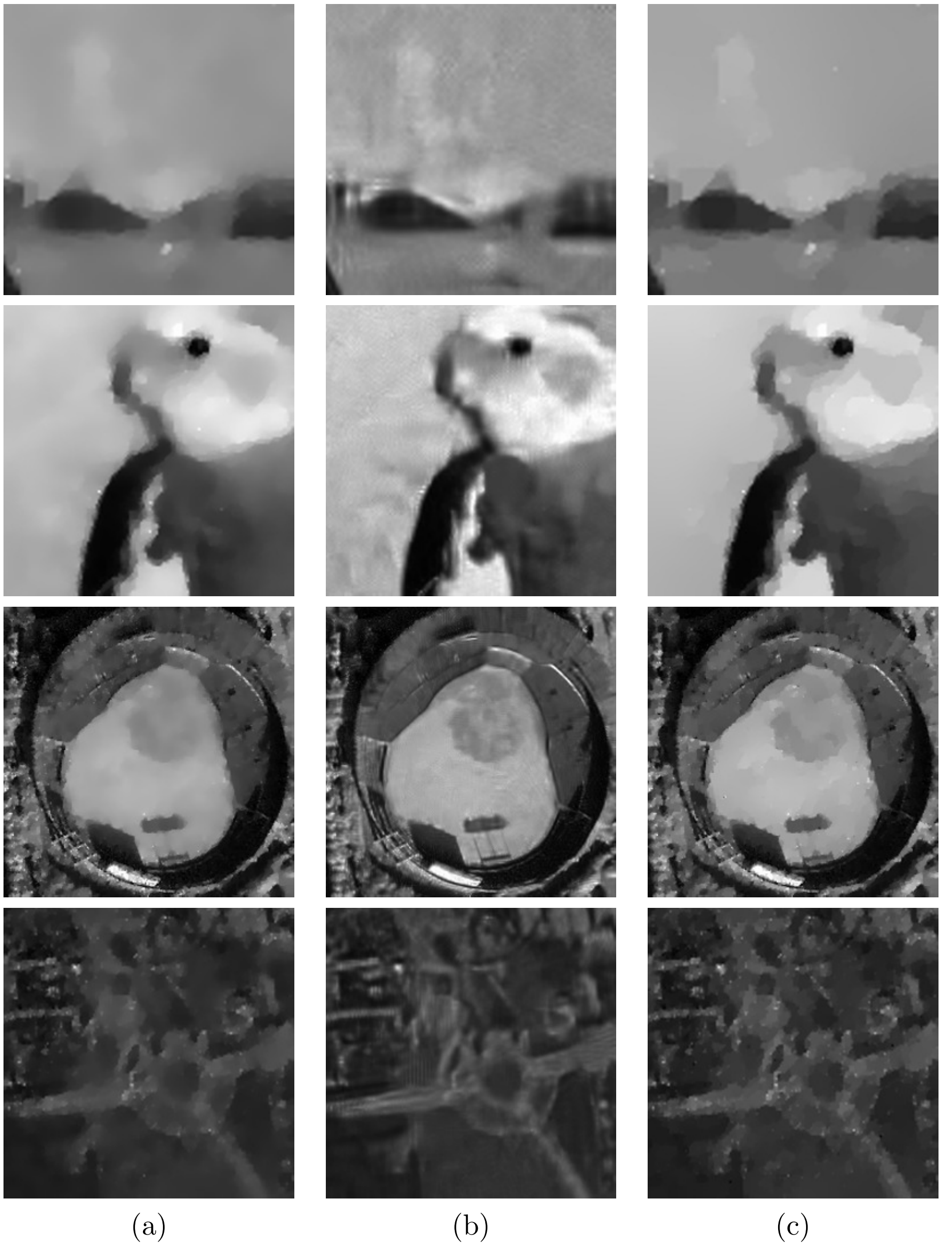

(a) (b) (c)

Figure 3.14: Zoomed denoised images in Figures 3.10, 3.11, 3.12, 3.13. Top row: zoom-in images of Figure 3.10, Second row: zoom-in images of Figure 3.11, Third row: zoom-in images of Figure 3.12, Bottom row: zoom-in image of Figure 3.13. (a) TV-SARP [17], (b) SAR-BM3D [59], (c) our model

Table 3.1: Comparisons of denoising results when $M = 10$ (PSNR/SSIM)

	exp model	SO model	TV-SARP	TwL-4V model	SAR-BM3D	Ours
Cameraman	25.77/0.79	25.39/0.77	26.11/0.80	25.73/0.78	26.98/0.80	26.45/0.81
Parrot	25.70/0.80	25.48/0.79	25.44/0.79	25.57/0.79	26.66/0.82	26.09/0.81
Bird	29.51/0.88	28.98/0.87	29.45/0.89	29.20/0.88	30.45/0.86	29.55/0.89
Castle	25.35/0.76	24.97/0.75	25.39/0.78	25.00/0.76	26.75/0.80	25.70/0.78
Clock tower	23.26/0.76	23.07/0.75	23.52/0.80	23.06/0.75	24.68/0.84	23.71/0.82
Rectangle	31.34/0.91	30.82/0.90	30.72/0.90	30.86/0.91	32.37/0.93	31.39/0.92
Zebra	23.24/0.67	23.07/0.68	23.39/0.69	23.01/0.67	24.92/0.73	23.69/0.70
Butterfly	25.93/0.85	25.50/0.84	25.62/0.86	25.85/0.85	27.39/0.87	26.12/0.86
House	27.89/0.78	27.48/0.77	27.79/0.79	27.51/0.78	29.91/0.81	28.08/0.80
Remote1	23.51/0.67	23.34/0.67	23.50/0.68	23.52/0.68	24.16/0.73	23.80/0.69
Remote2	21.44/0.71	21.48/0.71	21.61/0.73	21.31/0.70	21.69/0.75	21.93/0.74
Remote3	25.39/0.79	25.13/0.78	25.09/0.78	25.22/0.77	25.40/0.81	25.46/0.80
Remote4	24.85/0.75	24.71/0.75	24.75/0.77	24.81/0.75	25.66/0.81	25.14/0.78
Remote5	23.04/0.74	22.81/0.74	22.84/0.74	23.01/0.74	23.56/0.78	23.16/0.75
Remote6	20.03/0.79	19.61/0.78	19.52/0.77	19.96/0.78	19.84/0.80	20.09/0.80
Remote7	27.77/0.78	27.57/0.78	27.55/0.78	27.61/0.78	28.38/0.83	27.78/0.79

Table 3.2: Comparisons of denoising results when $M = 5$ (PSNR/SSIM)

	exp model	SO model	TV-SARP	TwL-4V model	SAR-BM3D	Ours
Cameraman	24.15/0.74	23.83/0.74	24.59/0.77	24.31/0.75	25.74/0.75	24.83/0.78
Parrot	24.38/0.76	23.95/0.75	23.95/0.76	24.10/0.76	25.32/0.78	24.58/0.77
Bird	27.63/0.85	27.52/0.85	27.98/0.86	27.83/0.85	28.71/0.81	28.20/0.86
Castle	23.82/0.71	23.63/0.70	24.01/0.73	23.78/0.70	25.14/0.75	24.21/0.74
Clock tower	21.73/0.69	21.41/0.68	21.83/0.74	21.49/0.68	23.16/0.77	22.10/0.75
Rectangle	29.23/0.88	28.86/0.87	28.71/0.87	28.81/0.88	30.33/0.89	29.39/0.89
Zebra	21.46/0.61	21.28/0.60	21.72/0.64	21.25/0.59	23.52/0.68	21.90/0.63
Butterfly	25.93/0.85	25.50/0.84	25.62/0.86	25.85/0.85	27.39/0.87	26.12/0.86
House	25.80/0.74	25.59/0.73	25.66/0.74	25.90/0.74	27.73/0.75	25.91/0.75
Remote1	22.17/0.60	21.92/0.60	22.04/0.62	22.09/0.61	22.94/0.66	22.39/0.63
Remote2	19.58/0.59	19.62/0.60	19.82/0.64	19.51/0.59	20.20/0.65	20.03/0.65
Remote3	23.78/0.71	23.42/0.69	23.49/0.70	23.51/0.68	24.05/0.72	23.74/0.72
Remote4	23.32/0.66	23.16/0.67	23.20/0.68	23.34/0.67	24.23/0.73	23.54/0.69
Remote5	21.69/0.66	21.38/0.65	21.36/0.66	21.52/0.66	22.12/0.70	21.70/0.67
Remote6	18.35/0.70	17.85/0.68	17.78/0.67	18.14/0.69	18.52/0.72	18.27/0.71
Remote7	26.19/0.70	25.95/0.70	25.96/0.70	26.07/0.70	26.88/0.76	26.15/0.72

Table 3.3: Comparisons of denoising results when $M = 3$ (PSNR/SSIM)

	exp model	SO model	TV-SARP	TwL-4V model	SAR-BM3D	Ours
Cameraman	23.17/0.72	22.93/0.72	23.51/0.75	23.28/0.73	24.93/0.72	23.57/0.75
Parrot	23.01/0.73	22.52/0.72	22.70/0.73	22.60/0.72	24.39/0.74	23.23/0.73
Bird	25.86/0.72	25.73/0.82	25.92/0.84	25.95/0.82	26.93/0.75	26.14/0.84
Castle	22.94/0.68	22.80/0.68	22.99/0.70	22.92/0.67	23.99/0.70	23.18/0.70
Clock tower	20.81/0.64	20.55/0.64	20.85/0.69	20.64/0.64	22.19/0.72	21.10/0.69
Rectangle	28.09/0.85	27.71/0.85	27.42/0.84	27.77/0.84	28.94/0.86	28.32/0.86
Zebra	20.25/0.55	20.24/0.55	20.59/0.59	20.17/0.54	22.40/0.62	20.62/0.57
Butterfly	22.62/0.76	22.10/0.75	22.15/0.78	22.33/0.76	24.73/0.79	22.82/0.78
House	24.84/0.71	24.62/0.71	24.67/0.73	24.78/0.72	26.47/0.71	25.07/0.74
Remote1	21.17/0.54	20.87/0.53	21.01/0.56	21.02/0.55	22.06/0.61	21.32/0.57
Remote2	18.59/0.50	18.56/0.52	18.72/0.56	18.57/0.52	19.20/0.58	18.93/0.58
Remote3	22.75/0.64	22.43/0.63	22.48/0.64	22.37/0.61	23.10/0.66	22.80/0.65
Remote4	22.36/0.60	22.03/0.58	22.13/0.61	22.23/0.60	23.15/0.67	22.48/0.62
Remote5	20.56/0.59	20.22/0.58	20.14/0.59	20.41/0.60	21.11/0.65	20.66/0.61
Remote6	17.16/0.61	16.57/0.56	16.56/0.56	16.80/0.58	17.60/0.65	17.05/0.62
Remote7	25.08/0.62	24.83/0.62	24.78/0.63	24.91/0.63	25.73/0.69	25.04/0.65

Table 3.4: Comparisons of computing time (sec) when $M = (10/5/3)$

	exp model [48]	SO model [65]	TV-SARP [17]	TwL-4V model [35]	SAR-BM3D [59]	Ours
Cameraman	2.7/5.5/6.1	0.4/0.4/0.5	3.8/5.1/6.1	0.04/0.12/0.06	20.2/20.2/20	3/3.5/3.4
Parrot	2.9/5.7/6.8	0.4/0.5/0.5	4.8/6.3/7.6	0.06/0.09/0.07	20.1/20.5/19.8	3.5/4.3/4
Bird	2.9/6/7.2	0.4/0.5/0.5	4.1/5.7/7.1	0.04/0.04/0.03	20.2/20.7/20.1	3.6/4/3.7
Castle	7.4/16.4/19.6	1.1/1.3/1.5	12.3/16.2/20.6	0.17/0.17/0.2	48.3/48.4/47.9	9.1/10.9/10.4
Clock tower	6.4/14.8/17.3	1/1.2/1.3	13/16.8/21	0.17/0.2/0.26	48.5/48.6/48.9	9.7/11.5/10.9
Rectangle	1.8/4.3/4.9	0.3/0.3/0.3	2.3/2.9/3.8	0.06/0.06/0.06	14.1/13.9/14	2/2.4/2
Zebra	6.5/14.6/17.5	1/1.2/1.3	12.5/15.2/19.1	0.14/0.18/0.2	49.4/48.7/49.1	8.4/9.8/10
Butterfly	3/6.5/7.6	0.5/0.5/0.6	5.4/7.1/9	0.06/0.07/0.07	22.6/22.6/22.7	3.3/3.7/3.5
House	2.6/5.5/6.5	0.4/0.5/0.5	4.2/5.7/7.1	0.06/0.03/0.04	20.2/20.2/20.3	3.2/3.8/3.7
Remote1	15.5/35/40.3	2.5/2.8/3.2	31.2/39.7/49	0.48/0.54/0.54	112.9/113.1/113.3	21/24.9/23.5
Remote2	14.1/37.7/46.6	2.3/2.8/3.4	35.9/47.4/60.5	0.65/0.6/0.74	134.2/134.6/135.7	19.4/25/25.2
Remote3	14/39.4/50.9	2.7/3.7/4	40.4/53.1/67.6	0.63/0.92/0.98	161.9/156.1/156.4	25.2/31.6/32.7
Remote4	11.3/27.5/32.7	1.9/2.1/2.4	22.1/29/35.7	0.39/0.54/0.49	91.6/91.7/91.7	13.2/16.7/16.3
Remote5	1.2/2.9/3.7	0.2/0.3/0.3	2.7/3.5/4.3	0.01/0.04/0.04	11.9/11.9/12	1.4/1.6/1.6
Remote6	1.7/4.1/4.9	0.3/0.4/0.4	4.8/6/7.5	0.09/0.04/0.06	20.1/20.1/20.2	2/2.3/2.5
Remote7	5.1/13.2/16.3	0.9/1.1/1.2	9/11.6/13.9	0.23/0.18/0.24	49.8/50/50.1	6.4/8.1/8.2

3.2 Proposed model 2 : exp NTGV model with SARP

In this section, we introduce a variational model using a NTGV and a SARP approach, and present an efficient optimization algorithm for solving our model. Specifically, in Section 3.2.1, we propose a NTGV-based model with the SARP to remove heavy multiplicative Gamma noise. In Section 3.2.2, we describe an updating strategy for the SARP by introducing a constrained model with local constraints. We present an iterative algorithm for solving the proposed model in Section 3.2.3.

3.2.1 Proposed NTGV model

First, we propose the following model for the removal of heavy multiplicative noise, which utilizes a NTGV and a SARP $\lambda : \Omega \to \mathbb{R}$:

$$\min_{u} \int_{\Omega} \lambda(x) \left[u + fe^{-u} + \alpha \left(\sqrt{\frac{e^u}{f}} - \beta \mathbf{1} \right)^2 \right] dx + \mathrm{NTGV}(u), \tag{3.2.1}$$

with the NTGV defined as

$$\mathrm{NTGV}(u) = \min_{\mathbf{p}} \int_{\Omega} \alpha_1 \phi_1(|\nabla u - \mathbf{p}|) + \alpha_0 \phi_0(|\mathcal{E}(\mathbf{p})|)\, dx, \tag{3.2.2}$$

where ϕ_i $(i = 1, 2)$ are the nonconvex log functions, $\phi_i(x) = \frac{1}{\rho_i} \log(1 + \rho_i x)$, where $\rho_i > 0$ control the nonconvexity of regularization terms. The parameters $\alpha > 0$ and $\beta \geqslant 1$ are defined in (2.1.15) and satisfy the condition in (2.1.16) to enforce the convexity of the data-fidelity term.

The data-fidelity term in (2.1.15) is employed for our model because it is suitable for heavy multiplicative Gamma noise. Thus, our model is an extension of the TV-based denoising models in (2.1.15) and (3.1.16) to higher-order regularization. Moreover, we utilize a nonconvex version of TGV, since TGV automatically balances the first- and second-order derivatives rather than using any fixed combination. The NTGV enables us to benefit from both higher-order regularization and nonconvex regularization for image denoising. That is, it helps sufficiently denoise smooth regions without staircasing effects while preserving edges and details. We further extend our model by incorporating the SARP approach. The SARP approach automatically selects a spatially varying regularization parameter, which prevents over-smoothing of small features such as textures while sufficiently denoising homogeneous regions.

Here we employ the nonconvex log function among some possible nonconvex functions in (2.1.3). In the case of the nonconvex ℓ_q-norm regularizer, it is difficult to find its limiting supergradient at zero. Moreover, as discussed in [49], one can expect to obtain better denoising results when using the fractional function to reconstruct piecewise-constant images. However, for images that are no longer piecewise constant, the log function produces better denoising results. In general, real natural or SAR images are not piecewise-constant, so we utilize the log function as our nonconvex function ϕ_i. This log type of NTGV was introduced in [53, 54], the only difference to our approach is that we use different values for the parameters ρ_1 and ρ_2.

3.2.2 Updating rule for $\lambda(x)$ in (3.2.1)

Now we describe an updating rule for the SARP $\lambda(x)$ in (3.2.1), following the SARP approaches given in [22, 51].

First, we present some statistical properties of a Gamma random variable. Let us assume that η follows the Gamma distribution with mean 1 and standard deviation $\frac{1}{\sqrt{M}}$, and consider the following function:

$$I(\eta) = \eta - \log \eta + \alpha \left(\sqrt{\frac{1}{\eta}} - \beta \right)^2, \tag{3.2.3}$$

where $\alpha, \beta \in \mathbb{R}$. As discussed in Lemma 3.1.1, the expectation of $I(\eta)$ is obtained as follows:

$$\begin{aligned} \mathbb{E}\{I(\eta)\} &= 1 + \frac{1}{2M} + \frac{1}{12M^2} - \frac{5}{2M^3} \\ &\quad + \alpha \left(\frac{M}{M-1} - \frac{2\beta\sqrt{M}\Gamma(M-\frac{1}{2})}{\Gamma(M)} + \beta^2 \right) + O(\frac{1}{M^3}), \end{aligned} \tag{3.2.4}$$

where the $O(s)$ is defined as $\lim_{s \to 0+} \dfrac{O(s)}{s} < \infty$.

From now on, we derive a constrained model with local constraints to obtain an updating strategy for the SARP $\lambda(x)$ in (3.2.1). First, we define a local window at center x with size r, $\Omega_x^r = \{y \mid \|x-y\|_\infty \leqslant \frac{r}{2}\}$, and a mean filter $w_r(x,y)$ as follows:

$$w_r(x,y) = \begin{cases} \frac{1}{|\Omega_x^r|}, & \text{if } \|y-x\|_\infty \leqslant \frac{r}{2}, \\ 0, & \text{otherwise}. \end{cases} \tag{3.2.5}$$

From the degradation model (1.0.1), we can obtain $\eta \approx \frac{f}{\tilde{u}}$, and then we substitute η in (3.2.3) with $\frac{f}{\tilde{u}}$. Hence, the local expected value estimator of $I(\frac{f}{\tilde{u}})$ at x, associated with the local window (3.2.5), is obtained as

$$\int_\Omega w_r(x,y)\left[\frac{f}{\tilde{u}} - \log\frac{f}{\tilde{u}} + \alpha\left(\sqrt{\frac{\tilde{u}}{f}} - \beta\right)^2\right] dy. \tag{3.2.6}$$

Then, by taking the transformation $u = \log\tilde{u}$ in (3.2.6), we can obtain the following local expected value estimation function $F_u^r(x)$:

$$F_u^r(x) = \int_\Omega w_r(x,y)\bar{g}(u)(y)\, dy, \tag{3.2.7}$$

where $\bar{g}(u) = u + fe^{-u} - \log f + \alpha\left(\sqrt{\frac{e^u}{f}} - \beta\right)^2$.

Now we consider the following NTGV based minimization problem with local constraints:

$$\min_u \ \mathrm{NTGV}(u) \quad \text{s.t.} \quad F_u^r(x) \leqslant C \quad \text{a.e. in } \Omega, \tag{3.2.8}$$

where C is an approximate expected value of $I(\eta)$, which is given by

$$C = 1 + \frac{1}{2M} + \frac{1}{12M^2} - \frac{5}{2M^3} + \alpha\left(\frac{M}{M-1} - \frac{2\beta\sqrt{M}\Gamma(M-\frac{1}{2})}{\Gamma(M)} + \beta^2\right). \tag{3.2.9}$$

The constrained model (3.2.8) involves only one local window. According to [51], a small local window results in leftover noise in homogeneous regions, whereas a large local window leads to over-smoothing of fine features such as edges and details. Thus, an appropriate selection of window size is important, so we here adopt multiple local windows to overcome this limitation. In [51], it was shown that the use of multiple local windows results in better denoising results in both homogeneous and edge regions than when using one local window, especially when considering heavy multiplicative noise.

Therefore, we ultimately consider the following constrained model with local constraints involving multiple local windows:

$$\min_u \mathrm{NTGV}(u) \quad \text{s.t.} \quad F_u(x) \leqslant C \quad \text{a.e. in } \Omega, \tag{3.2.10}$$

where $F_u(x)$ is the local expected value using multiple local windows, which can be computed as

$$\begin{aligned} F_u(x) &= \frac{1}{N}\sum_{k=1}^{N} F_u^{r_k}(x) = \frac{1}{N}\sum_{k=1}^{N}\int_\Omega w_{r_k}(x,y)\bar{g}(u)(y)\,dy \\ &= \int_\Omega w(x,y)\bar{g}(u)\,dy, \end{aligned} \tag{3.2.11}$$

with $w(x,y) = \frac{1}{N}\sum_{k=1}^{N} w_{r_k}(x,y)$ is the average of the mean filters defined in (3.2.5).

Finally, we relate the constrained model (3.2.10) with the proposed model (3.2.1). For this, we convert the constrained model (3.2.10) into the following unconstrained minimization problem using the penalty method:

$$\min_u \ \mathrm{NTGV}(u) + \frac{\mu}{2}\int_\Omega (\max(F_u(x) - C, 0))^2\,dx, \tag{3.2.12}$$

where $\mu > 0$ is a penalty parameter. As μ approaches ∞, the unconstrained problem (3.2.12) goes back to the original problem (3.2.10).

The Féchet derivative of $F_u(x)$, with its action ν, is computed as

$$F_u'(x)\nu = \int_\Omega w(x,y)(\bar{g}'(u)\nu)(y)\,dy. \tag{3.2.13}$$

Using this formula (3.2.13), the Féchet derivative of the penalty quadratic term in (3.2.12) is computed as follows:

$$\int_\Omega G_\mu(u)F_u'(x)\nu\,dx = \int_\Omega G_\mu(u)\left(\int_\Omega w(x,y)(\bar{g}'(u)\nu)(y)\,dy\right)dx, \tag{3.2.14}$$

where $G_\mu(u) = \mu\max(F_u(x) - C, 0)$. Thus, the first-order optimality condition of the problem (3.2.12) is given by

$$\mathbf{0} \in \partial(\mathrm{NTGV}(u)) + F_u'(x)^* G_\mu(u), \tag{3.2.15}$$

where $F_u'(x)^*$ is the adjoint operator of $F_u'(x)$. This condition (3.2.15) is only the necessary optimality condition due to the nonconvexity of the model (3.2.12).

Let u_μ be a critical point which holds the first-order optimality condition (3.2.15). Then, we can have the following equality for any action ν:

$$\int_\Omega F_{u_\mu}'(x)^* G_\mu(u_\mu)\nu\,dx = \int_\Omega [\bar{g}'(u_\mu)\nu](x)\lambda_\mu(x)\,dx, \tag{3.2.16}$$

where

$$\lambda_\mu^\circ = G_\mu(u_\mu), \quad \lambda_\mu = \int_\Omega w(x,y)\lambda_\mu^\circ \, dx. \tag{3.2.17}$$

On the other hand, the right-hand side of (3.2.16) is identical to the Féchet derivative of the data-fitting term in the proposed model (3.2.1) at $u = u_\mu$ when $\lambda_\mu = \lambda$. This implies that the problem (3.2.10) is identical to the problem (3.2.1) with a spatially varying function $\lambda : \Omega \to \mathbb{R}$ defined in (3.2.17).

Consequently, from this relation, we can obtain the updating rule (3.2.17) for the spatially varying parameter λ in (3.2.1).

3.2.3 Algorithm for solving the proposed model (3.2.1)

In this subsection, we present an algorithm to solving the proposed model (3.2.1). The function $\lambda : \Omega \to \mathbb{R}$ is automatically updated from the updating rule in (3.2.17). We initially select a small positive constant value for λ to obtain an over-smoothed restored image, and then restore details by updating the function λ. The updating rule for λ is as follows:

$$\begin{cases} \tilde{\lambda}^{n+1} &= \tilde{\lambda}^n + G_\delta(u^n), \\ \lambda^{n+1} &= \displaystyle\int_\Omega w(x,y)\tilde{\lambda}^{n+1} \, dx, \end{cases} \tag{3.2.18}$$

where $\delta > 0$ is a step size and u^n is the current estimation of the original image u. In other words, u^n is a solution of the problem (3.2.1) with respect to u for fixed $\lambda = \lambda^n(x)$:

$$u^n := \arg\min_u \int_\Omega \lambda^n(x) g(u) \, dx + \mathrm{NTGV}(u). \tag{3.2.19}$$

To sum up, our SARP algorithm for the model (3.2.1) is summarized in Algorithm 1.

Solving for the u-subproblem (3.2.20)

Here we focus on solving the u-subproblem (3.2.20) for fixed λ^n, which is a nonconvex problem. We first adopt the IRLA, which is introduced in [53] for solving a nonconvex minimization problem with linear constraints. Let us consider the following nonconvex linearly constrained minimization problem:

$$\min_{\mathbf{v}} \; S_1(\mathbf{v}) + S_2(|\mathbf{v}|) \quad \text{s.t.} \quad A\mathbf{v} = \mathbf{s}, \tag{3.2.21}$$

Algorithm 3 Proposed SARP algorithm for model (3.2.1)

```
Parameter : $\alpha_0, \alpha_1, \rho_0, \rho_1, \alpha,\ \beta,\ \delta$; the size $r_h$ of local windows ($h = 1, 2, \ldots, N$).
Initialization : $n = 0$, $\bar{\lambda}^n = \lambda^n = \lambda^0$ with a small constant value.
while a stopping condition is satisfied do
    Solve the discrete version of the problem
        $$u^n := \arg\min_u \left\{ \int_\Omega \lambda^n \left[ u + f e^{-u} + \alpha \left( \sqrt{\frac{e^u}{f}} - \beta \right)^2 \right] dx + \mathrm{NTGV}(u) \right\}. \tag{3.2.20}$$
    Based on $u^n$, update $\lambda^n$ as follows:
        Calculate $F^{r_h}_{u^k}(x)$ for all $h \in \{1, 2, \ldots, N\}$,
        $\bar{\lambda}^{n+1} = \bar{\lambda}^n + \delta \max\left( \frac{1}{N} \sum_{h=1}^{N} F^{r_h}_{u^n}(x) - C, 0 \right)$,
        $(\lambda^{n+1})_{i_x,i_y} = \frac{1}{N} \sum_{h=1}^{N} \left( \frac{1}{r_h^2} \sum_{(s,t)\in\Omega^{r_i}_{i_x,i_y}} (\bar{\lambda}^{n+1})_{s,t} \right)$.
end while
Final output : $\tilde{u} = e^u$
```

where $A \in \mathbb{R}^{m\times n}$, $\boldsymbol{s} \in \mathbb{R}^m$, $S_1 : \mathbb{R}^n \to \mathbb{R} \cup \{\infty\}$ is proper and convex, and $S_2 : \mathbb{R}^n_+ \to \mathbb{R}$ is concave and increasing. Here, $\mathbb{R}^n_+$ denotes the non-negative orthant of $\mathbb{R}^n$, and $|\mathbf{v}|$ is the coordinate-wise absolute value function. The IRLA for solving the problem (3.2.21) iteratively solves the following convex relaxation problem of (3.2.21):

$$\begin{cases} \mathbf{d}^k & \in & \bar{\partial} S_2(|\mathbf{v}_k|). \\ \mathbf{v}_{k+1} & = & \arg\min\limits_{A\mathbf{v}=\mathbf{s}} \; S_1(\mathbf{v}) + \langle \mathbf{d}^k, |\mathbf{v}| \rangle, \end{cases} \tag{3.2.22}$$

where $\bar{\partial} S_2 := -\partial(-S_2)$ denotes the superdifferential of the concave function S_2.

To apply IRLA, we first reformulate the problem (3.2.20) to the following equivalent constrained problem, using the variable splitting technique:

$$\begin{aligned} \min_{u,\mathbf{p},\mathbf{a},\mathbf{b},c} & \int_\Omega \lambda^n(x) g(c(x))\,dx + \int_\Omega \alpha_1\phi_1(|\mathbf{a}|) + \alpha_0\phi_0(|\mathbf{b}|), \quad (3.2.23) \\ \text{s.t. } & \mathbf{a} = \nabla u - \mathbf{p}, \quad \mathbf{b} = \mathcal{E}(\mathbf{p}), \quad c = u. \end{aligned}$$

This constrained problem (3.2.23) can be rewritten in the form (3.2.21) with the following setting:

$$\mathbf{v} = (u, \mathbf{p}, \mathbf{a}, \mathbf{b}, c)^T, \quad \mathbf{s} = \mathbf{0}, \quad A = \begin{pmatrix} \nabla & -I_{\mathbf{p}} & -I_{\mathbf{a}} & \mathbf{0} & \mathbf{0} \\ \mathbf{0} & \mathcal{E} & \mathbf{0} & -I_{\mathbf{b}} & \mathbf{0} \\ I_u & \mathbf{0} & \mathbf{0} & \mathbf{0} & -I_c \end{pmatrix},$$

$$S_1(\mathbf{v}) = \int_\Omega \lambda(x)^n g(c(x))\,dx \quad \text{and} \quad S_2(|\mathbf{v}|) = \int_\Omega \alpha_1\phi_1(|\mathbf{a}|) + \alpha_0\phi_0(|\mathbf{b}|)\,dx.$$

Now we can apply the IRLA to the constrained model (3.2.23). The first step of the IRLA applied to the model (3.2.23) is given by

$$\mathbf{d}^k = \left(0, \mathbf{0}, \frac{\alpha_1}{1+\rho_1|\mathbf{a}^k|}, \frac{\alpha_0}{1+\rho_0|\mathbf{b}^k|}, 0\right)^T \in \bar{\partial} S_2(|\mathbf{v}^k|). \tag{3.2.24}$$

Since the functional S_2 is differentiable, its limiting supergradient corresponds to its gradient. Moreover, the second step of the IRLA applied to the model (3.2.23) is obtained as follows:

$$\begin{aligned} & (\mathbf{a}^{k+1}, \mathbf{b}^{k+1}, c^{k+1}, u^{k+1}, \mathbf{p}^{k+1})^T = \quad (3.2.25) \\ & \qquad \arg\min_{A\mathbf{v}=\mathbf{0}} \left\{ \langle \lambda^n g(c), 1 \rangle + \langle \mathbf{d}_1^k, |\mathbf{a}| \rangle + \langle \mathbf{d}_0^k, |\mathbf{b}| \rangle \right\}, \end{aligned}$$

where $\langle\cdot,\cdot\rangle$ is the componentwise inner product, $\mathbf{d}_1^k = \frac{\alpha_1}{\rho_1|\mathbf{a}^k|+1}$ and $\mathbf{d}_0^k = \frac{\alpha_0}{\rho_0|\mathbf{b}^k|+1}$.

The problem in (3.2.25) is a convex minimization problem with linear equality constraints. However, the minimization of (3.2.25) is not easy, due to the nonsmooth terms and the constraints. To handle these difficulties, we employ the ADMM. In the following section, we depict an algorithm for solving the problem (3.2.25).

ADMM for solving the problem (3.2.25)

The ADMM [8, 70] is a widely used algorithm to solve linearly constrained convex optimization problems. We consider the following convex minimization problem with linear constraints:

$$\min_{y,v} \theta_1(y) + \theta_2(v) \quad \text{s.t.} \quad Cy + Dv = e, \tag{3.2.26}$$

where θ_1 and θ_2 are convex, proper, and lower semi-continuous functions. The augmented Lagrangian function for the problem (3.2.26) is defined as

$$\mathcal{L}_\tau(y, v; z) = \theta_1(y) + \theta_2(v) + z^T(Cy + Dv - e) + \frac{\tau}{2}\|Cy + Dv - e\|_2^2, \tag{3.2.27}$$

where z is the Lagrangian multiplier vector and $\tau > 0$ is a penalty parameter. The ADMM for solving the problem (3.2.26) minimizes the augmented Lagrangian function (3.2.27) over each variable, y or v, with the other variable fixed, and then updates the Lagrange multiplier z induced by the Karush–Kuhn–Tucker optimality conditions for (3.2.26), which are given by

$$\begin{cases} y^{i+1} &= \arg\min_y \mathcal{L}_\tau(y, v, z^i), \\ v^{i+1} &= \arg\min_v \mathcal{L}_\tau(y^{i+1}, v, z^i), \\ z^{i+1} &= z^i + \tau(Cy^{i+1} + Dv^{i+1} - e). \end{cases} \tag{3.2.28}$$

In the model (3.2.25), we let $\mathbf{v} = (y, v)$ with $y = (\mathbf{a}, \mathbf{b}, c)$ and $v = (u, \mathbf{p})$. Then the constraint in (3.2.25), i.e. $A\mathbf{v} = \mathbf{0}$, can have the form of $Cy + Dv = e$. Hence, the augmented Lagrangian function for the problem (3.2.25) is as follows:

$$\begin{aligned}\mathcal{L}_\tau(\mathbf{a},\mathbf{b},c,u,\mathbf{p};\gamma_{\mathbf{a}},\gamma_{\mathbf{b}},\gamma_c) &= \langle\lambda(x)g(c),1\rangle+\langle\mathbf{d}_1^k,|\mathbf{a}|\rangle+\langle\mathbf{d}_0^k,|\mathbf{b}|\rangle\\ &\quad+\langle\gamma_{\mathbf{a}},\mathbf{a}-\nabla u+\mathbf{p}\rangle+\frac{\tau}{2}\|\mathbf{a}-\nabla u+\mathbf{p}\|_2^2\\ &\quad+\langle\gamma_{\mathbf{b}},\mathbf{b}-\mathcal{E}(\mathbf{p})\rangle+\frac{\tau}{2}\|\mathbf{b}-\mathcal{E}(\mathbf{p})\|_2^2\\ &\quad+\langle\gamma_c,c-u\rangle+\frac{\tau}{2}\|c-u\|_2^2. \qquad (3.2.29)\end{aligned}$$

Thus, the ADMM applied to the problem (3.2.25) yields

$$\left\{\begin{aligned}\begin{pmatrix}\mathbf{a}^{i+1}\\ \mathbf{b}^{i+1}\\ c^{i+1}\end{pmatrix} &:= \arg\min_{\mathbf{a},\mathbf{b},c}\Big\{\langle\lambda(x)g(c),1\rangle+\langle\mathbf{d}_1^k,|\mathbf{a}|\rangle+\langle\mathbf{d}_0^k,|\mathbf{b}|\rangle+\langle\gamma_{\mathbf{a}}^i,\mathbf{a}\rangle\\ &\qquad+\frac{\tau}{2}\|\mathbf{a}-\nabla u^i+\mathbf{p}^i\|_2^2+\langle\gamma_{\mathbf{b}}^i,\mathbf{b}\rangle\\ &\qquad+\frac{\tau}{2}\|\mathbf{b}-\mathcal{E}(\mathbf{p}^i)\|_2^2+\langle\gamma_c^i,c\rangle+\frac{\tau}{2}\|c-u^i\|_2^2\Big\},\\ \begin{pmatrix}u^{i+1}\\ \mathbf{p}^{i+1}\end{pmatrix} &:= \arg\min_{u,\mathbf{p}}\Big\{\langle\gamma_{\mathbf{a}}^i,-\nabla u+\mathbf{p}\rangle+\frac{\tau}{2}\|\mathbf{a}^{i+1}-\nabla u+\mathbf{p}\|_2^2\\ &\qquad+\langle\gamma_{\mathbf{b}}^i,-\mathcal{E}(\mathbf{p})\rangle+\frac{\tau}{2}\|\mathbf{b}^{i+1}-\mathcal{E}(\mathbf{p})\|_2^2+\langle\gamma_c^i,-u\rangle\\ &\qquad+\frac{\tau}{2}\|c^{i+1}-u\|_2^2\Big\},\\ \begin{pmatrix}\gamma_{\mathbf{a}}^{i+1}\\ \gamma_{\mathbf{b}}^{i+1}\\ \gamma_c^{i+1}\end{pmatrix} &:= \begin{pmatrix}\gamma_{\mathbf{a}}^{i}\\ \gamma_{\mathbf{b}}^{i}\\ \gamma_c^{i}\end{pmatrix}-\tau\begin{pmatrix}\mathbf{a}^{i+1}-\nabla u^{i+1}+\mathbf{p}^{i+1}\\ \mathbf{b}^{i+1}-\mathcal{E}(\mathbf{p}^{i+1}))\\ c^{i+1}-u^{i+1}\end{pmatrix}.\end{aligned}\right.$$

The first subproblem in (3.2.30) is decoupled over the variables **a**, **b**, and c. Thus, it can be separated into the following three subproblems:

$$\begin{aligned}\mathbf{a}^{i+1} &= \arg\min_{\mathbf{a}}\Big\{\langle\mathbf{d}_1^k,|\mathbf{a}|\rangle+\langle\gamma_{\mathbf{a}}^i,\mathbf{a}\rangle+\frac{\tau}{2}\|\mathbf{a}-\nabla u^i+\mathbf{p}^i\|_2^2\Big\}, \qquad (3.2.30)\\ \mathbf{b}^{i+1} &= \arg\min_{\mathbf{b}}\Big\{\langle\mathbf{d}_0^k,|\mathbf{b}|\rangle+\langle\gamma_{\mathbf{b}}^i,\mathbf{b}\rangle+\frac{\tau}{2}\|\mathbf{b}-\mathcal{E}(\mathbf{p}^i)\|_2^2\Big\}, \qquad (3.2.31)\\ c^{i+1} &= \arg\min_{c}\Big\{\langle\lambda(x)g(c),1\rangle+\langle\gamma_c^i,c\rangle+\frac{\tau}{2}\|c-u^i\|_2^2\Big\}. \qquad (3.2.32)\end{aligned}$$

The subproblems for $\mathbf{a}^{i+1}$ and $\mathbf{b}^{i+1}$ in (3.2.30) can be solved exactly using the shrink operator:

$$\mathbf{a}^{i+1} = \text{shrink}\left(\nabla u^i - \mathbf{p}^i - \frac{\gamma_{\mathbf{a}}^i}{\tau}, \frac{\mathbf{d}_1^k}{\tau}\right), \tag{3.2.33}$$

$$\mathbf{b}^{i+1} = \text{shrink}\left(\mathcal{E}(\mathbf{p}^i) - \frac{\gamma_{\mathbf{b}}^i}{\tau}, \frac{\mathbf{d}_0^k}{\tau}\right), \tag{3.2.34}$$

where $\text{shrink}(a,b) = \frac{a}{\|a\|_2}\max(\|a\|_2 - b, 0)$. On the other hand, there is no closed-form solution for c^{i+1}. Since the objective function in the c-subproblem is differentiable, the Euler–Lagrange equation for c^{i+1} can be obtained as

$$Q(c) = \lambda(x)\left(1 - fe^{-c} + \alpha\left(\frac{e^c}{f} - \beta\sqrt{\frac{e^c}{f}}\right)\right) + \gamma_c^i + \tau(c - u^i) = 0. \tag{3.2.35}$$

The normal equation (3.2.35) can be efficiently solved by using Newton's method.

The minimizer $(u^{i+1}, \mathbf{p}^{i+1})$ of the second subproblem in (3.2.30) satisfy the following first-order optimality condition:

$$\left\{\begin{array}{rcl} -\tau \triangle u + \tau u + \tau \text{div}\mathbf{p} & = & -\text{div}\gamma_{\mathbf{a}}^i - \tau \text{div}\mathbf{a}^{i+1} + \gamma_c^i + \tau c^{i+1}, \\ \tau \nabla u - \tau \mathbf{p} + \tau \text{div}^2 \mathcal{E}(\mathbf{p}) & = & \gamma_{\mathbf{a}}^i + \tau \mathbf{a}^{i+1} + \text{div}^2 \gamma_{\mathbf{b}}^i + \tau \text{div}^2 \mathbf{b}^{i+1}, \end{array}\right. \tag{3.2.36}$$

where $\text{div}^2 W = \begin{pmatrix} \partial_x \omega_{11} + \partial_y \omega_{12} \\ \partial_x \omega_{21} + \partial_y \omega_{22} \end{pmatrix}$ for $W = \begin{pmatrix} \omega_{11} & \omega_{12} \\ \omega_{21} & \omega_{22} \end{pmatrix}$, which is the adjoint operator of $-\mathcal{E}$.

The formula (3.2.36) can be rewritten as the following linear equation:

$$B\begin{pmatrix} u \\ \mathbf{p}_1 \\ \mathbf{p}_2 \end{pmatrix} = \begin{pmatrix} -\text{div}\gamma_{\mathbf{a}}^i - \tau \text{div}\mathbf{a}^{i+1} + \gamma_c^i + \tau c^{i+1} \\ B_{1,i} \\ B_{2,i} \end{pmatrix}, \tag{3.2.37}$$

where $\mathbf{p} = (\mathbf{p}_1, \mathbf{p}_2)^T$, B is defined as

$$B = \begin{pmatrix} \tau(D_1^T D_1 + D_2^T D_2 + 1) & -\tau D_1^T & -\tau D_2^T \\ \tau D_1 & -\tau(1 + D_1^T D_1 + \frac{1}{2} D_2^T D_2) & -\frac{\tau}{2} D_2^T D_1 \\ \tau D_2 & -\frac{\tau}{2} D_1^T D_2 & -\tau(1 + \frac{1}{2} D_1^T D_1 + D_2^T D_2) \end{pmatrix}, \tag{3.2.38}$$

and $(B_{1,i},\, B_{2,i})^T = \gamma_{\mathbf{a}}^i + \tau \mathbf{a}^{i+1} + \text{div}^2 \gamma_{\mathbf{b}}^i + \tau \text{div}^2 \mathbf{b}^{i+1}$. Following the ideas in [32, 27], we can obtain $u^{i+1}, \mathbf{p}^{i+1}$ by two-dimensional fast Fourier transform (FFT) under a symmetric boundary condition.

To sum up, we describe the algorithm for solving the u-subproblem (3.2.20) in Algorithm 4.

Algorithm 4 Solve the u-subproblem (3.2.20)

```
Parameter : $\alpha_0, \alpha_1, \rho_0, \rho_1, \alpha, \beta, \tau > 0$; and $u^0 = f$
for $k = 0, 1, 2, \ldots$ do
    $\mathbf{d}_1^k = \frac{\alpha_1}{1+\rho_1|\mathbf{a}^k|}, \quad \mathbf{d}_0^k = \frac{\alpha_0}{1+\rho_2|\mathbf{b}^k|}$
    for $i = 0, 1, 2, \ldots, M_1 - 1$ do
        Initialize : $\gamma_{\mathbf{a}}^0 = \gamma_{\mathbf{b}}^0 = \gamma_c^0 = \mathbf{0}$
        $\mathbf{a}^{k,i+1} = \text{shrink}\left(\nabla u_i - \mathbf{p}_i - \frac{\gamma_i^{\mathbf{a}}}{\tau}, \frac{\mathbf{d}_1^k}{\tau}\right),$
        $\mathbf{b}^{k,i+1} = \text{shrink}\left(\mathcal{E}(\mathbf{p}_i) - \frac{\gamma_i^{\mathbf{b}}}{\tau}, \frac{\mathbf{d}_0^k}{\tau}\right)$
        $z^{k,i+1}$ is obtained by Newton's method.
        $\begin{pmatrix} u^{k,i+1} \\ \mathbf{p}_1^{k,i+1} \\ \mathbf{p}_2^{k,i+1} \end{pmatrix} = B^{-1} \begin{pmatrix} \{-\text{div}\gamma_{\mathbf{a}}^k - \tau\text{div}\mathbf{a}^{k+1} + \gamma_c^k + \tau c^{k+1}\}_i \\ B_{1,i} \\ B_{2,i} \end{pmatrix}$
        $\gamma_{\mathbf{a}}^{i+1} = \gamma_{\mathbf{a}}^i + \tau(\mathbf{a}^{k,i+1} - \nabla u^{k,i+1} + \mathbf{p}^{k,i+1})$
        $\gamma_{\mathbf{b}}^{i+1} = \gamma_{\mathbf{b}}^i + \tau(\mathbf{b}^{k,i+1} - \mathcal{E}(\mathbf{p}^{k,i+1}))$
        $\gamma_c^{i+1} = \gamma_c^i + \tau(c^{k,i+1} - u^{k,i+1})$
    end for
    Return $\mathbf{a}^{k+1} = \mathbf{a}^{k,M_1}, \ \mathbf{b}^{k+1} = \mathbf{b}^{k,M_1}, \ c^{k+1} = c^{k,M_1},$
           $u^{k+1} = u^{k,M_1}, \ \mathbf{p}^{k+1} = \mathbf{p}^{k,M_1}.$
end for
```

3.2.4 Numerical results

In this section, we compare the performance of our model with other state-of-art models which were recently proposed for multiplicative noise removal. Specifically, we compare our proposed model with the exp-SARP model [51], the TwL-mV model [35], the SO-TGV model [25], and the DZ-TGV model [64].

We tested 10 images, as shown in Figure 3.15, which consist of six natural images and four SAR images. For experiments, all test images are corrupted by multiplicative Gamma noise for $M = 3$, 5, or 10.

To measure the quality of restored images, we use the peak-signal-to-noise-ratio (PSNR) value and structure similarity (SSIM) index [68]. The PSNR is given by

$$\mathrm{PSNR}(u, u_*) = 10 \log_{10} \left(\frac{255^2 N_p}{\|u - u_*\|_2^2} \right),$$

where N_p is the total number of pixels, u and u_* present the restored image and clean image, respectively.

All methods are terminated when the following stopping condition is satisfied:

$$\frac{\|\tilde{u}^{l+1} - \tilde{u}^l\|_2}{\|\tilde{u}^l\|_2} < tol \quad \text{or} \quad l > MaxIter \tag{3.2.39}$$

where $\tilde{u}^l$ is the restored image at iteration l; $\tilde{u} = e^u$ for our model, the exp-SARP model, and SO-TGV model, $\tilde{u} = u^m$ for the TwL-mV model and $\tilde{u} = u$ for the DZ-TGV model. We use the tolerance value $tol = 10^{-4}$ for our model and the exp-SARP model when we solve the u-subproblem. In particular, we set $M_1 = 50$ in Algorithm 2 and use the tolerance value in the ADMM process. For other iterations of our model and the exp-SARP model, we only use the maximum iteration which is fixed by $MaxIter = 3$ which is the smallest iteration number to get satisfactory updated λ. As can be seen in Figure 3.17, the more iteration, the texture region has higher λ value while homogeneous region has still low λ value. This shows that λ is updated appropriately. Moreover, Figure 3.17-(b) and (c) do not make a big difference. Thus more iteration is not meaningful. The tolerance value of the SO-TGV model and DZ-TGV model is set as $tol = 3 \times 10^{-5}$ and 4×10^{-4}, respectively, as provided in [25, 64].

We use the proximal linearized ADMM (PLAD) algorithm [69] to solve the exp-SARP model. For the SO-TGV and the DZ-TGV models, the primal dual algorithm [14] is utilized.

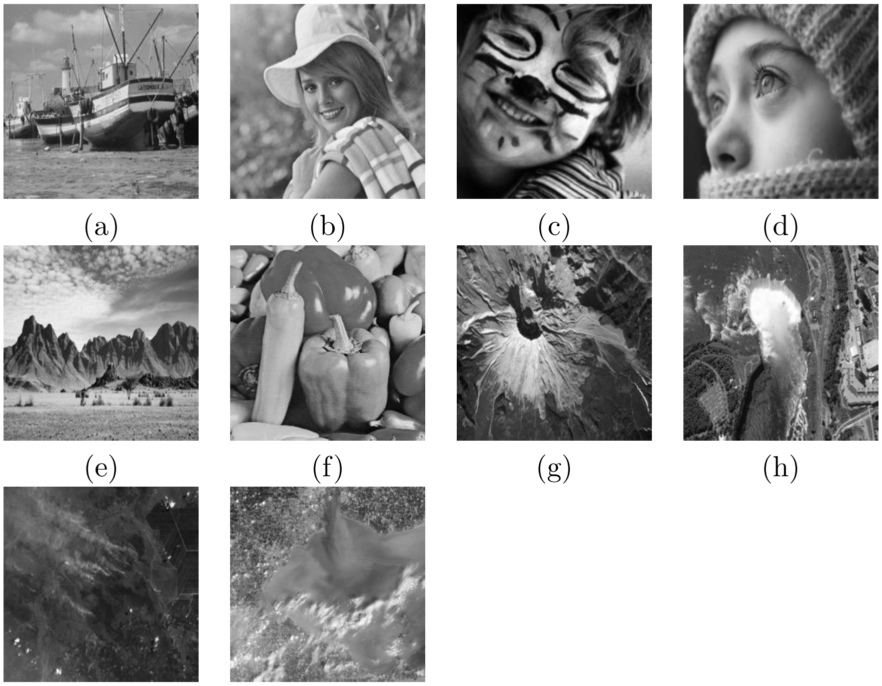

(a) (b) (c) (d)

(e) (f) (g) (h)

(i) (j)

Figure 3.15: Original images. First row: Boat (256 × 256), Elaine (256 × 256), Face (255 × 255), Girl (336 × 254), and Mountain (400 × 200). Second row: Peppers (256 × 256), Remote1 (350 × 228), Remote2 (350 × 253), Remote3 (308 × 236), and Remote4 (275 × 275).

All numerical experiments are performed in MATLAB R2015b running on a 64-bit Windows 7 PC with an Intel i7-3770 CPU @ 3.40 GHz and 16 GB RAM.

3.2.5 Selection of parameters

In the primal dual algorithm [14] used to solve the SO-TGV and DZ-TGV models, the primal and dual proximal parameters σ, τ are directly related to the speed of convergence. We set $\sigma = \tau = \frac{1}{\sqrt{12}}$ for the SO-TGV model and $\sigma = 0.0016,\ \tau = 50$ for the DZ-TGV model, as described in [25, 64], respectively. The parameter α in the DZ-TGV model has to be manually tuned to obtain satisfactory restored results. In particular, α should satisfy the condition $\alpha \geqslant \frac{2\sqrt{6}}{9}$ for the convexity of the data-fidelity term. Under heavy noise level such as $M = 3$ or 5, the restored images of the DZ-TGV

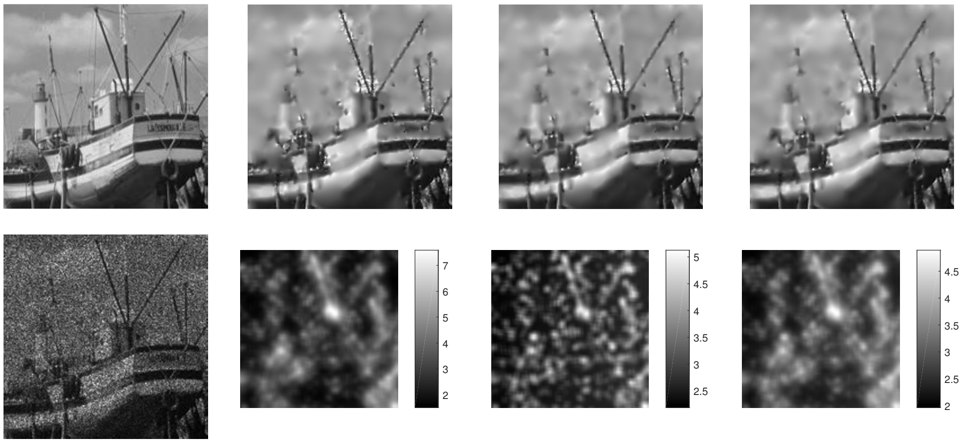

(a) (b) (c) (d)

Figure 3.16: Denoised images and final λ values of the Boat image with different number of windows and sizes. (a) Original and noisy images (b) $(r_1, r_2) = (7, 21)$ (PSNR : 25.31) (c) $(r_1, r_2) = (7, 256)$ (PSNR: 25.63) (d) $(r_1, r_2, r_3) = (7, 21, 256)$ (PSNR: 25.65)

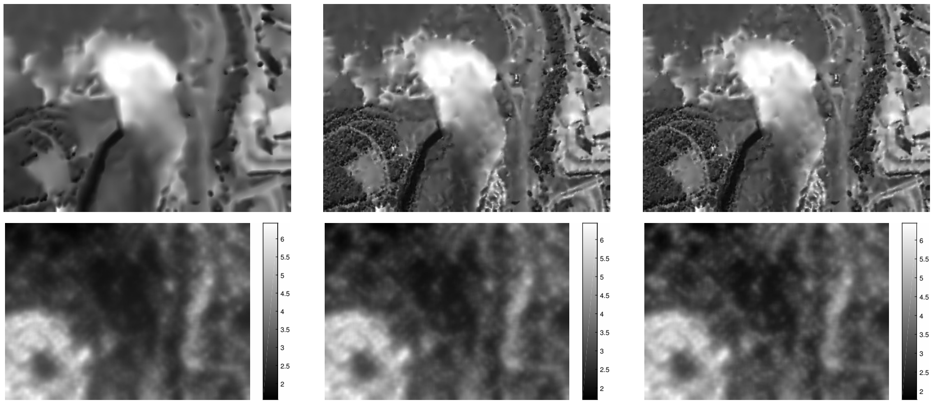

(a) (b) (c)

Figure 3.17: Denoising images and corresponding updated λ values of different iteration : (a) first iteration (PSNR : 22.68) (b) second iteration (PSNR : 24.79) (c) third iteration (PSNR : 24.82)

model get worse as α increases. For this reason, α was selected as $\frac{2\sqrt{6}}{9}$ for $M = 3$ and 5. We tune the regularization parameter λ in the SO-TGV and DZ-TGV models to obtain satisfactory denoising results.

We choose $m = 4$ for TwL-mV model [35], which gives satisfactory results with reasonable computational cost. To find a solution, LPAMA is utilized and we set same parameter as in [35].

For the exp-SARP model and our model, the value of β is closely related to the noise level M. As provided in [48], we take $\beta = \frac{1}{0.1113+0.1109M^2} + 1$. The value for α in the exp-SARP model and our model is heuristically set to satisfy the condition (2.1.16). In fact, we use the same values for α and β in the exp-SARP model and our model. Moreover, we fix a penalty parameter $\tau = 0.75$ in both ADMM and PLAD algorithms. In Figure 3.16, we present the restored images and final λ-value for $(r_1, r_2) = (7, 21)$, $(7, \text{size}(f))$ and $(r_1, r_2, r_3) = (7, 21, \text{size}(f))$. Figure 3.16-(b) presents the denoised image with two small local windows. It is observed that the difference of maximum and minimum values in the final λ is too big and it yields to produce too oversmoothed homogenous region and lots of noises in textural region. That is, λ has not been updated properly and it leads the lowest PSNR value. Figure 3.16-(c) is the denoised image obtained using one small and one large windows. Compared to (d), which uses the combination of small, medium and large windows, the denoising results do not differ significantly. However, the texture regions in Figure 3.16-(c) are slightly oversmoothed. Thus, we use the combination of three local windows that shows the most satisfactory result. Therefore, in our experiments, three local windows are utilized with size $r_1 = 7$, $r_2 = 21$, and $r_3 = \text{size}(f)$ for both models. For our model, the parameters ρ_1 and ρ_0 affect the quality of restored images, which are fixed as $\rho_1 = 0.01$ and $\rho_0 = 5$.

3.2.6 Image denoising

In Figures 3.18 and 3.19, we show the denoising results of our model when the noise level $M = 10$, and comparisons with other models. It can be seen that the TwL-mV model and the exp-SARP model produces restored images with staircasing artifacts around the faces of both images. Comparing our model with the SO-TGV model and the DZ-TGV model, we can observe that our model retains less noise around the cheek and preserves more details in the eyes and hat in Figure 3.18. Moreover, in Figure 3.19, we can observe that the restored image of our model has clear eyes, nose, and mouth and some noise in the hat is eliminated well, unlike the SO-TGV model and the DZ-TGV model. These images indicate that the SARP $\lambda(x)$ in our model performs properly, leading to better denoising results than a fixed constant λ.

In Figure 3.20 and 3.21, we test all the above-mentioned denoising models for all noise levels $M = 10, 5$, and 3. It is seen that recovered images of TV based models (TwL-4V model and exp-SARP model) have the staircasing artifacts in the homogeneous region for all noise levels. However, the exp-SARP model retains less noise in the background while preserving details than the TwL-4V model due to its SARP approach. In the case of $M = 10$, the DZ-TGV model provides a satisfactory result. However, when M is small ($M = 5$ and 3), it produces a restored image that is too over-smoothed. Thus, the restored images of the DZ-TGV model do not capture any details. Moreover, we can see some artifacts with black and white dots, which are caused by the quadratic term in the DZ-TGV model. From [23], the authors showed that the data-fidelity term of the DZ-TGV model is mainly suitable for a large value of M owing to statistical property of the Gamma distribution. In addition, we also confirm that the DZ-TGV model is not suitable when the noise level M is smaller than 10. If we increase the λ value for the DZ-TGV model, then we obtain a reconstructed image with a lot of black and white dots while avoiding over-smoothing and conserving detail. Thus, when choosing the regularization parameter λ, we have to decide whether to retain many such black and white points along with preserving more details. In these experiments, we choose that the recovered images for the DZ-TGV model involve fewer black and white points and are slightly over-smoothed when M is smaller than 10. Comparing the SO-TGV model with our proposed model, we can observe that the SO-TGV model retains noise in the homogeneous region, which was not removed sufficiently. In contrast, as one can see in Figure 3.20, the denoising result of the SO-TGV model is less clear near the stem of the peppers than that of our model and a lot of remaining noise as a whole in the result of the SO-TGV model. In addition, our model in Figure 3.21 shows more details of the boat and the edges are more clearly restored.

Figures 3.22 present the denoised images for all models when the observed images are contaminated by the heavy multiplicative noise with noise level $M = 3$. The exp-SARP model removes noise in the homogeneous region while preserving details well owing to the SARP approach. However, comparing our model with the exp-SARP model, our model preserves edges more clearly in the face pattern than the exp-SARP model. Since the exp-SARP model and our model are based on the SARP approach, this result comes from the superiority of the NTGV regularization of our model. We can confirm the DZ-TGV model is not suitable for heavy noise and the TwL-

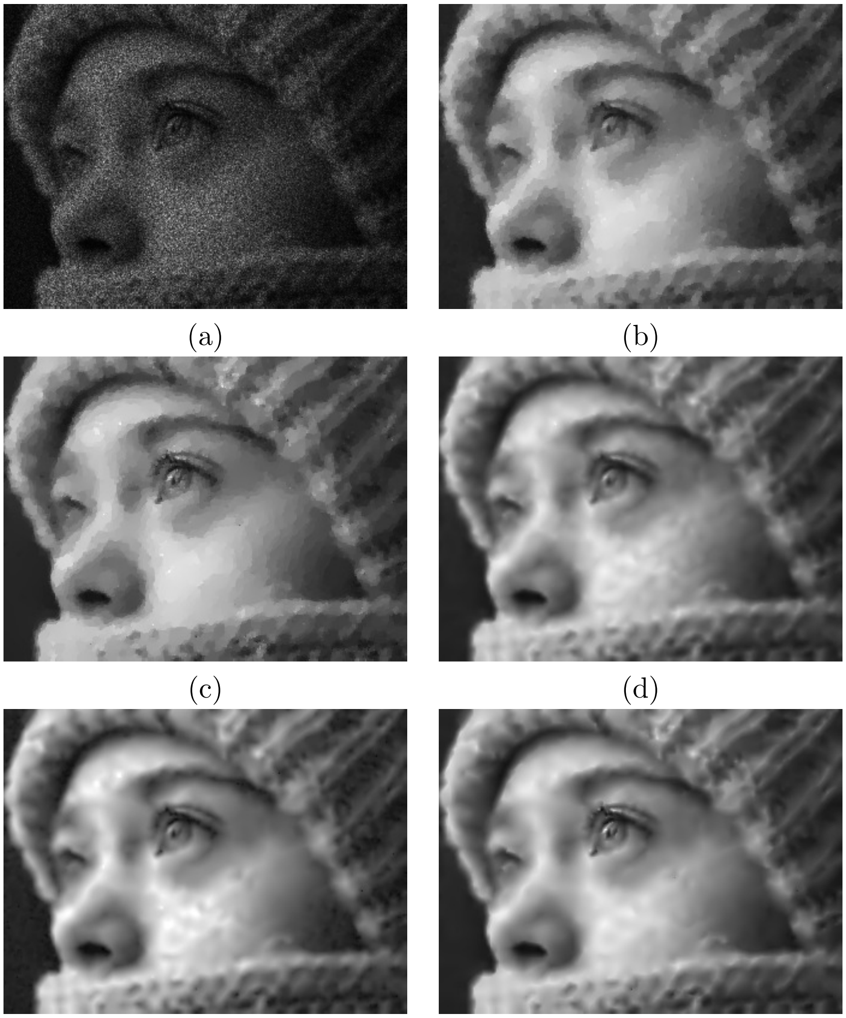

(a) (b) (c) (d) (e) (f)

Figure 3.18: Denoising results of our model when $M = 10$, and comparisons with other models: (a) data f with $M = 10$. Denoised images: (b) TwL-4V [35]; (c) exp-SARP [51]; (d) SO-TGV [25]; (e) DZ-TGV [64]; (f) our model.

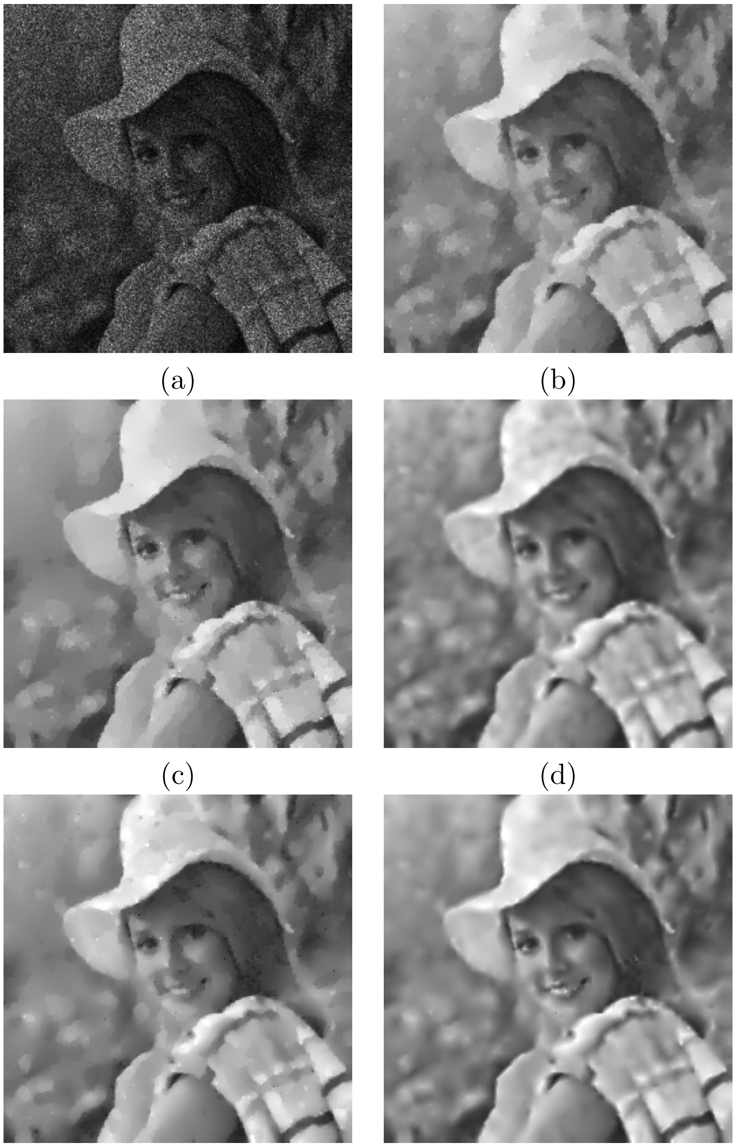

(a) (b)

(c) (d)

(e) (f)

Figure 3.19: Denoising results of our model when $M = 10$, and comparisons with other models: (a) data f with $M = 10$. Denoised images: (b) TwL-4V [35]; (c) exp-SARP [51]; (d) SO-TGV [25]; (e) DZ-TGV [64]; (f) our model.

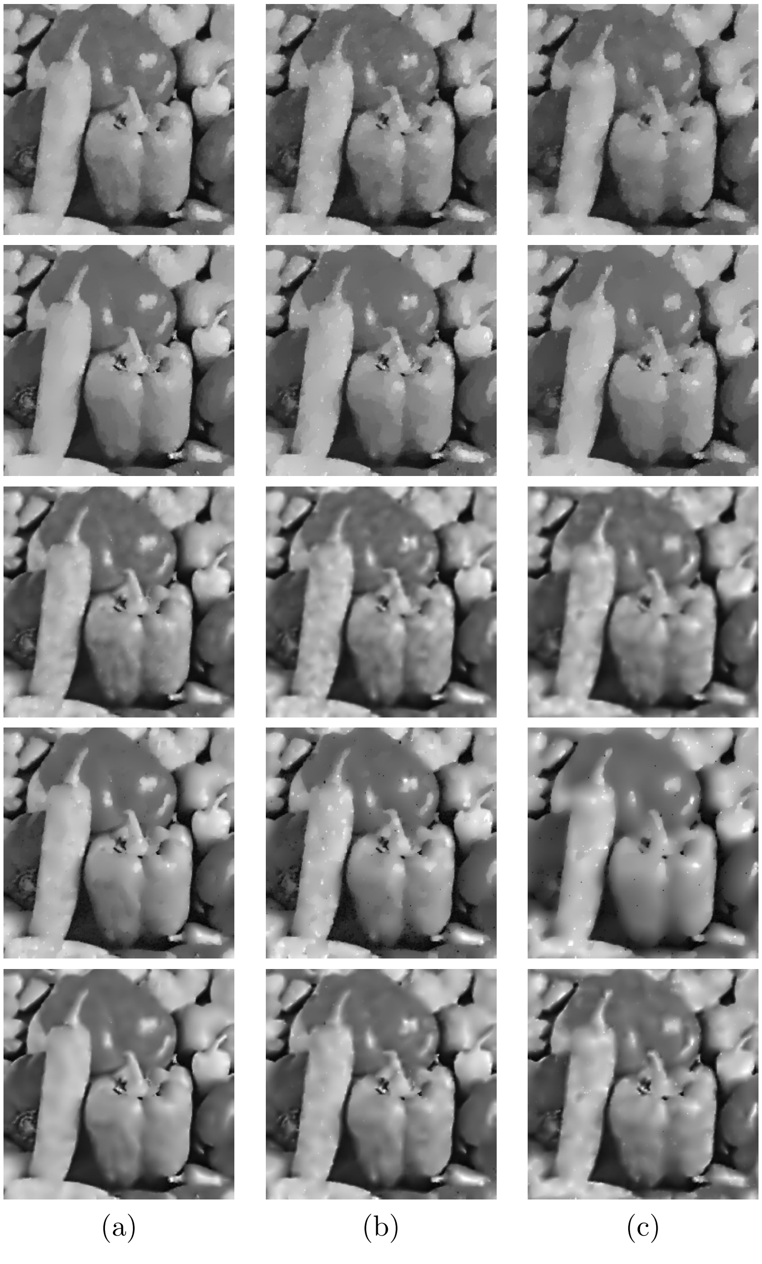
(a) (b) (c)

Figure 3.20: Denoised results of our model when (a) $M = 10$, (b) $M = 5$, and (c) $M = 3$, and comparisons with other models. Top to bottom rows: TwL-4V [35], exp-SARP [51], SO-TGV [25], DZ-TGV [64], and our model.

Figure 3.21: Denoised results of our model when (a) $M = 10$, (b) $M = 5$, and (c) $M = 3$, and comparisons with other models. Top to bottom rows: TwL-4V [35], exp-SARP [51], SO-TGV [25], DZ-TGV [64], and our model.

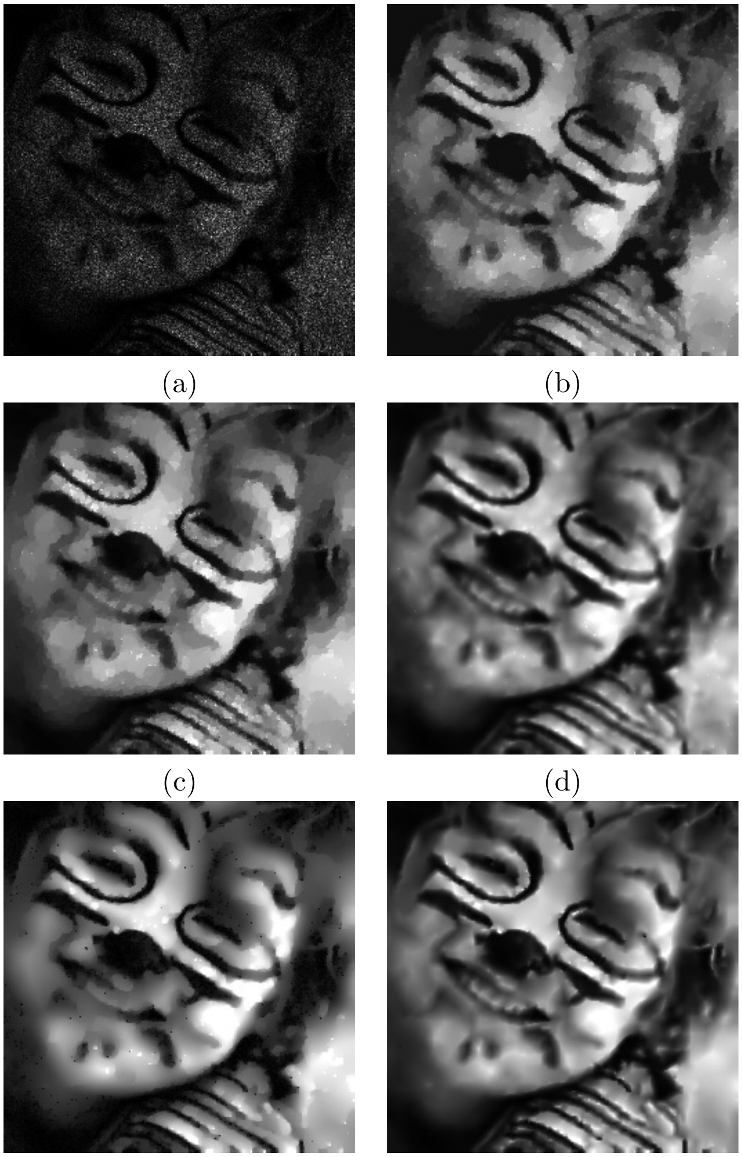

(a) (b)

(c) (d)

(e) (f)

Figure 3.22: Denoising results of our model when $M = 3$, and comparisons with other models: (a) data f with $M = 3$. Denoised images: (b) TwL-4V [35]; (c) exp-SARP [51]; (d) SO-TGV [25]; (e) DZ-TGV [64]; (f) our model.

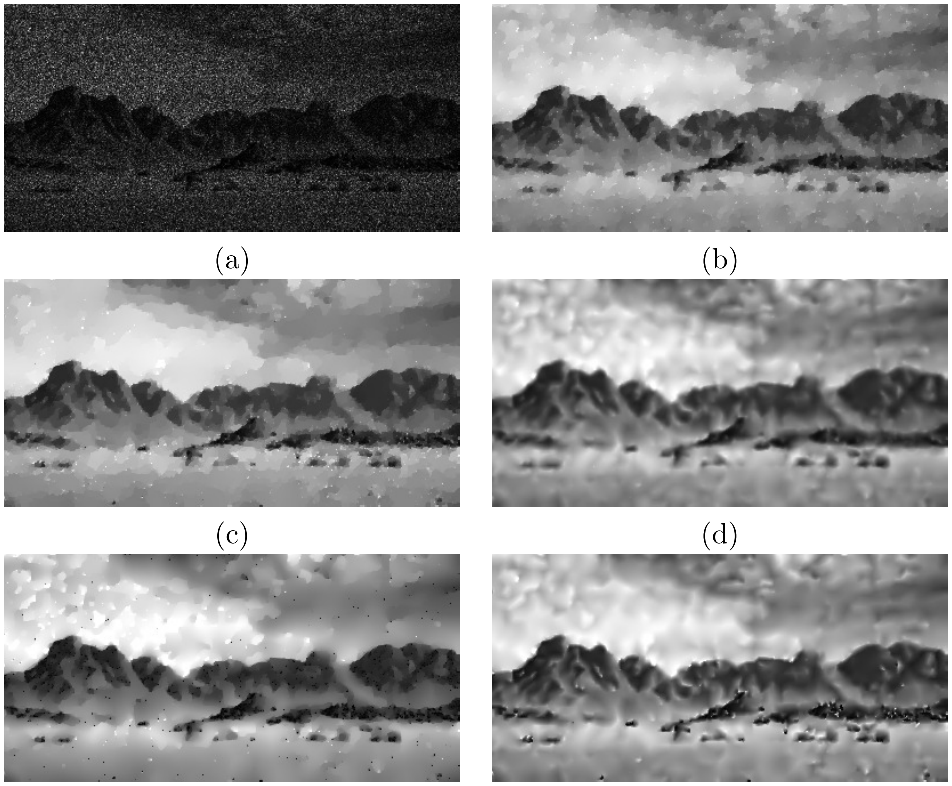

(a) (b)

(c) (d)

(e) (f)

Figure 3.23: Denoising results of our model when $M = 3$, and comparisons with other models: (a) data f with $M = 3$. Denoised images: (b) TwL-4V [35]; (c) exp-SARP [51]; (d) SO-TGV [25]; (e) DZ-TGV [64]; (f) our model.

4V model produces staircasing artifacts. The restored image of the SO-TGV model is satisfactory result, but that of our model shows less noise in the homogeneous region.

Figure 3.23 shows the degraded image with noise level $M = 3$ and denoising results of our model with comparisons with the exp-SARP model, the TwL-4V model, the SO-TGV model, and the DZ-TGV model. The DZ-TGV model produces unsatisfactory results for heavy noise levels. Our model removes noise in the sky region very well and furnishes more clear ridges compared with the SO-TGV. In addition, the proposed model better preserves the forest region, in front of the mountain, than the SO-TGV model. The restored images of the exp-SARP model and the TwL-4V model include

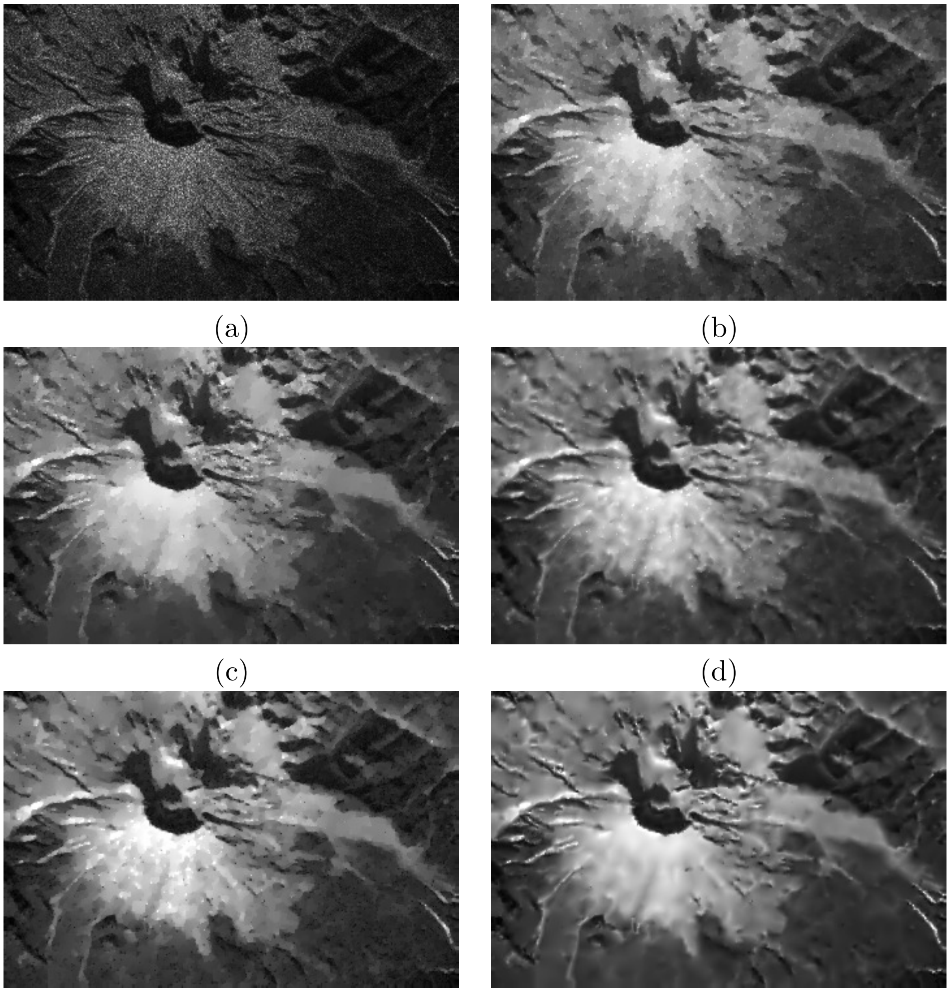

(a) (b) (c) (d) (e) (f)

Figure 3.24: Denoising results of our model when $M = 10$, and comparisons with other models: (a) data f with $M = 10$. Denoised images: (b) TwL-4V [35]; (c) exp-SARP [51]; (d) SO-TGV [25]; (e) DZ-TGV [64]; (f) our model.

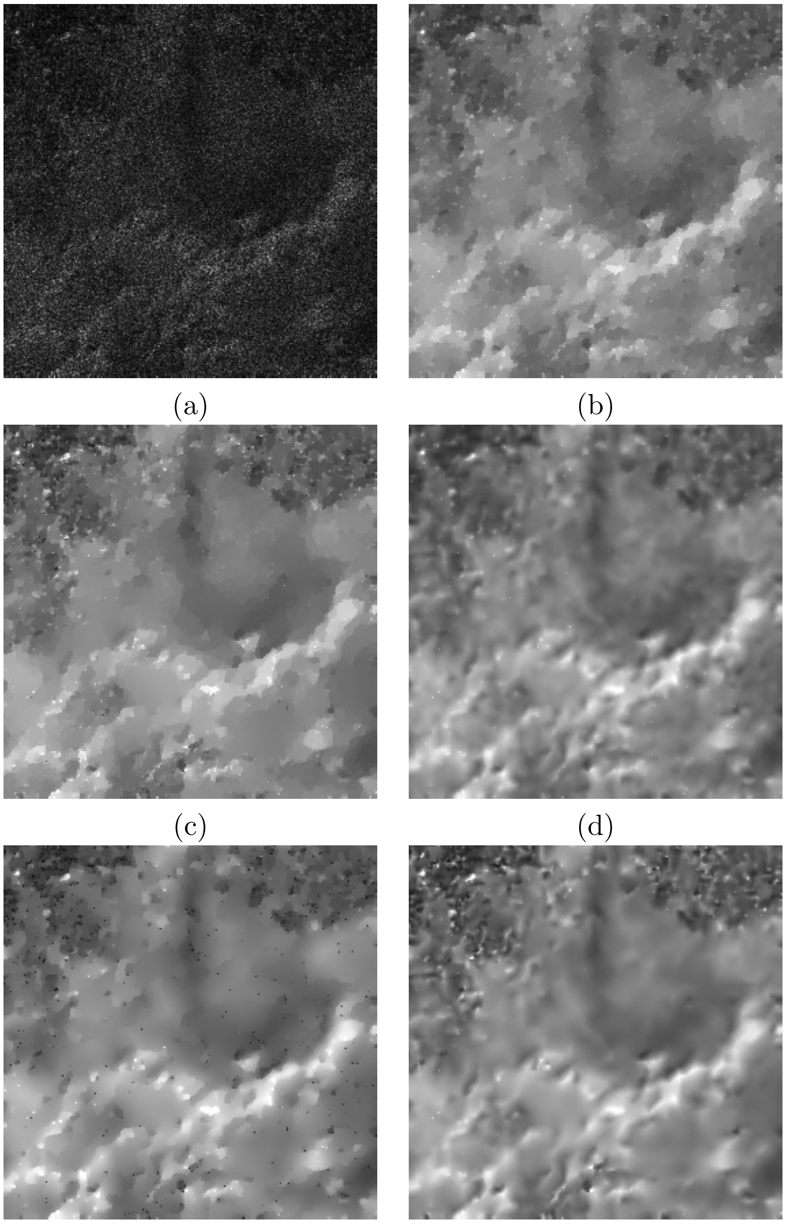

(a) (b) (c) (d) (e) (f)

Figure 3.25: Denoising results of our model when $M = 5$, and comparisons with other models: (a) data f with $M = 5$. Denoised images: (b) TwL-4V [35]; (c) exp-SARP [51]; (d) SO-TGV [25]; (e) DZ-TGV [64]; (f) our model.

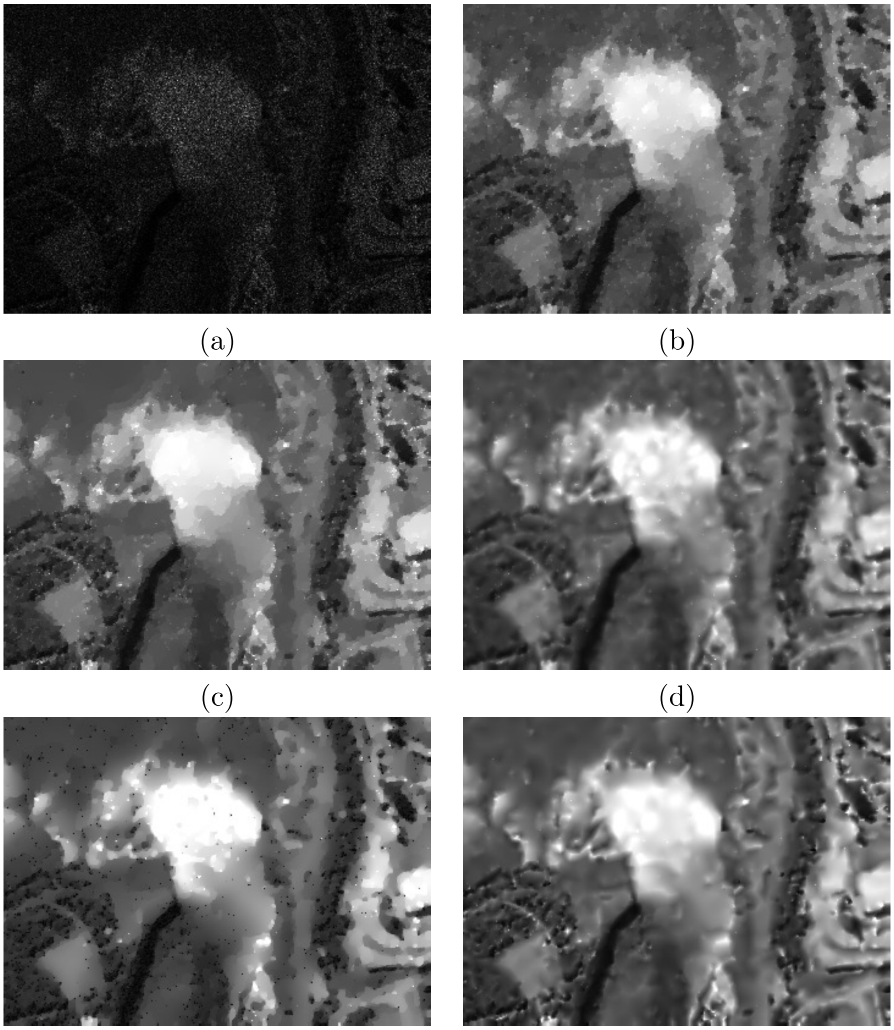

(a) (b) (c) (d) (e) (f)

Figure 3.26: Denoising results of our model when $M = 3$, and comparisons with other models: (a) data f with $M = 3$. Denoised images: (b) TwL-4V [35]; (c) exp-SARP [51]; (d) SO-TGV [25]; (e) DZ-TGV [64]; (f) our model.

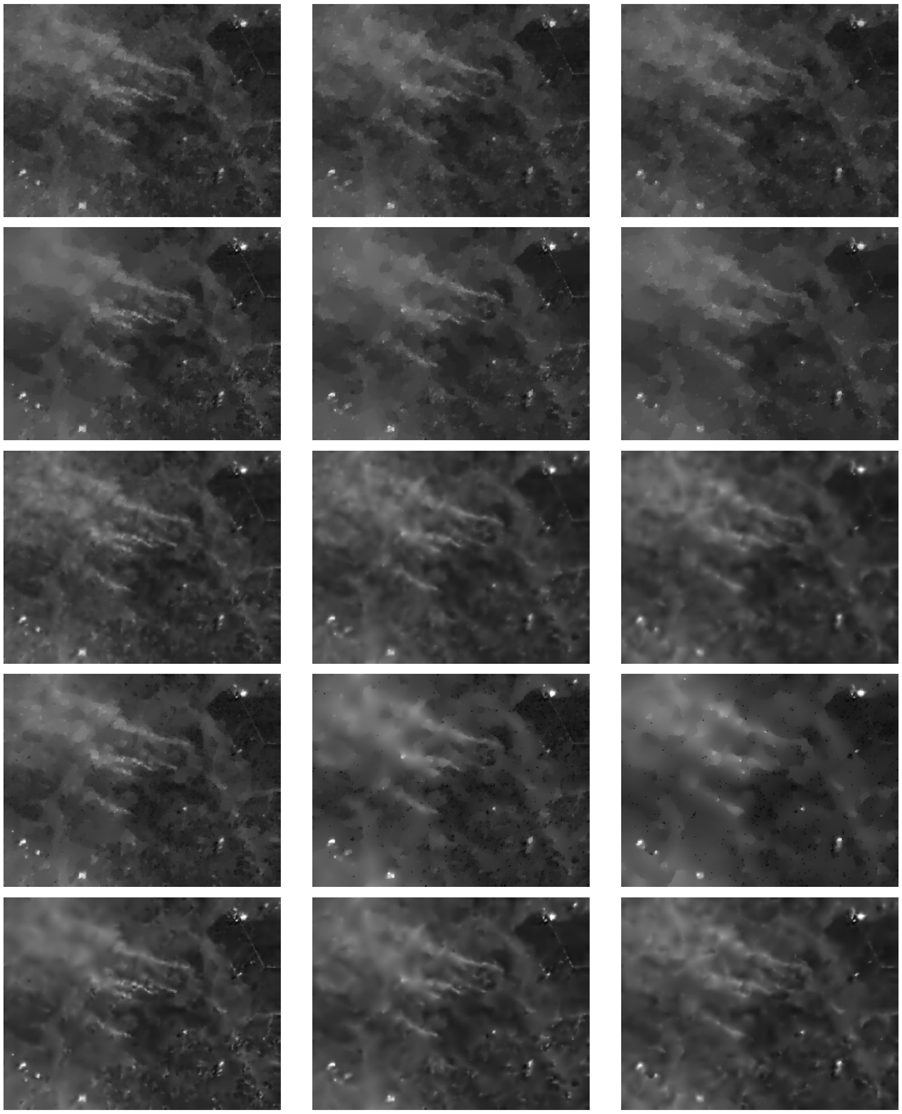

(a) (b) (c)

Figure 3.27: Denoised results of our model when (a) $M = 10$, (b) $M = 5$, and (c) $M = 3$ and comparisons with other models. Top to bottom rows: TwL-4V [35], exp-SARP [51], SO-TGV [25], DZ-TGV [64], our model.

several partitions in the sky region which cannot be observed in our model.

In Figures 3.24–3.27, we test all five models with SAR images with all noise levels $M = 10, 5$, and 3. It is observed that the exp-SARP model gives more successful results in terms of preserving fine features than the TwL-4V model, but both models still generate undesirable staircasing effects. The restored images of the DZ-TGV model improve as M increases. We can confirm that our model provides the best denoising results. For SAR images, our model also provides denoised images with well-smoothed homogeneous regions and conserved edges. Overall, the proposed model produces the restored images with the most natural visual quality and these numerical examples show the effectiveness of the NTGV regularization and the SARP approach.

In Tables 3.5, 3.6, and 3.7, we measure qualities of the restored images for the exp-SARP model, the TwL-4V model, the SO-TGV model, the DZ-TGV model, and our model. We report the PSNR and the SSIM values for $M = 10, 5$, and 3, respectively. We note that our proposed model has the highest PSNR and SSIM values for all images and for all noise levels. Although some PSNR values of the proposed model and exp-SARP model are not very different, we can see in Figures 3.21 and 3.23 that the denoising results of our model have better visual quality than those of the exp-SARP model.

	TwL-4V model	exp-SARP model	SO-TGV model	DZ-TGV model	Our model
Boat	25.30 / 0.6851	25.54 / 0.6985	24.93 / 0.6762	25.22 / 0.6853	**25.65 / 0.7094**
Elaine	27.05 / 0.7646	27.06 / 0.7688	27.54 / 0.7977	27.21 / 0.7792	**27.91 / 0.8103**
Face	26.70 / 0.8158	27.08 / 0.8508	27.99 / 0.8779	26.84 / 0.8455	**28.22 / 0.885**
Girl	28.99 / 0.8199	28.79 / 0.8218	30.39 / 0.8724	29.06 / 0.8655	**30.56 / 0.8789**
Mountain	24.73 / 0.6491	24.70 / 0.6539	24.42 / 0.6486	24.16 / 0.6348	**24.80 / 0.6677**
Peppers	27.10 / 0.8064	27.22 / 0.8161	27.10 / 0.8143	27.12 / 0.8124	**27.51 / 0.8303**
Remote1	24.97 / 0.7091	25.07 / 0.7072	24.96 / 0.7095	24.23 / 0.6885	**25.20 / 0.7098**
Remote2	24.70 / 0.6912	24.74 / 0.701	24.66 / 0.6775	23.89 / 0.665	**24.82 / 0.7025**
Remote3	30.33 / 0.769	30.36 / 0.7701	30.60 / 0.7816	30.01 / 0.7583	**30.82 / 0.7845**
Remote4	24.62 / 0.6287	24.64 / 0.6611	24.72 / 0.6442	24.33 / 0.6311	**24.88 / 0.6756**
average	26.45 / 0.7338	26.52 / 0.7449	26.73 / 0.75	26.21 / 0.7365	**27.04 / 0.7654**

Table 3.5: Comparisons of denoising results when $M = 10$ (PSNR/SSIM).

	TwL-4V model	exp-SARP model	SO-TGV model	DZ-TGV model	Our model
Boat	23.84 / 0.6207	23.89 / 0.6309	23.62 / 0.6165	23.41 / 0.6081	**24.17 / 0.6514**
Elaine	25.54 / 0.7122	25.41 / 0.714	26.01 / 0.7552	25.17 / 0.7173	**26.20 / 0.7622**
Face	25.02 / 0.7707	25.53 / 0.8065	26.12 / 0.8405	24.51 / 0.7974	**26.50 / 0.8493**
Girl	27.63 / 0.7806	27.29 / 0.7728	28.87 / 0.8394	26.90 / 0.8131	**29.00 / 0.8446**
Mountain	23.52 / 0.5869	23.40 / 0.5843	23.16 / 0.5791	22.66 / 0.5544	**23.51 / 0.6028**
Peppers	25.68 / 0.7601	25.82 / 0.7763	25.60 / 0.7732	25.17 / 0.7621	**26.16 / 0.7959**
Remote1	23.53 / 0.6329	23.60 / 0.622	23.54 / 0.6422	22.55 / 0.6005	**23.70 / 0.6461**
Remote2	23.38 / 0.6119	23.39 / 0.6171	23.34 / 0.5835	22.22 / 0.5755	**23.57 / 0.6249**
Remote3	29.32 / 0.7288	29.36 / 0.7286	29.45 / 0.7351	28.20 / 0.6977	**29.76 / 0.7434**
Remote4	23.53 / 0.5588	23.42 / 0.5787	23.63 / 0.575	22.91 / 0.55	**23.74 / 0.6075**
average	25.10 / 0.6763	25.11 / 0.6831	25.33 / 0.6939	24.37 / 0.6676	**25.63 / 0.7128**

Table 3.6: Comparisons of denoising results when $M = 5$ (PSNR/SSIM).

	TwL-4V model	exp-SARP model	SO-TGV model	DZ-TGV model	Our model
Boat	22.93 / 0.5786	23.01 / 0.5837	22.71 / 0.5704	21.92 / 0.5355	**23.11 / 0.6005**
Elaine	24.27 / 0.6706	23.95 / 0.6689	24.50 / 0.7117	23.06 / 0.6436	**24.80 / 0.724**
Face	23.50 / 0.7347	24.12 / 0.7624	24.66 / 0.8058	22.45 / 0.7389	**25.00 / 0.8181**
Girl	26.32 / 0.7465	26.25 / 0.7332	27.32 / 0.8038	25.30 / 0.7447	**27.50 / 0.8125**
Mountain	22.58 / 0.542	22.57 / 0.5384	22.30 / 0.533	21.12 / 0.4885	**22.63 / 0.56**
Peppers	24.16 / 0.7327	24.42 / 0.7371	24.27 / 0.7368	23.21 / 0.7074	**24.77 / 0.7534**
Remote1	22.61 / 0.576	22.65 / 0.5723	22.64 / 0.5731	20.77 / 0.5142	**22.75 / 0.5755**
Remote2	22.43 / 0.5525	22.45 / 0.5526	22.46 / 0.5327	20.32 / 0.4972	**22.60 / 0.565**
Remote3	28.37 / 0.6908	28.41 / 0.6931	28.56 / 0.7043	27.08 / 0.6514	**28.75 / 0.7138**
Remote4	22.81 / 0.5116	22.71 / 0.521	22.92 / 0.5309	21.95 / 0.4849	**23.02 / 0.5513**
average	24.00 / 0.6336	24.05 / 0.6362	24.23 / 0.6502	22.72 / 0.6006	**24.49 / 0.6674**

Table 3.7: Comparisons of denoising results when $M = 3$ (PSNR/SSIM).

Chapter 4

Conclusion

In this dissertation, we proposed a new variational models, incorporated with the SARP approach, for restoring images corrupted by multiplicative Gamma noise. The new models, in particular, are based on the exp model [48]; thus, it is designed to effectively deal with heavy multiplicative noise. The SARP approach enhanced the denoising results, by sufficiently reducing the noise in homogeneous regions while preserving textures. Moreover, our SARP approach further improved denoising results as it used multiple local windows unlike prior work [17], which used only one local window.

For the exp TV model with SARP (Proposed model 1), the convergence analysis such as the existence and uniqueness of a solution for the model was also demonstrated. Further, a SARP algorithm corresponding to our proposed model was derived from the first order optimality conditions. Furthermore, we adopted a proximal linearized alternating direction algorithm to solve our subproblem. This resulted in a fast and efficient iterative algorithm for solving our model. We tested our proposed model and algorithm on various natural images and SAR images. Numerical experiments demonstrated the effectiveness and efficiency of our proposed model and algorithm, in terms of visual quality and various quantities, compared to several state-of-the-art models.

For exp NTGV model with SARP (Proposed model 2), we used a NTGV regularization and a SARP were utilized. The NTGV allowed us to adequately denoise smooth regions without the staircasing artifacts that appear in TV-based models, while preserving edges and details. The SARP further assisted in keeping textures and small scales during the denoising process. We presented an automatic selection rule for the SARP, by introducing a constrained model with local constraints associated with multiple local windows. To solve the nonconvex minimization problem, we employed the IRLA, and the ADMM was adopted to solve the subproblem induced by the IRLA. These led to an efficient iterative algorithm for solving the proposed model. We tested our proposed model and algorithm on several images including real natural and SAR images. Numerical results showed the superiority of our proposed model over the state-of-the-art models with regards to visual quality and some quantities.

Bibliography

[1] Andrés Almansa, Coloma Ballester, Vicent Caselles, and Gloria Haro. A TV based restoration model with local constraints. *Journal of Scientific Computing*, 34(3):209–236, 2008.

[2] Marco Artina, Massimo Fornasier, and Francesco Solombrino. Linearly constrained nonsmooth and nonconvex minimization. *SIAM Journal on Optimization*, 23(3):1904–1937, 2013.

[3] H Attouch, G Buttazzo, and G Michaille. Variational analysis in sobolev and bv spaces: Applications to pdes and optimization, mps/siam ser, 2005.

[4] Hedy Attouch, Jérôme Bolte, and Benar Fux Svaiter. Convergence of descent methods for semi-algebraic and tame problems: proximal algorithms, forward-backward splitting, and regularized Gauss-Seidel methods. *Mathematical Programming*, 137(1-2):91–129, 2013.

[5] Gilles Aubert and Jean-Francois Aujol. A variational approach to removing multiplicative noise. *SIAM Journal on Applied Mathematics*, 68(4):925–946, 2008.

[6] Gilles Aubert and Pierre Kornprobst. *Mathematical problems in image processing: partial differential equations and the calculus of variations*, volume 147. Springer Science & Business Media, 2006.

[7] Marcelo Bertalmío, Vicent Caselles, Bernard Rougé, and A Solé. TV based image restoration with local constraints. *Journal of scientific computing*, 19(1):95–122, 2003.

[8] Stephen Boyd. Alternating direction method of multipliers. In *Talk at NIPS Workshop on Optimization and Machine Learning*, 2011.

[9] Kristian Bredies, Karl Kunisch, and Thomas Pock. Total generalized variation. *SIAM Journal on Imaging Sciences*, 3(3):492–526, 2010.

[10] Emmanuel J Candes, Michael B Wakin, and Stephen P Boyd. Enhancing sparsity by reweighted ℓ_1 minimization. *Journal of Fourier analysis and applications*, 14(5-6):877–905, 2008.

[11] Turgay Celik and Kai-Kuang Ma. Unsupervised change detection for satellite images using dual-tree complex wavelet transform. *IEEE Transactions on Geoscience and Remote Sensing*, 48(3):1199–1210, 2010.

[12] Turgay Celik and Kai-Kuang Ma. Multitemporal image change detection using undecimated discrete wavelet transform and active contours. *IEEE Transactions on Geoscience and Remote Sensing*, 49(2):706–716, 2011.

[13] Antonin Chambolle and Pierre-Louis Lions. Image recovery via total variation minimization and related problems. *Numerische Mathematik*, 76(2):167–188, 1997.

[14] Antonin Chambolle and Thomas Pock. A first-order primal-dual algorithm for convex problems with applications to imaging. *Journal of Mathematical Imaging and Vision*, 40(1):120–145, 2011.

[15] Tony Chan, Antonio Marquina, and Pep Mulet. High-order total variation-based image restoration. *SIAM Journal on Scientific Computing*, 22(2):503–516, 2000.

[16] Dai-Qiang Chen and Li-Zhi Cheng. Spatially adapted regularization parameter selection based on the local discrepancy function for Poissonian image deblurring. *Inverse Problems*, 28(1):015004, 2011.

[17] Dai-Qiang Chen and Li-Zhi Cheng. Spatially adapted total variation model to remove multiplicative noise. *IEEE Transactions on Image Processing*, 21(4):1650–1662, 2012.

[18] Dai-Qiang Chen and Li-Zhi Cheng. Fast linearized alternating direction minimization algorithm with adaptive parameter selection for multiplicative noise removal. *Journal of Computational and Applied Mathematics*, 257:29–45, 2014.

[19] John B Conway. *A course in functional analysis*, volume 96. Springer Science & Business Media, 2013.

[20] Kostadin Dabov, Alessandro Foi, Vladimir Katkovnik, and Karen Egiazarian. Image denoising by sparse 3-D transform-domain collaborative filtering. *IEEE Transactions on image processing*, 16(8):2080–2095, 2007.

[21] Fangfang Dong, Haili Zhang, and De-Xing Kong. Nonlocal total variation models for multiplicative noise removal using split Bregman iteration. *Mathematical and Computer Modelling*, 55(3):939–954, 2012.

[22] Yiqiu Dong, Michael Hintermüller, and M Monserrat Rincon-Camacho. Automated regularization parameter selection in multi-scale total variation models for image restoration. *Journal of Mathematical Imaging and Vision*, 40(1):82–104, 2011.

[23] Yiqiu Dong and Tieyong Zeng. A convex variational model for restoring blurred images with multiplicative noise. *SIAM Journal on Imaging Sciences*, 6(3):1598–1625, 2013.

[24] Michael Elad and Michal Aharon. Image denoising via sparse and redundant representations over learned dictionaries. *IEEE Transactions on Image processing*, 15(12):3736–3745, 2006.

[25] Wensen Feng, Hong Lei, and Yang Gao. Speckle reduction via higher order total variation approach. *IEEE Transactions on Image Processing*, 23(4):1831–1843, 2014.

[26] Victor S Frost, Josephine Abbott Stiles, K Sam Shanmugan, and Julian C Holtzman. A model for radar images and its application to adaptive digital filtering of multiplicative noise. *IEEE Transactions on pattern analysis and machine intelligence*, (2):157–166, 1982.

[27] Pascal Getreuer. Total variation deconvolution using split Bregman. *Image Processing On Line*, 2:158–174, 2012.

[28] Pascal Getreuer, Melissa Tong, and Luminita A Vese. A variational model for the restoration of MR images corrupted by blur and Rician noise. In *International Symposium on Visual Computing*, pages 686–698. Springer, 2011.

[29] Guy Gilboa, Nir Sochen, and Yehoshua Y Zeevi. Variational denoising of partly textured images by spatially varying constraints. *IEEE Transactions on Image Processing*, 15(8):2281–2289, 2006.

[30] Tom Goldstein and Stanley Osher. The split Bregman method for L1-regularized problems. *SIAM journal on imaging sciences*, 2(2):323–343, 2009.

[31] Markus Grasmair. Locally adaptive total variation regularization. In *International Conference on Scale Space and Variational Methods in Computer Vision*, pages 331–342. Springer, 2009.

[32] Weihong Guo, Jing Qin, and Wotao Yin. A new detail-preserving regularization scheme. *SIAM Journal on Imaging Sciences*, 7(2):1309–1334, 2014.

[33] Yu-Mei Huang, Lionel Moisan, Michael K Ng, and Tieyong Zeng. Multiplicative noise removal via a learned dictionary. *IEEE Transactions on Image Processing*, 21(11):4534–4543, 2012.

[34] Myeongmin Kang, Myungjoo Kang, and Miyoun Jung. Nonconvex higher-order regularization based Rician noise removal with spatially adaptive parameters. *Journal of Visual Communication and Image Representation*, 32:180–193, 2015.

[35] Myungjoo Kang, Sangwoon Yun, and Hyenkyun Woo. Two-level convex relaxed variational model for multiplicative denoising. *SIAM Journal on Imaging Sciences*, 6(2):875–903, 2013.

[36] Pierre Kornprobst, Rachid Deriche, and Gilles Aubert. Image sequence analysis via partial differential equations. *Journal of Mathematical Imaging and Vision*, 11(1):5–26, 1999.

[37] Dilip Krishnan and Rob Fergus. Fast image deconvolution using hyper-Laplacian priors. In *Advances in Neural Information Processing Systems*, pages 1033–1041, 2009.

[38] Karl Krissian, Carl-Fredrik Westin, Ron Kikinis, and Kirby G Vosburgh. Oriented speckle reducing anisotropic diffusion. *IEEE Transactions on Image Processing*, 16(5):1412–1424, 2007.

[39] Darwin T Kuan, Alexander A Sawchuk, Timothy C Strand, and Pierre Chavel. Adaptive noise smoothing filter for images with signal-dependent noise. *IEEE transactions on pattern analysis and machine intelligence*, (2):165–177, 1985.

[40] Alessandro Lanza, Serena Morigi, and Fiorella Sgallari. Convex image denoising via non-convex regularization. In *International Conference on Scale Space and Variational Methods in Computer Vision*, pages 666–677. Springer, 2015.

[41] Triet Le, Rick Chartrand, and Thomas J Asaki. A variational approach to reconstructing images corrupted by Poisson noise. *Journal of mathematical imaging and vision*, 27(3):257–263, 2007.

[42] Jong-Sen Lee. Digital image enhancement and noise filtering by use of local statistics. *IEEE transactions on pattern analysis and machine intelligence*, (2):165–168, 1980.

[43] Jong-Sen Lee, Karl W Hoppel, Stephen A Mango, and Allen R Miller. Intensity and phase statistics of multilook polarimetric and interferometric SAR imagery. *IEEE Transactions on Geoscience and Remote Sensing*, 32(5):1017–1028, 1994.

[44] Fang Li, Michael K Ng, and Chaomin Shen. Multiplicative noise removal with spatially varying regularization parameters. *SIAM Journal on Imaging Sciences*, 3(1):1–20, 2010.

[45] Fang Li, Chaomin Shen, Jingsong Fan, and Chunli Shen. Image restoration combining a total variational filter and a fourth-order filter. *Journal of Visual Communication and Image Representation*, 18(4):322–330, 2007.

[46] Zhi Li, Yifei Lou, and Tieyong Zeng. Variational multiplicative noise removal by DC programming. *Journal of Scientific Computing*, 68(3):1200–1216, 2016.

[47] Gang Liu, Ting-Zhu Huang, and Jun Liu. High-order TVL1-based images restoration and spatially adapted regularization parameter selection. *Computers & Mathematics with Applications*, 67(10):2015–2026, 2014.

[48] Jian Lu, Lixin Shen, Chen Xu, and Yuesheng Xu. Multiplicative noise removal in imaging: An exp-model and its fixed-point proximity algorithm. *Applied and Computational Harmonic Analysis*, 41(2):518–539, 2016.

[49] Vese Luminita and Tony F Chan. Reduced non-convex functional approximations for imag restoration & segmentation. *UCLA CAM Website 97-56 (1997).*

[50] Marius Lysaker, Arvid Lundervold, and Xue-Cheng Tai. Noise removal using fourth-order partial differential equation with applications to medical magnetic resonance images in space and time. *IEEE Transactions on image processing*, 12(12):1579–1590, 2003.

[51] Hanwool Na, Myeongmin Kang, Miyoun Jung, and Myungjoo Kang. An exp model with spatially adaptive regularization parameters for multiplicative noise removal. *http://ncia.snu.ac.kr/xe/preprint*.

[52] Mila Nikolova, Michael K Ng, and Chi-Pan Tam. Fast nonconvex nonsmooth minimization methods for image restoration and reconstruction. *IEEE Transactions on Image Processing*, 19(12):3073–3088, 2010.

[53] Peter Ochs, Alexey Dosovitskiy, Thomas Brox, and Thomas Pock. An iterated ℓ_1 algorithm for non-smooth non-convex optimization in computer vision. In *Proceedings of the IEEE Conference on Computer Vision and Pattern Recognition*, pages 1759–1766, 2013.

[54] Peter Ochs, Alexey Dosovitskiy, Thomas Brox, and Thomas Pock. On iteratively reweighted algorithms for nonsmooth nonconvex optimization in computer vision. *SIAM Journal on Imaging Sciences*, 8(1):331–372, 2015.

[55] Seungmi Oh, Hyenkyun Woo, Sangwoon Yun, and Myungjoo Kang. Non-convex hybrid total variation for image denoising. *Journal of Visual Communication and Image Representation*, 24(3):332–344, 2013.

[56] Stanley Osher, Yu Mao, Bin Dong, and Wotao Yin. Fast linearized Bregman iteration for compressive sensing and sparse denoising. *arXiv preprint arXiv:1104.0262*, 2011.

[57] Yuyuan Ouyang, Yunmei Chen, Guanghui Lan, and Eduardo Pasiliao Jr. An accelerated linearized alternating direction method of multipliers. *SIAM Journal on Imaging Sciences*, 8(1):644–681, 2015.

[58] Ankit Parekh and Ivan W Selesnick. Convex denoising using nonconvex tight frame regularization. *IEEE Signal Processing Letters*, 22(10):1786–1790, 2015.

[59] Sara Parrilli, Mariana Poderico, Cesario Vincenzo Angelino, and Luisa Verdoliva. A nonlocal SAR image denoising algorithm based on LLMMSE wavelet shrinkage. *IEEE Transactions on Geoscience and Remote Sensing*, 50(2):606–616, 2012.

[60] Pietro Perona and Jitendra Malik. Scale-space and edge detection using anisotropic diffusion. *IEEE Transactions on pattern analysis and machine intelligence*, 12(7):629–639, 1990.

[61] Leonid Rudin, Pierre-Luis Lions, and Stanley Osher. Multiplicative denoising and deblurring: theory and algorithms. In *Geometric Level Set Methods in Imaging, Vision, and Graphics*, pages 103–119. Springer, 2003.

[62] Leonid I Rudin, Stanley Osher, and Emad Fatemi. Nonlinear total variation based noise removal algorithms. *Physica D: Nonlinear Phenomena*, 60(1-4):259–268, 1992.

[63] Simon Setzer. Operator splittings, Bregman methods and frame shrinkage in image processing. *International Journal of Computer Vision*, 92(3):265–280, 2011.

[64] Mu-Ga Shama, Ting-Zhu Huang, Jun Liu, and Si Wang. A convex total generalized variation regularized model for multiplicative noise and blur removal. *Applied Mathematics and Computation*, 276:109–121, 2016.

[65] Jianing Shi and Stanley Osher. A nonlinear inverse scale space method for a convex multiplicative noise model. *SIAM Journal on Imaging Sciences*, 1(3):294–321, 2008.

[66] Suvrit Sra. Scalable nonconvex inexact proximal splitting. In *Advances in Neural Information Processing Systems*, pages 530–538, 2012.

[67] Gabriele Steidl and Tanja Teuber. Removing multiplicative noise by Douglas-Rachford splitting methods. *Journal of Mathematical Imaging and Vision*, 36(2):168–184, 2010.

[68] Zhou Wang, Alan C Bovik, Hamid R Sheikh, and Eero P Simoncelli. Image quality assessment: from error visibility to structural similarity. *IEEE transactions on image processing*, 13(4):600–612, 2004.

[69] Hyenkyun Woo and Sangwoon Yun. Proximal linearized alternating direction method for multiplicative denoising. *SIAM Journal on Scientific Computing*, 35(2):B336–B358, 2013.

[70] Junfeng Yang and Yin Zhang. Alternating direction algorithms for ℓ_1-problems in compressive sensing. *SIAM journal on scientific computing*, 33(1):250–278, 2011.

[71] Junfeng Yang, Yin Zhang, and Wotao Yin. A fast alternating direction method for TVL1-L2 signal reconstruction from partial Fourier data. *IEEE Journal of Selected Topics in Signal Processing*, 4(2):288–297, 2010.

[72] Yongjian Yu and Scott T Acton. Speckle reducing anisotropic diffusion. *IEEE Transactions on image processing*, 11(11):1260–1270, 2002.

국문초록

본 논문에서는 편미분 방정식을 이용한 곱셈 감마 잡음으로 오염된 영상복원의 변분법적인 모델에 대해서 다룬다. 두 가지 제안하는 모델은 실제 응용에서 많이 다루는 강한 곱셈 잡음에 적합하다. 첫 번째로 우리는 국지 제한 조건과 총 변이 정규화를 기반으로 한 모델을 제안한다. 국지 제한조건은 여러 개의 국지 창으로 구성되어 있는데 이는 국지적 조정 정규화 매개변수와 연관이 있다. 게다가 해의 존재성과 유일성과 같은 분석도 제공한다. 두 번째로는 우리는 첫 번째 모델을 비볼록일반총변이로 확장시켰다. 비볼록일반총변이는 평평한 지역을 효과적으로 잡음을 제거하고 경계와 세부적인 부분을 보존해주면서 총 변이 정규화에서 보이던 계단현상이 나타나지 않는다.

주요어휘: 영상잡음제거, 곱셈 감마 잡음, 국지적 조정 정규화 매개변수, 근접 선형화된 교류방향 알고리즘, 비볼록일반화총변이, 반복적 재가중치 ℓ_1 알고리즘
학번: 2011-20269